MASTERARBEIT | MASTER'S THESIS

Titel | Title

Mercury isotope fractionation during reduction of mercury(II) by dissolved or surface bound iron(II) species

verfasst von | submitted by

Niklas Gallati BSc

angestrebter akademischer Grad | in partial fulfilment of the requirements for the degree of

Master of Science (MSc)

Wien | Vienna, 2024

Studienkennzahl lt. Studienblatt | Degree programme code as it appears on the student record sheet:	UA 066 815
Studienrichtung lt. Studienblatt | Degree programme as it appears on the student record sheet:	Masterstudium Erdwissenschaften
Betreut von | Supervisor:	Univ.-Prof. Dipl.-Geol. Dr. Stephan Krämer

Acknowledgements

First and most importantly, I want to thank my supervisor Lorenz Schwab, who was a PhD student for most of the time I worked on this thesis. Not only has he helped me with every step of this thesis, from introducing me to the lab work and designing the first experiments to the last word I wrote in this work, he also encouraged me in tough times both academically and privately with outstanding patience. He was the best mentor I could have wished for and more. Without him, I would have never been able to finish this thesis.

I also want to thank my fellow MSc students Florian Exler and Katharina Reinhold for the inspiring discussions about our respective work and sharing both setbacks and happy moments during our first steps in the academic world.

I also want to thank Stephan Krämer, Naresh Kumar and Jan Wiederhold for their expertise and technical input. For providing the chemicals and the working space I needed to carry out the experiments, I want to thank the Krämer Group in the Department of Environmental Geosciences and the University Vienna in general.

I also want to thank my parents who made my academic journey possible and Alexander Budik and Birgit Krampl, who stood by my side during the writing part of this thesis.

Last but not least, I want to thank Patrick Pesek and Clemens Schmalfuß, whom I met in my first semester of my bachelor studies. They accompanied my academic way until now and became close friends along this journey.

Abstract

Mercury (Hg) is an important inorganic pollutant widely spread across the world. Growing awareness of its danger and advanced analytical methods have led to a better understanding of its behavior in the environment. Over the last two decades, MC-ICP-MS analysis has enhanced the relevance of Hg stable isotope fractionation research regarding various chemical processes for source tracking and predicting the fate of Hg in nature. This study aims to gain better understandings of Hg isotope behavior when Fe(II) reduces Hg(II) to Hg(0) either dissolved in water or sorbed to an unreactive Al_2O_3-surface under dark anoxic conditions (pH = 8). Both the homogeneous (Fe(II) dissolved) and the heterogeneous (Fe(II) sorbed to Al_2O_3-particles) reactions favored the lighter Hg isotopes but differed in their enrichment factors for mass dependent fractionation (MDF): Enrichment factors for the homogeneous experiments ranged from $\varepsilon^{202}Hg$ = -2.93 ‰ to -2.79 ‰ and between $\varepsilon^{202}Hg$ = -2.32 ‰ and -2.25 ‰ for the heterogeneous experiments. These two Hg reductions led to similar positive mass independent fractionation (MIF) of the odd mass isotope ^{199}Hg, showing enrichment factors of $E^{199}Hg$ = 0.29 ‰ and $E^{199}Hg$ = 0.30 ‰ in the experiments with Fe(II) in solution and $E^{199}Hg$ = 0.27 ‰ and $E^{199}Hg$ = 0.25 ‰ in the experiments with Fe(II) bound to Al_2O_3. The $\Delta^{199}Hg$- and $\Delta^{201}Hg$-data suggest nuclear volume effect to be the main mechanism driving MIF ($\Delta^{199}Hg$ / $\Delta^{201}Hg$ – slope: 1.70 ± 0.12 in the homogeneous and 1.56 ± 0.11 in the heterogeneous reduction). The sorption process of Hg to Al_2O_3 slightly favored lighter isotopes in experiments specifically designed to investigate the sorption process as well as in the heterogeneous reduction experiments. The homogeneous reduction kinetic, with a rate constant k = -2.04*10^4 M^{-1} min^{-1}, was observed to be faster than in previous studies. The results indicate a possible distinction between different Hg reduction processes through stable isotope analysis, as studies observing photochemical or microbial reduction led to different MDF- and / or MIF-factors than witnessed for the abiotic reduction with Fe(II) in this work.

Deutsche Zusammenfassung

Quecksilber (Hg) ist ein weit verbreiteter anorganischer Schadstoff. Über die letzten Jahre wurde das Bewusstsein über seine Gefahr für Mensch und Umwelt immer größer und moderne analytische Methoden haben zu einem besseren Verständnis über das Verhalten und die Verbreitung von Quecksilber geführt. Etwa seit Beginn des 21. Jahrhunderts hat die Entwicklung von MC-ICP-MS-Technologie die wissenschaftliche Relevanz der Schwermetallisotopenforschung in Bezug auf das Verständnis über verschiedene chemische Prozesse und Vorgänge in der Umwelt erhöht. In dieser Studie werden Erkenntnisse über die Quecksilberisotopenfraktionierung bei der Reduktion von Hg(II) zu Hg(0) sowohl durch gelöstes Fe(II), als auch durch an Al_2O_3-Partikel adsorbiertes Fe(II) unter dunklen, anoxischen Bedingungen erzielt (pH = 8). In beiden Fällen reagierten die leichteren Quecksilberisotope schneller als die schwereren, jedoch mit unterschiedlichen Fraktionierungsfaktoren: Die homogenen Experimente (Fe(II) in Lösung) ergaben $\varepsilon^{202}Hg$ = -2.93 ‰ und $\varepsilon^{202}Hg$ = -2.79 ‰ und die heterogenen (Fe(II) adsorbiert an Al_2O_3) $\varepsilon^{202}Hg$ = -2.32 ‰ und -2.25 ‰. Die beiden Hg-Reduktionsvorgänge führten zu ähnlichen massenunabhängigen Fraktionierung (MIF) mit Fraktionierungsfaktoren der ungeraden Isotope: $E^{199}Hg$ = 0.29 ‰ und $E^{199}Hg$ = 0.30 ‰, durch Fe(II) in gelöster Form und $E^{199}Hg$ = 0.27 ‰ und $E^{199}Hg$ = 0.25 ‰ bei den Experimenten mit an Al_2O_3 adsorbiertem Fe(II). Die $\Delta^{199}Hg$- und $\Delta^{201}Hg$-Daten zeigen, dass der Kernvolumeneffekt der Grund für die MIF ist ($\Delta^{199}Hg$ / $\Delta^{201}Hg$ – Steigung: 1.70 ± 0.12 bei der homogenen und 1.56 ± 0.11 bei der heterogenen Reduktion). Die Sorption von Quecksilber an die Al_2O_3-Oberfläche bevorzugte die leichten Hg isotope geringfügig, wie sowohl bei den heterogenen Experimenten als auch bei spezifisch für die Untersuchung des Sorptionsprozesses gestalteten Versuchen beobachtet werden konnte. Die Kinetik der homogenen Reduktion lief mit k = $-2.04*10^4$ M^{-1} min^{-1} etwas schneller ab als in vorgängigen Studien beschrieben. Die Resultate dieser Studie zeigen, dass eine Unterscheidung von verschiedenen Hg-Reduktionsprozessen durch Analyse der stabilen Isotope möglich sein kann, da Studien über zum Beispiel Photoreduktion und mikrobielle Quecksilberreduktion zu anderen MDF- und / oder MIF-Faktoren führten, als die abiotische Reduktion durch Fe(II), die in dieser Studie untersucht wurde.

Table of contents

Table of figures

Table of tables

1. Introduction

Mercury (Hg) is a significant inorganic pollutant and can have a great negative impact on human health and wildlife when exceeding certain thresholds of concentration. Anthropogenic sources are a major factor of Hg release into the environment, resulting in a growing awareness of this issue and leading to an increasing number of studies and therefore understanding of Hg cycling and its behavior in the environment. It has been used for anthropogenic purposes like gold mining since the roman times with a strong increase in global Hg emissions during the industrial revolution. In 2013, it was highly restricted due to the Minamata conventions with the goal "to protect the human health and the environment from the anthropogenic emissions and releases of Hg and Hg compounds." (Minamata Convention on Hg, n.d.). The UNEP (United Nations Environment Programme) also listed Hg as a priority pollutant (Futsaeter & Wilson, 2013).
However, since isotope measurement technologies have only advanced far enough to distinct heavy metals, like Hg, in the last two decades, the behavior of different Hg isotopes in natural processes is still to be understood. Better knowledge regarding this topic could lead to more efficient source tracing and better prediction of the fate of this highly toxic element.

1.1 Physicochemical properties of Hg

Mercury has a mean molar mass of 200.59 g. It is the 80th element in the periodic table and belongs to the group of transition metals. Its electronic configuration is [Xe]4f^{14}5d^{10}6s^{2}, which makes it somewhat similar to noble gases in terms of stability (Skyllberg et al., 2012). Hg is the only metal element that is liquid at room temperatures, with a melting point at -37.87 °C. This is a consequence of its weak interatomic attraction, which also causes its vapor to be monoatomic. The boiling point of Hg is at 356.57 °C (Skyllberg et al., 2012).
The elemental form, Hg(0), has a water solubility of 60 µg/L at 25 °C and can be present in liquid, aqueous but also in gaseous phases (Skyllberg et al., 2012). Hg can exist in three oxidation states throughout the environment: Metallic Hg(0), dominating the atmospheric fraction of Hg, mercurous (Hg(I)), which is by far the least abundant form due to its metastability, and mercuric (Hg(II)), which is the most abundant form in sediments, soils and water (G. Liu et al., 2012; Skyllberg et al., 2012). The three oxidation states show extremely different chemical behaviors (Blum et al., 2014). Long range transport of Hg is mainly driven by gaseous Hg in the atmosphere, which is predominantly present as Hg(0) (>90 %) (Liu et al., 2012). It also contributes to atmospheric waters as Hg(II) sorbed to particles or dissolved in droplets and further deposit to the ground (Liu et al., 2012). Mainly through oxidation by organic matter, Hg(0) can be transformed into inorganic Hg(II), which in turn may also be reduced back into Hg(0) under appropriate conditions by either organic matter, bacteria or minerals (Boening, 2000).
In liquid and solid phases (water, soils, sediments, etc.) Hg in the Hg(II) oxidation state, can be present either in organic (MethylHg, dimethylHg) or in inorganic compounds (Hg Hydroxides) and also complexed by inorganic or organic ligands (Hintelmann, 2010; Liu et al., 2012). MethylHg and Hg(II) have high affinities to reduced sulfur groups such as thiol-groups in NOM and metal sulfides, which is coherent with hard and soft (Lewis) acid and base theory (Hg^{2+}=soft acid, S=soft base) (Pearson, 1963). The only stable Hg(II)-minerals occurring at natural conditions are sulfides, like cinnabar (α-HgS) and metacinnabar (β-HgS). However, it is

also known from ore processing and mine tailings that a number of oxides and chloride minerals, like montroydite (HgO), terlinguite (Hg_2OCl) and mercuric chloride ($HgCl_2$) exist (Skyllberg et al., 2012).
The behaviour and speciation of Hg compounds changes drastically with changing redox conditions. Under oxic conditions with organic matter being present, almost all the Hg is complexed by organic thiols (Skyllberg et al., 2012). However, in anoxic surroundings, where compounds with intermediate oxidation states, like elemental sulfur, polysulfides and thiosulfides, are present, an increase of the solubility of Hg takes place due to the formation of Hg-polysulfides (Skyllberg et al., 2012).
These reactions under anoxic conditions are of high importance in terms of mobility and solubility of Hg and therefore highly investigated.

1.2 Hg toxicity effects

Mercury can occur as an inorganic pollutant, but also take part in organic compounds like methylHg (MeHg) either as monomethylHg $[CH_3Hg]+$, which is usually complexed with a negatively charged ligand or dimethylHg ($(CH_3)_2Hg$). OrganoHg compounds have the highest toxicity and, moreover, they have the highest tendency to be bioaccumulated and taken up into the food web (Futsaeter & Wilson, 2013; Liu et al., 2012). It is created by microbes in aqueous systems under anaerobic conditions (Futsaeter & Wilson, 2013). They are then taken up by larger life forms and that way further ascend trophic levels.
Inorganic Hg can harm life forms at concentrations of 5 µg/l and organoHg compounds even at values ten times lower (Boening, 2000). Especially at larval stage, aquatic invertebrates tend to show toxicity effects when fed elevated Hg concentrations and in birds inorganic Hg uptake led to poor growth, reduced food intake and several avian receptor effects (Boening, 2000).
With the exception of artisanal small scale gold miners, the risk for humans of acute Hg poisoning is quite low nowadays, however, especially through consumption of large predatory aquatic species MeHg is taken up chronically in high doses leading to several neural diseases as well as other effects like renal toxicity, myocardial infarction, immune malfunction and irregular blood pressure (Liu et al., 2012).

1.3 Sources of Hg

1.3.1 Anthropogenic sources

Anthropogenic sources are assumed to make up for about half of the Hg amount entering the environment, although the exact ratio of anthropological to natural output is to be determined (Liu et al., 2012).
The content of atmospheric Hg has increased by 450 % since the beginning of the industrial era, as historical records show and the total anthropogenic Hg aerial release per year is estimated to be 2500 ± 500 tons. (Outridge et al., 2018). The main sources of anthropological Hg emissions are attributed to fossil fuel combustion (45 %), gold (20 %), metal (10 %), cement (10 %) and dental amalgam production (2 %), the chlor-alkali industry (3 %) and waste incineration (50-470 tons) (Liu et al., 2012). Another factor of Hg pollution is its remobilization in previously affected sites and makes up for 82 ± 13 Mg Hg emissions into the atmosphere and 116 ± 49 Mg Hg release into soil and groundwater per year (Kocman et al., 2013). Nowadays, Asia is responsible for the largest amount of global Hg emissions (65 %), however, earlier developed countries like Europe and North America could have been a main driving force over the last decades (Streets et al., 2019). A region's Hg output is also connected to its

geological properties and the socio-economic alignment. For example, in South America 60 % of the annual emissions can be traced back to gold mining activities, whereas on a global scale gold production only makes up for about 20 % (Liu et al., 2012). Anthropogenic sources of Hg can emit various forms of Hg like gaseous elemental Hg (GEM, Hg^0), reactive gaseous Hg (RGM) – atmospheric Hg(II)-species present as gaseous compounds like $HgCl_2$ or $Hg(OH)_2$ or in particles - and particulate Hg (pHg) (Lindberg & Stratton, 1998; Liu et al., 2012).

1.3.2 Natural sources

Due to the complexity of natural processes emitting Hg, their total annual output is hard to be estimated quantitatively. Several studies show that it ranges from 800 to 5800 t (Liu et al., 2012). Processes causing volatilization of Hg into the atmosphere are volcanic and geothermal activities, vaporization from marine and terrestrial environments, also taking previously anthropogenically afflicted soils and substrates into account (Liu et al., 2012). In contrast to anthropogenic sources, Hg is emitted naturally predominantly (99 %) as GEM (Liu et al., 2012).

1.4 Hg isotope fractionation mechanisms

Isotopes are variations of the same element differing in their mass due to different numbers of neutrons in the atomic nucleus. Elements can exhibit various numbers of isotopes (Fry, 2006). Hg, for example has seven different isotopes: ^{196}Hg, ^{198}Hg, ^{199}Hg, ^{200}Hg, ^{201}Hg, ^{202}Hg, and ^{204}Hg (Blum et al., 2014). These variations behave very similarly in chemical reactions. However, they show slight differences in their physicochemical properties due to their different masses, nuclear volumes and other slightly different nuclear physiochemical properties resulting from quantum mechanical effects (Hoefs, 2015). For example, the lowest energy of a molecule is at the level of the lowest potential energy, but ½hv higher (h=Planck's constant, v=vibrational frequency of the atoms in the molecule), leading to a zero-point energy of the molecule even at absolute zero temperature (Hoefs, 2015). This fundamental energy depends on the mass of the molecule and the masses of the atoms involved (Hoefs, 2015). Higher mass isotopes participating in the molecule therefore cause lower zero-point energy since the vibrational frequency is lower than in the same molecule formed by lighter isotopes. This leads to the general property of heavier isotopes forming stiffer bonds in molecules than their lighter counterparts and a lower reaction rate of these heavier molecules, which is especially seen in equilibrium conditions (Fry, 2006; Hoefs, 2015).
Almost all chemical, physical and biological transformations involving any Hg species lead to fractionation of the Hg isotopes. They can either show mass dependent fractionation (MDF), mass independent fractionation (MIF) effects or both at the same time (Blum et al., 2014). For example, most biotic and dark abiotic reactions only produce MDF of Hg isotopes, whereas photochemical reactions lead to MDF as well as MIF (Blum et al., 2014). In most analytical studies of Hg isotopes, as well as in the studies done during this thesis, the Standard Reference Material (SRM) 3133 of the National Institute of Standards and Technology (NIST) is used. It has the isotopic composition listed in *table 1* (Blum et al., 2014).
Since variations of one to a few atomic mass units in the isotopes have a higher relative impact in lighter elements, the isotopes of heavy metals – like Hg – differ to a much lower degree in terms of their physicochemical properties than lighter elements like hydrogen or oxygen (Teng et al., 2017). This leads to more subtle changes to the isotopic signature in heavy elements (per mill ranges) compared to lighter elements (up to per cent ranges).

Table 1: Hg isotope abundances in the NIST-3133 standard material (Blum et al., 2014).

Isotope	Abundance in NIST-3133 (%)
^{196}Hg	0.16
^{198}Hg	10.04
^{199}Hg	16.94
^{200}Hg	23.14
^{201}Hg	13.17
^{202}Hg	29.73
^{204}Hg	6.83

1.4.1 Mass dependent fractionation

In isotope geochemistry, the lightest isotope of an element normally represents the denominator of the formula and the heaviest the nominator (Hoefs, 2015). However, this is not the case for Hg, due to the very low abundance of ^{196}Hg and the isobaric interference with ^{204}Pb of ^{204}Hg. This led to the convention that MDF of Hg isotopes is measured and presented with the ^{202}Hg / ^{198}Hg ratio. Therefore, the formula

$$\delta^{202}Hg(‰) = \left(\left[\frac{(^{202}Hg/^{198}Hg)_{sample}}{(^{202}Hg/^{198}Hg)_{SRM3133}}\right] - 1\right) \times 1000 \qquad \textit{Equation 1}$$

is used to express δ^{202}Hg-values (Blum et al., 2014).
Stable isotope fractionation can be divided in kinetic and equilibrium isotope effect. The rule of thumb regarding isotope reaction chemistry is that lighter isotopes show faster reaction rates, which leads to a higher δ^{202}Hg-value in kinetically driven reactions compared to reactions at equilibrium conditions (Fry, 2006; Wiederhold, 2015). Therefore, the change in isotopic composition of both the reactant and the products pool changes with a changing completion rate of the observed reaction. Reactant pools that underwent large depletion can show very heavy isotopic signatures (Wiederhold, 2015).
To describe this phenomenon a Rayleigh Fractionation model as shown in *Figure 1* is often used. In these plots, the delta-value of interest is represented on the y-axis and the "fraction reacted"-factor *f* on the x-axis. This factor indicates the portion of reacted atoms.
Thus, a Rayleigh fractionation-plot describes the isotopic change (in per mill) of a system with increasing completion rate. The three trend lines display the isotopic signatures of the reactant pool ($\delta_{reactant}$; red dots), the product pool ($\delta_{cum.products}$; black line) and the isotopic signature of the products at the very moment of reaction ($\delta_{inst.products}$; blue dots).
These three trend lines can be described as

$$\delta_{reactant} = \delta_0 + \varepsilon \ln f \qquad \textit{Equation 2}$$

$$\delta_{inst.products} = \delta_0 + \varepsilon \ln f + \varepsilon \qquad \textit{Equation 3}$$

$$\delta_{cum.products} = \delta_0 + \varepsilon \ln f - \frac{\varepsilon \ln f}{1 - f} \qquad \textit{Equation 4}$$

with δ_0 representing the initial isotope ratio of the reactant. The fractionation factor ε is decisive for the course of all three trend lines. Every chemical reaction involving Hg could exhibit a unique fractionation factor. However, these differences can be very subtle, and it is still to be determined to what extend they can be resolved analytically. Ideally, assumptions about the mechanism responsible for isotope fractionation during a reduction process (like photochemical vs. nonphotochemical, biotic vs. abiotic) could be made with more advanced studies of Hg isotope fractionation. The reduction experiments in this study were specifically designed to determine this fractionation factor.

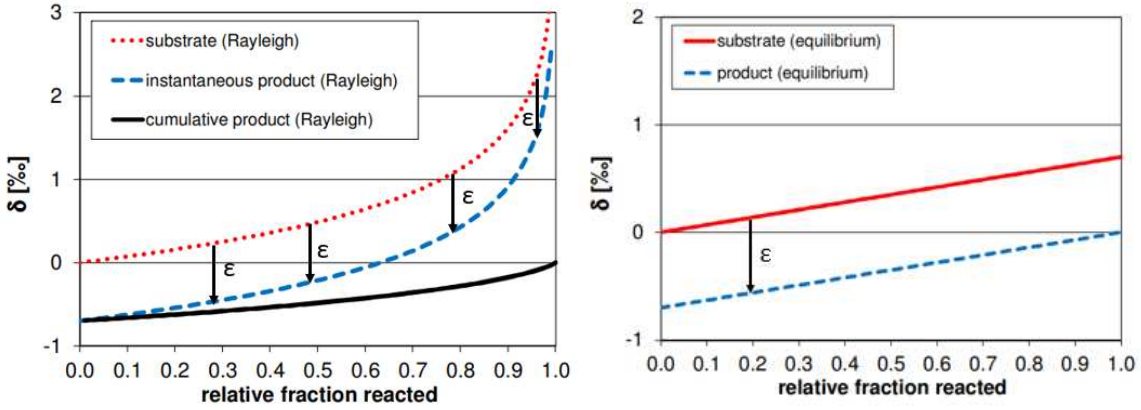

Figure 1: On the left, a Rayleigh Fractionation plot is depicted. It is valid for kinetically driven reactions or systems with no back reaction e.g. where the product is removed. On the right, the isotope fractionation of a reaction in equilibrium is shown. In both plots, the "relative fraction reacted" factor f is shown on the x-axis and the δ-value on the y-axis (adapted from Wiederhold, 2015).

1.4.2 Mass independent fractionation

In addition to MDF, some reactions can also evoke MIF, which results in slight changes of the odd-mass isotopes Hg^{199} and Hg^{201} compared to the MDF-trend the even-mass isotopes are following (Hoefs, 2015). The most common way to describe MIF of Hg isotopes is to examine the Δ^{xxx}Hg-values defined as

$$\Delta^{199}Hg = \delta^{199}Hg - (\delta^{202}Hg \times 0.2520) \qquad \textbf{Equation 5}$$

$$\Delta^{200}Hg = \delta^{200}Hg - (\delta^{202}Hg \times 0.5024) \qquad \textbf{Equation 6}$$

$$\Delta^{201}Hg = \delta^{201}Hg - (\delta^{202}Hg \times 0.7520) \qquad \textbf{Equation 7}$$

$$\Delta^{204}Hg = \delta^{204}Hg - (\delta^{202}Hg \times 1.493) \qquad \textbf{Equation 8}$$

MIF in high mass elements is generally caused by the different behavior in chemical reactions of odd-mass number isotopes due to nuclear volume effects (NVE) and magnetic isotope effects (MIE) (Wiederhold, 2015). Nuclear volume effects lead to MDF, since the nuclear radii increase with increasing mass of isotopes. However, they also account for MIF, because of small negative discrepancies from the linear correlation between increasing mass and nuclear volume in odd-mass isotopes. NVE can be observed in kinetically controlled and in equilibrium reaction conditions (Wiederhold, 2015).

Magnetic isotope effects occur in odd-mass number isotopes as a result of their magnetic moments and nuclear spin. Therefore, they only evoke MIF (Blum et al., 2014). MIE were often

observed under experimental conditions, but for most elements, the relevance and detectability of these effects occurring in nature are questionable. In the case of Hg, however, MIE induced photochemically have been proven experimentally and convenient isotopic signatures have been found in fish and precipitation (Wiederhold, 2015). In *Figure 2,* a schematic example of fractionation leading to Δ^{199}Hg and Δ^{201}Hg deviations from the general δ^{202}Hg fractionation trend is depicted.
Similar to the fractionation factor *ε*, a fractionation factor *E* can be defined for MIF occurring in a specific chemical reaction and used to trace Hg back to its source as well as for process tracing, if different processes lead to distinct MIF (Wiederhold, 2015).
The two mechanisms, MIE and NVE, lead to different relations between Δ^{199}Hg and Δ^{201}Hg. By comparing these two data sets, an assumption can be made, which of those effects is the predominant one causing MIF in a set of data (Wiederhold, 2015). To represent this data, plots with Δ^{199}Hg on the y-axis and Δ^{201}Hg on the x-axis are used to depict a linear trend line of the data cloud. The slope of said trend line is then compared to the characteristic slopes of MIE (0.9-1.3) and NVE (1.65) (Wiederhold, 2015; Zheng & Hintelmann, 2009).

To express both MDF and MIF, the most common way is to use a plot with δ^{202}Hg on the x-axis and Δ^{199}Hg on the y-axis, as shown in *Figure 3* (Blum et al., 2014). On this plot, the general isotopic fractionation trend of various reactions involving Hg can be seen. During microbial degradation of monomethylHg to Hg(0), the light isotopes were observed to be degraded faster following a Rayleigh fractionation trend of $\alpha_{202/198}$ = 1.0004 ± 0.0002 (2SD), but no significant MIF was measured (Kritee et al., 2009). In *Kritee et al., 2007* and *Kritee et al., 2008,* microbial reduction of Hg(II) to Hg(0) was found to fractionate Hg isotopes $\alpha_{202/198}$ = 1.0013 - 1.0020 and $\alpha_{202/198}$ = 1.00016 ± 0.0004 (1 SD), respectively. In dark abiotic settings, the Hg(II) reduction via $SnCl_2$ and dissolved organic matter caused MDF and MIF interpreted as NVE in the odd-mass number isotopes Hg^{199} and Hg^{201} (Zheng & Hintelmann, 2010b). The oxidation of Hg(II) in dark conditions in the presence of thiol and natural humic acid lead to MDF (ε^{202}Hg = 1.10 ‰ to 1.56 ‰) and MIF (E^{199}Hg = -0.16 ‰ to 0.18 ‰) favoring heavier isotopes in the oxidized products (Zheng et al., 2019). Photoreduction triggered by dissolved organic matter or solar irradiation causes significant MIE observable as ^{199}Hg and ^{201}Hg enrichment in the reactants (MIF) compared to the overall MDF trend (Bergquist & Blum, 2007; Sherman et al., 2010; Zheng & Hintelmann, 2009, 2010a). When complexed with organic ligands like cysteine, Hg(II) photoreduction induces MIF either in the positive or negative direction depending on the pH and in the presence of serine both MIE and NVE could be observed depending on the wavelength of the light used for reduction (Motta et al., 2020). For the volatilization of Hg(0) from the liquid phase δ^{202}Hg = 1.48 ± 0.07 ‰ was experimentally determined and first order kinetics were observed (Zheng et al., 2007). A more recent study observed how the reduction of Hg(II) with different Fe(II) bearing minerals affect Hg isotopes and determined fractionation factors of ε^{202}Hg = -2.43 ± 0.38 ‰ and E^{201}Hg = 0.28 ± 0.06 ‰for siderite and ε^{202}Hg = -2.28 ± 0.40 ‰ and E^{201}Hg = 0.28 ± 0.06 ‰for green rust, respectively (Wang et al., 2021).
For other heavy metal elements than Hg, isotope fractionation mechanisms have also been observed. For example, the mobilization of noncrystalline U(IV) by complexation of ligands such as EDTA, citrate and bicarbonate was found out to lead to isotope fractionation of δ^{238}U = 0.2 ‰ - 0.7 ‰, depending on the ligand (Roebbert et al., 2021). The isotope fractionation through microbial reduction of U(IV) to U(IV) was shown to be strongly dependent on the reaction rate (faster kinetics leading to less observed isotope fractionation) resulting in ε-values between 0.36 ± 0.07 ‰ and 0.96 ± 0.16 ‰ (Basu et al., 2020). The reduction of Cr(VI)

to Cr(III) by Fe(II) in solution and various organic showed isotope fractionation of ε = -4.20 ± 0.11 ‰ and ε = -3.11 ± 0.11 ‰, respectively (Kitchen et al., 2012).

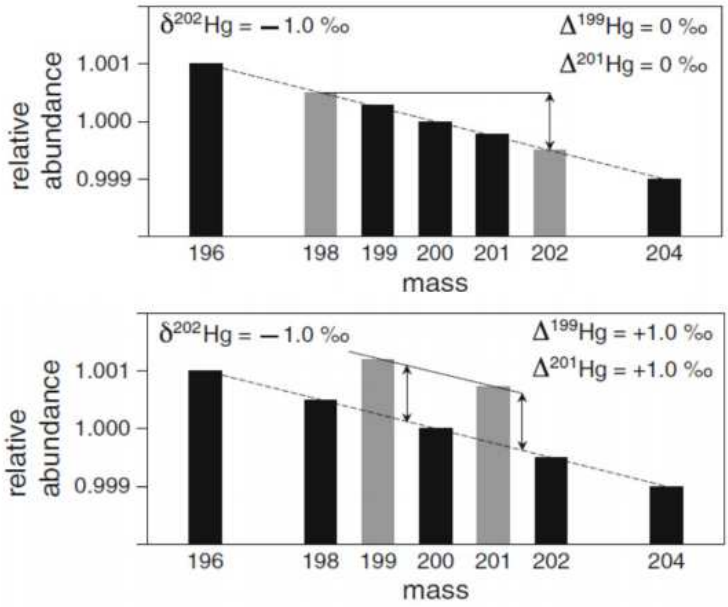

Figure 2: Difference between a process evoking only MDF in the Hg isotopes (upper graph) and a process that also causes MIF (lower graph). MIF leads to abnormal behavior of the odd-mass isotopes ^{199}Hg and ^{201}Hg compared to the MDF even-mass isotope trend. The difference between the expected MDF of the odd-mass isotopes and the observed fractionation is described as Δ^{199}Hg and Δ^{201}Hg for both odd-mass Hg isotopes, respectively. Figure taken from Blum, 2011.

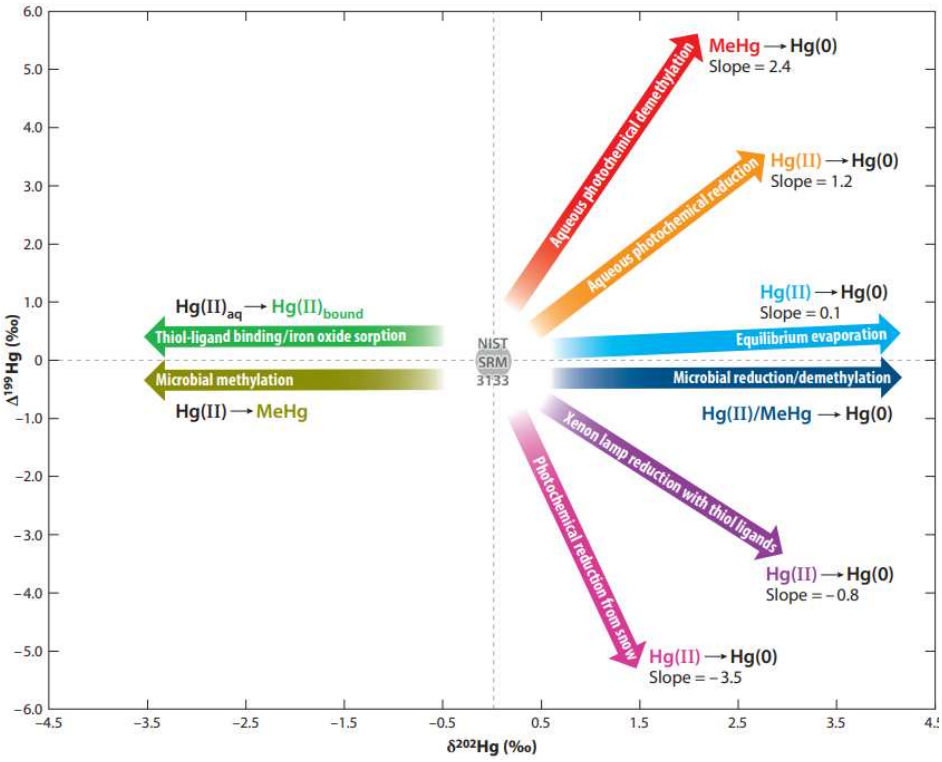

Figure 3: This plot gives an overview in which directions chemical processes occuring in nature tend to fractionate Hg isotopes. It takes both MDF (δ^{202}Hg, x-axis) and MIF (Δ^{199}Hg, y-axis) into account (Blum et al., 2014).

1.5 Hg reduction by Fe(II)

In dark anoxic iron-rich water systems (groundwater, but also in temporarily flooded soils or sediments) with low organic matter content, Hg is estimated to be reduced by Fe(II)-bearing minerals such as siderite ($FeCO_3$) (Ha et al., 2017; Wang et al., 2021), mackinawite (FeS) (Bone et al., 2014; Coulibaly et al., 2021), vivianite ($Fe_3(PO_4)_2$) (Etique et al., 2021), magnetite (Fe_3O_4) (Liu & Wiatrowski, 2018; Mishra et al., 2011; Pasakarnis et al., 2013; Wiatrowski et al., 2009), and green rust (Mishra et al., 2011; O'Loughlin et al., 2003; Remy et al., 2015). Additionally dissolved Fe(II) (Amirbahman et al., 2013; Ha et al., 2017), surface-bound Fe(II) species (Amirbahman et al., 2013; Charlet et al., 2002), and Fe(II)-bearing clays (O'Loughlin et al., 2020) were reported to be capable of reducing Hg(II) to Hg(0). This reduction of Hg(II) leads to a decrease of the more bioavailable Hg(II) concentrations and an increase of the more volatile Hg(0)-species in the water (Amirbahman et al., 2013). Several cases have been documented where flooding of oxidized Fe(III)-rich environments coupled with reductive dissolution of Fe(III) led to mobilization of Hg and therefore elevated concentrations (Amirbahman et al., 2013).

The rate determining species in the reduction reaction between Fe(II) and Hg(II) are the hydroxide species $FeOH^+$ and $Hg(OH)_2$. The concentration of both these species is favored with increasing pH, leading to faster reaction kinetics at high pH-values (observed pH values ranged from 5.5 to 8.1) (Amirbahman et al., 2013). Amirbahman et al., 2013 described the reaction rate as $r_{hom} = k_{hom}\,[FeOH^+]\,[Hg(OH)_2]$; khom = $7.19 \times 10^{+3}$ L/(mol min). An electron is first transferred from $Fe^{II}(OH)^+$ to Hg(II), resulting in $Fe^{III}(OH)^{2+}$ and an $Hg(I)_2$-intermediate species. Hg(I) is then further reduced by either another electron transfer from $Fe(OH)^+$ or disproportionation of Hg(I) to Hg(0). In both cases two $Fe(OH)^+$ are needed to reduce Hg(II) to Hg(0) (Amirbahman et al., 2013).

Although the reduction of Hg(II) in a heterogeneous system with Fe(II)-bearing mineral surfaces was enhanced, Fe(II) sorbed to an unreactive Boehmite surface (γ-Alumina) decreased the reaction rate (Amirbahman et al., 2013). In *Figure 4,* a scheme of both the homogeneous Hg(II) reduction via Fe(II) in solution and surface catalyzed is illustrated.

There are two pathways leading to the reduction of Hg(II) to Hg(0) via Fe(II). Both start with an electron transfer from the reactive species $Fe(OH)^+$ to $Hg(OH)_2$

$$\boldsymbol{FeOH^+ + Hg(OH)_2 \leftrightarrow Fe(OH)_2^+ + OH^- + Hg^+} \qquad \textbf{Equation 9}$$

The second step either follows a second electron transfer from $Fe(OH)^+$ to Hg(I)

$$\boldsymbol{FeOH^+ + Hg^+ + H_2O \leftrightarrow Fe(OH)_2^+ + H^+ + Hg(0)} \qquad \textbf{Equation 10}$$

Or Hg(I) forming a dimer (Hg_2^{2+}) which disproportionates into Hg(0)

$$\boldsymbol{Hg^+ + Hg^+ \leftrightarrow Hg_2^{2+}} \qquad \textbf{Equation 11}$$

$$\boldsymbol{Hg_2^{2+} \leftrightarrow Hg(0) + Hg^{2+}} \qquad \textbf{Equation 12}$$

In *Equation 9* and *Equation 10*, the backreactions are assumed to be very slow, as $Fe(OH)_2^+$ functions as a weak oxidant, and in *Equation 1*, the reaction is considered irreversible, since Hg(0) is immediately purged out of the system in the experimental setup. The intermediate

species Hg(I) is unstable in alkaline conditions with OH^- present (in this study: pH = 7.5-8.0). Independ of the pathway of Hg(I) transforming to Hg(0) (electron transfer from a second $FeOH^+$ as described in *Equation 2* or disproportionation of Hg_2^{2+} as in *Equation 3),* the rate determining step is considered to be the first electron transfer from $FeOH^+$ to $Hg(OH)_2$ (Amirbahman et al., 2013).

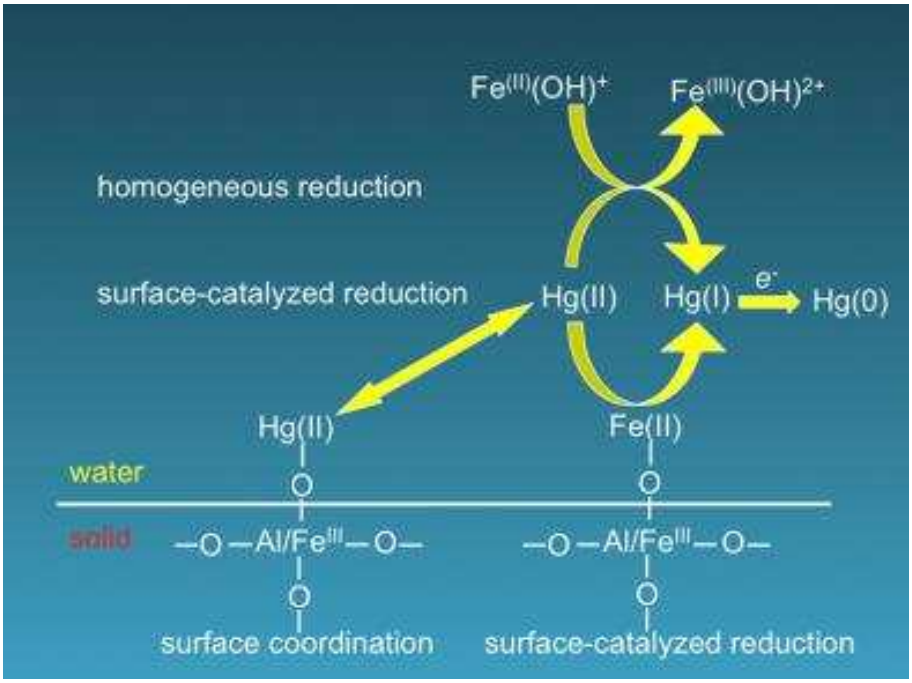

Figure 4: Schematic description of both the surface catalyzed reduction reaction between Hg(II) and Fe(II) as well as the homogeneous reduction, where Hg(II) is reduced by the first Fe(II)-hydrolysis species $Fe(OH)^+$. This graphic was taken from (Amirbahman et al., 2013).

In heterogeneous reduction processes of Hg(II) by Fe(II) as a component in various mineral forms like siderite, magnetite and vivianite, Hg(0) was produced within minutes to hours under anoxic conditions and elevated reaction rates were observed with increasing Fe(II) mineral surface area (Etique et al., 2021; Ha et al., 2017; S. Liu & Wiatrowski, 2018; Wiatrowski et al., 2009). Under sulfidic conditions, the Hg(II) forms HgS compounds and becomes complexed with S^{2-}, leading to a decrease in the reduction rate, but is still reduced by mackinawite suspensions (Bone et al., 2014; Coulibaly et al., 2021). Reduced Fe-bearing smectite minerals are also able to reduce Hg(II) to Hg(0) in the pH-range 5-9 (O'Loughlin et al., 2020). The presence of chloride hinders the reduction, since the metastable intermediate Hg(I)-species forms Hg_2Cl_2-compounds and therefore stabilizes the second part of the reduction (reduction of Hg(I) via $FeOH^+$ or the disproportionation of Hg_2^{2+}, shown in *Equation 10* and *Equation 12*, respectively) and forms $HgCl^+$, $HgCl_2$, $HgCl_3^-$ and $HgCl_4^{2-}$ leading to a lower concentration of the reactive $Hg(OH)_2$-species (Pasakarnis et al., 2013).

1.6 Goals

In this study, reduction reactions between Fe(II) and Hg(II) based on the knowledge of the reaction kinetics gained by in previous studies, were conducted with both species in solution

(homogeneous experiments) and with Fe(II) sorbed to an unreactive Boehmite surface (heterogeneous experiments) (Amirbahman et al., 2013; Ha et al., 2017).
A series of pre-experiments had to be conducted to find proper settings in terms of electrolyte content, pH, Hg, and iron starting concentrations and, for the case of the heterogeneous experiments, the right Boehmite surface area. To satisfy the MC-ICP-MS sensitivity of the Hg isotope analysis, sample volume and Hg starting concentrations had to fulfil quantitative requirements. Compared to other studies, not only the accumulation of the reacted Hg fraction in a trap vial was monitored, but also the mass loss in the reactor, to increase data quality and keep track of the mass balance at every sampling point.
Advanced Hg isotope analysis methods were applied to observe isotope fractionation mechanisms of these reactions and determine the MDF-factor ε and MIF-factor E, as well as the predominant effect causing MIF. The following questions were addressed in this work:

Question 1

In which way are Hg isotopes fractionated during the reduction reaction with Fe(II) in solution, in terms of MDF as well as MIF?

Question 2

How is the isotope fractionation affected, if the reduction of Hg is induced by Fe(II) sorbed to an unreactive boehmite surface instead of dissolved in water?

Question 3

How do the observed isotope fractionations of the homogeneous and heterogeneous experiments compare to isotope behavior of previously investigated reactions including Hg?

As previously shown, most Hg reduction reactions investigated so far fractionated isotopes in quite similar ways with MDF favoring the lighter isotopes. It is fair to assume the same trend for the reduction reaction with Fe(II) in solution and the reaction with Fe(II) sorbed to Boehmite. However, since Boehmite slows down the reduction process, the fractionation factor could also change compared to the homogeneous reaction, as kinetics were shown to impact on that matter. For microbial U(VI) reduction, for example, a clear correlation between the reaction rate and the isotope fractionation was observed, which resulted in decreasing ε with increasing rate constants (Basu et al., 2020). In a general approach to relate U isotope fractionation in kinetically driven reduction processes by Fe(II)-species with free energy, the fractionation factor was observed to be log-linearly correlated with the reduction rate (Joe-Wong et al., 2021). *Kavner et al., 2005* investigated the effect of changes in applied electrochemical potential on Fe isotope fractionation and observed voltage dependency of the fractionation, similar to the correlation of isotope fractionation and reduction reaction kinetics observed in nature. They postulated, that the impact of electron transfer on kinetics and isotope fractionation could be inherently correlated, not only for Fe but for transition metals with multiple isotopes in general.
However, to what extent the addition of the sorption process plays into the overall fractionation outcome in the heterogeneous reduction is hard to tell, as it is poorly

investigated so far. *Jiskra et al., 2012* suggested that the sorption process of Hg(II) fractionates Hg isotopes in favor of the lighter ones independently from the specific surface, which is therefore also expected for the sorption to Al_2O_3. Reaction kinetics can have an impact on isotope fractionation and *Amirbahman et al., 2013* observed a decrease in reaction rate for the reduction of Hg(II) with Fe(II) with Al_2O_3 present as an unreactive surface. This change of reaction kinetics could be reflected in the isotope results of this study to some degree. MIF is hard to predict, since previously investigated reduction mechanisms lead to either positive or negative MIF or showed no measurable deviation of Hg^{199} and Hg^{201} from the MDF trend. The Hg^{199}/Hg^{201}-slope is expected to follow the NVE trend in the homogeneous as well as in the heterogeneous reduction experiments, as dark abiotic reduction experiments of Hg(II) also observed NVE (J. G. Wiederhold et al., 2010).

2. Materials and methods

2.1 Chemicals

Anoxic H_2O: In the experiments, only anoxic water was used, to reproduce anoxic conditions. For this purpose, ultrapure water coming from a Millipore system with > 18 MΩ·cm resistivity and < 2ppb TOC was boiled for about half an hour and afterwards purged with Nitrogen gas for at least three hours. Then it was sealed with a butyl-rubber stopper and brought into an anoxic chamber manufactured by Coy Laboratory Products, Grass Lake, MI as fast as possible. The glovebox atmosphere consisted of Formier gas containing ~3 % Hydrogen and ~97 % Nitrogen.

Hg: For all the Hg containing experiments the NIST-3133 standard was used. Its known isotopic signature led to an easy handling of the data gathered in the MC-ICP-MS and to a high reproducibility of the conducted experiments. It is stored in the laboratory at University Vienna as a 1000 ppm stock solution in a 10 % (v/v) HNO_3 matrix.

Al_2O_3: The Boehmite solid particles used as reaction inhibitor (Amirbahman et al., 2013) were manufactured by *Condea Chemie.* This material was well described by Nordin et al., 1997. Inductive Coupled Plasma – Atomic Emission Spectroscopy showed that its purity is 99.2 %, with the main contaminating elements being potassium, magnesium, sodium and silicon. The measured mineral surface area was 180 m^2/g. XRD-measurement was also conducted at University of Vienna to specify the crystallographic structure. The analyzed XRD pattern is shown in *Figure 6.* It was stored in the plastic bottle provided by the manufacturer and weighed in just before the start of the experiments.

BrCl: The 0.2 M BrCl-Solution was prepared in the laboratory in a fume hood following the protocol of *Bloom et al., 2003*. The reagents KBr and $KBrO_3$ were heated up to 220 °C for 24 h before use, to vaporize any potential Hg contamination (Bloom et al., 2003). 5.4 g KBr were added to 500 ml HCl conc. and stirred with a magnetic stirrer for 1 h. Afterwards, 7.6 g $KBrO_3$ were added. Since the addition of $KBrO_3$ releases Cl_2 and Br_2, this was done slowly and carefully. After another hour of stirring, the bottle was sealed and stored in a fridge. This solution will be referred to as "BrCl conc." in this thesis. Diluted solutions are presented as % (v/v) BrCl. For example: 1 % BrCl means a ratio of one part BrCl conc. to 99 parts H_2O.

Inverse Aqua Regia: The 40 % (v/v) inverse aqua regia solution used in the experiments to capture and oxidize the previously reduced Hg(0) was prepared shortly before experimental start. Three parts HNO_3 conc. (65 % p.a.) and one part BrCl conc. were added to six parts H_2O.

$FeCl_2$: The Fe(II)Cl_2-stock solution used in the experiments was manufactured by Merck Millipore and purified in the laboratory following the description of *Dideriksen et al., 2015,* with some slight adjustments in an anoxic Coy-Tent. The Fe(II)Cl_2- stock solution was produced by dissolving 13.421 g Fe(II)$Cl_2 \cdot 4H_2O$ in 45 ml anoxic water inside the coy-tent (aiming for c = 1.5 M). To exclude Fe(III) impurities, 6 M NaOH was added to bring the pH up to a value of 6 in order to precipitate Fe(III) as a green slurry. The 50 ml vial was then capped and sealed with parafilm, brought out of the chamber to be centrifuged at 2000 rcf for 30 seconds and brought back in. Inside it was filtered and its pH was then adjusted to 3 with 6 M HCl. Its Iron concentration was later characterized by ferrozine assay and UV-VIS using a multi plate reader (Tecan Infinite 200 Pro) as c(Fe(II)) = 1.25 M.

For each experiment that was conducted outside the anaerobic chamber, the Fe(II) stock solution was transferred into a smaller 15 ml centrifuge vial inside the chamber, diluted to reach the wanted concentration and sealed with parafilm and then transferred to a benchtop glove bag (AtmosBag, Sigma-Aldrich), where the experiment was conducted at.

2.2 Mineral synthesis

For further investigations of the behavior of Hg isotopes during the reduction through Fe(II)-bearing minerals, siderite, mackinawite, pyrite and magnetite were synthesized and characterized. Those minerals were chosen due to their relevance and abundance in natural systems. Unfortunately, these experiments could not be covered in the extent of this thesis, but the synthesized minerals will provide a valuable basis for future experiments. All syntheses were conducted in an anoxic glove box and deoxygenated water was used exclusively.

2.2.1 Siderite ($FeCO_3$)

For the synthesis of siderite, the protocol of (Dideriksen et al., 2015) was followed with some slight changes of concentrations. The previously described $Fe(II)Cl_2$- stock solution was diluted to reach a volume of 300 ml with $c(Fe(II)Cl_2)$ = 150 mM. A $NaHCO_3$ -solution was produced inside the anoxic glovebox by adding 3.780 g of $NaHCO_3$-salt to 300 ml anoxic water (c = 150 mM). By mixing these two solutions, a milky white suspension was formed. After seven days, the solution on top of the precipitant was discarded and the remaining siderite was transferred to 50 ml vials and washed three times with anoxic water. Between each washing step, the vials were capped, sealed with parafilm, brought out of the Coy-tent and centrifuged at 6000 rcf for one minute. After washing, the mineral slurries were transferred to a 100 ml serum bottle and sealed with butyl-rubber stoppers.

2.2.2 Mackinawite (Fe_9S_8) and pyrite (FeS_2)

The synthesis of Mackinawite and Pyrite only differs in growth time. Two solutions were prepared: 0.625 M $FeCl_3 \cdot 6H_2O$ (6.758 g dissolved in 40 ml deoxygenated H_2O) and 0.625 M $Na_2S \cdot 9H_2O$ (6.005 g dissolved in 40 ml deoxygenated H_2O). In four serum bottles, 8 ml $FeCl_3$ were diluted with 84 ml anoxic water respectively while stirring. Then, 8 ml per bottle Na_2S-solution was added. Black precipitation was formed immediately.
For Mackinawite synthesis the substances of two bottles were washed three times inside the coy chamber promptly afterwards. After each washing step, the slurries were centrifuged.
For Pyrite synthesis two bottles were sealed with butyl rubber stoppers and aluminum crimps and placed on a lateral shaker for four weeks outside the coy chamber at room temperate. Afterwards, the slurry was transferred to 50 ml vials and washed in the same manner the siderite was (Morin et al., 2017).

2.2.3 Magnetite (Fe_3O_4)

To synthesize magnetite, the protocol of *Wang et al., (2011)* was followed. 4 ml of the $Fe(II)Cl_2$-stock solution were diluted in a glass serum bottle to reach 5 ml $c(Fe(II)Cl_2)$ = 1 M. 10ml 1 M $FeCl_3$-solution was added (2.701 g $FeCl_3 \cdot 6H_2O$ in 10 ml deoxygenated H_2O). After the addition

of 60 ml 1 M NaOH, black precipitation could be observed. After two days, the magnetite was transferred to 50 ml vials and washed three times. Between each washing step, the vials were capped, sealed with parafilm, brought out of the anoxic glovebox and centrifuged at 6000 rcf for one minute. After washing, the mineral slurries were transferred to a 100 ml serum bottle and sealed with butyl-rubber stoppers.

2.3 Hg(II) reduction by Fe(II)

2.3.1 Experimental setup

The experimental setup was inspired by previous works as described, for example, in *Zheng et al., 2007* or *Zheng & Hintelmann, 2009*. Its purpose was to provide anoxic reaction conditions for the reduction of Hg(II) to Hg(0) by Fe(II). The reduced Hg transitions into the gaseous phase (Fry, 2006). The process of transferring the reduced Hg was accelerated by a constant nitrogen gas flow in the reactors. To measure the recovery and provide an analytical counterpart pool, the purged Hg was transferred via a PTFE tube and captured in a 40 % inverse aqua regia (3:1 HNO_3:BrCl) trap liquid that oxidizes the Hg^0 back to the Hg^{2+}-state stabilizing it in solution (Janssen et al., 2019). To get an overview of the reaction kinetics and, especially, to generate meaningful isotope fractionation data, several sampling points were taken during the proceeding experiment. A sketch of the experimental set up is shown in *Figure 5.*
Three 100 ml or 250 ml glass bottles functioning as reactors were placed inside a glove bag, which had previously been flushed with nitrogen gas to reach oxygen levels below 1 %. For the purpose of these experiments, this was considered sufficient because the reaction bottles represent a more or less closed system and were also constantly purged with nitrogen gas and sealed with PTFE lids with three valves. One for the inlet tubes, one for the outlet tubes and one to sample the reaction fluid during the experiments. In the tubing system between the gas bottle and the reaction bottles a gas flow meter to regulate the gas flow and a gold trap to bind eventual Hg impurities in the nitrogen gas were installed. To provide a long contact time between the nitrogen gas and the reaction fluid and therefore efficiently purge out all reduced Hg as fast as possible, the inlet tube was placed far to the ground of the reactor. Magnetic stirrers were used to constantly move the liquid and homogenization of the system. Each reactor was connected to a 60 ml PFA gas washing bottle containing the trap solution via a PTFE tube and a glass frit. The glass frits were placed to the bottom of the trap vessels to maximize contact time of the Hg containing nitrogen gas and the trap liquid to efficiently oxidize and stabilize all the Hg purged out of the reactors. The PTFE tubes and the glass frits were treated with 5% BrCl overnight, similar to *Amirbahman et al., 2013*.

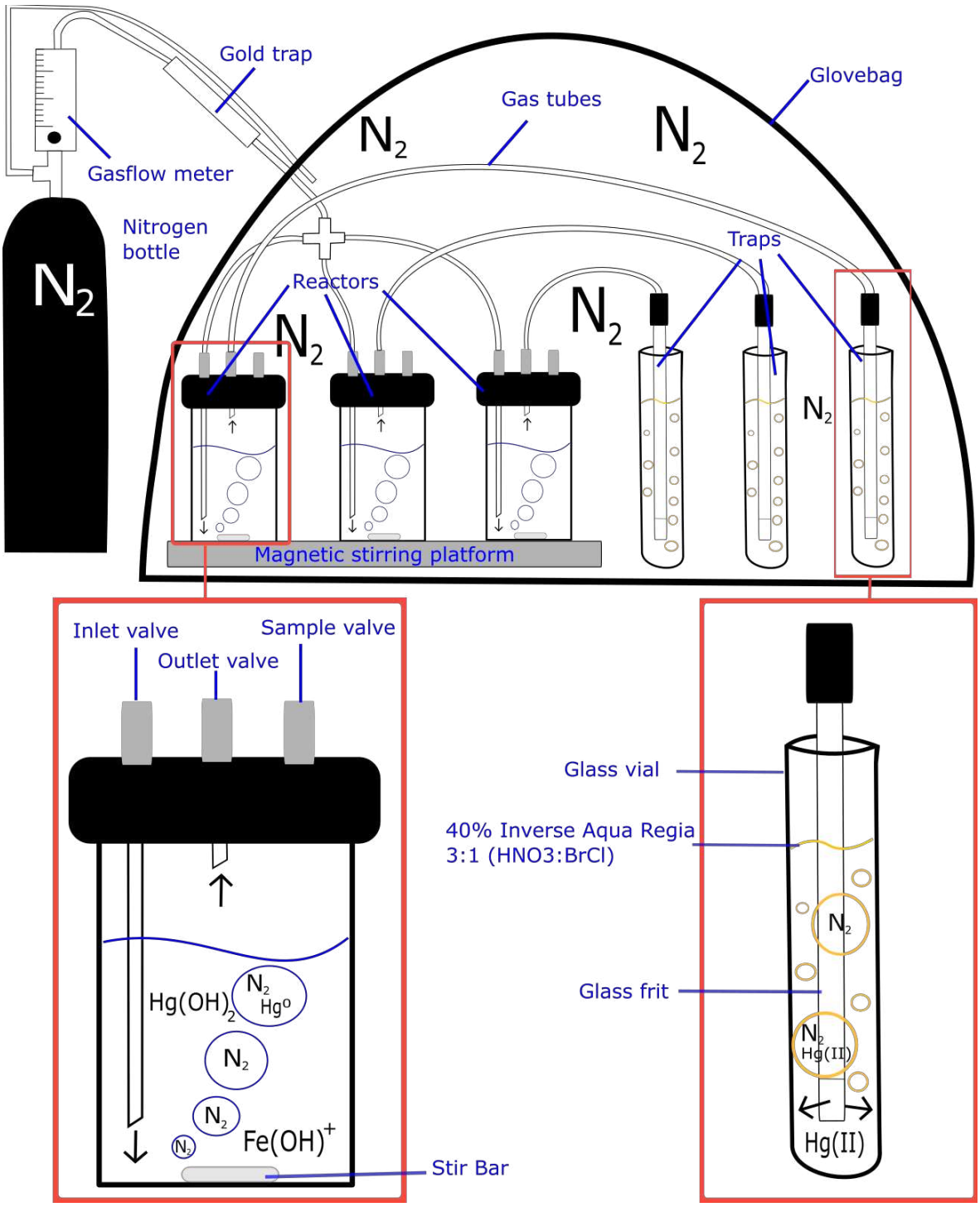

Figure 5: Sketch of the set-up used for the reduction experiments.

2.3.2 Hg and Fe-speciation modelling

To assess the impact of varying starting concentrations of different components in the reactor solution on Hg and iron speciation in solution, equilibrium speciation models were generated with the default database of visual MINTEQ. The effect of different NaCl-concentrations on said predominant iron and Hg species were compared and the change of the reactive species

$FeOH^+$ and $Hg(OH)_2$ during the course of the experiment and the resulting Hg and Fe(II) losses were depicted.

2.3.3 Homogeneous reduction with $FeCl_2$ in solution

Settings for a reduction reaction of Hg(II) and Fe(II) that takes place only in solution and under anoxic conditions were tried to be generated. For this purpose, the previously described experimental set-up was used.

At the beginning of the experimental phase of the studies for this thesis, the aim was to find the most fitting concentrations of NaCl and $FeCl_2$ for reaching reaction kinetics that would lead to meaningful data in terms of isotope analysis (even at late stages of the experiment – when more than 50 % of the initial Hg reacted - large enough volume in the reactor and Hg concentration high enough for the MC-ICP-MS analysis). To do so, initially only the Hg concentrations were measured and not the isotope composition. To examine if there is a reduction reaction with no Fe(II) in the system, several blank experiments with the same starting concentration of Hg, but without the addition of $Fe(II)Cl_2$ were conducted. Based on previous work from *Amirbahman et al. (2013)* and the results from speciation modelling the pH was adjusted to a value of 8. A pH-buffer (PIPPS (1,4-Piperazine-N,N'-bis(propanesulfonic acid)), MOPS (3-(N-morpholino)propane sulfonic acid)) was added at a concentration of 20 mM to keep the pH constant. A lot of trial runs had to be done in to find conditions fitting for the purpose of this thesis. A table with the starting conditions of all the experimental runs of the homogeneous experiments (also including the trial runs) is given in the appendix in *Table A1.*

Due to the initially faster reaction kinetics (Amirbahman et al., 2013), more frequent samples were taken at the beginning of the experiment. After one hour, samples were taken in 60-minute intervals. At each step the reactor and the trap solution were sampled. Conditions for each experimental run that led to data considered robust enough and therefore discussed in this work are summarized in *Table 2*.

Table 2: List of initial concentrations of chemicals used in the respective homogeneous experiments.

Experiment	Hg (µmol/l)	$FeCl_2$ (µmol/l)	NaCl (µmol/l)	pH	Buffer	Date
Hom N	0.5	12.5	342.2	8.0	MOPS	2020-10-28
Hom Q	0.5	12.5	342.2	8.0	MOPS	2020-11-11
Hom R	0.5	12.5	342.2	8.0	MOPS	2020-11-11
Hom S	0.5	12.5	342.2	8.0	MOPS	2021-01-15

2.3.4 Sorption experiments for heterogeneous reduction experiments

A series of sorption experiments were conducted with the same chemical background in terms of electrolyte concentration and pH to find a suitable alumina surface area for the heterogeneous reduction experiment. The goal of these experiments was to find the optimal surface area to provide enough sorption sites to adsorb almost all the Fe(II) to the Al_2O_3. This is necessary to ensure that the observed reduction is indeed surface catalyzed and not occurring in solution as in the homogenous case. As *Amirbahman et al., 2013* stated, with

increasing Alumina surface, the Hg^{2+} reduction reaction shows a decreasing reaction rate. Increasing the Al_2O_3 content too much to ensure complete Fe(II) sorption would therefore slow down the reaction. There are a handful of problems coming alongside slowing down the reaction kinetics too much:

- Compensating for the decrease in reaction rate would lead to worse comparability of the gathered data to the homogeneous experiments conducted beforehand, since options to do so would be changing of the chemical background (electrolytes, buffer, pH) or significantly increasing Hg concentrations during the experiment, and therefore sacrificing the similarity of the experiments with natural systems.
- To create meaningful isotope data, it is critical to have a certain amount of the Hg^{2+} reacted at the time of the last sampling point, as described in section *2.3.3.*.
- Constant nitrogen gas flow is needed to keep the system anoxic. Longer reaction time would force a gas bottle exchange and therefore a gas flow stop during the experiment.
- A longer experiment time would increase the chance of oxygen infiltration into the system.

In case of an Alumina surface area, that cannot adsorb all the iron, the observed reaction takes place partly in solution. Given the fact, that the reduction in solution also is faster than it is on the non-reactive Alumina surface, this would only mimic, at least to some degree, the entirely homogeneous reaction.

Table 3: List of initial concentrations of chemicals used in the respective sorption experiments.

Reactor	vol (l)	$FeCl_2$ (µmol/l)	Hg (µmol/l)	Al_2O_3 (g/l)	Al_2O_3 (m^2/l)
SorpA	0.1	62.5	0	2.0	360
SorpB	0.1	62.5	0	2.0	360
SorpC	0.1	62.5	0	5.0	900
SorpD	0.1	62.5	0	5.0	900
SorpE	0.1	62.5	0	15.0	2700
SorpF	0.1	62.5	0	15.0	2700
SorpG	0.1	0	0.5	2.0	360
SorpH	0.1	0	0.5	2.0	360
SorpI	0.1	0	0.5	5.0	900
SorpJ	0.1	0	0.5	5.0	900
SorpK	0.1	0	0.5	15.0	2700
SorpL	0.1	0	0.5	15.0	2700
SorpM	0.1	0	0.5	25.0	4500
SorpN	0.1	0	0.5	25.0	4500
SorpO	0.1	0	0.5	40.0	7200
SorpP	0.1	0	0.5	40.0	7200
SorpQ	0.1	62.5	0	25.0	4500
SorpR	0.1	62.5	0	25.0	4500
SorpS	0.1	62.5	0	40.0	7200
SorpT	0.1	62.5	0	40.0	7200
SorpU	0.1	0	0	0	0
SorpV	0.1	0	0	0	0

The sorption experiments were conducted in the glovebox and only anoxic deoxidized MilliQ-water was used. As in the homogeneous and the heterogeneous experiments, 342.17 µmol/l NaCl was added to each reaction bottle. The pH was adjusted by pipetting 1 M NaOH to reach a value of 8 and buffered with 20 mM MOPS. Different amounts of aluminum-oxide were tested with consistent $FeCl_2$ and Hg(II) concentrations separately. In *Table 3*, a list of the Al_2O_3 m^2/l as well as the associated starting concentrations is provided. For all the different starting concentrations a duplicate reactor bottle was provided to improve data quality. Reactors U and V were added as blank reactors to check for potential Hg contaminations in the system.

2.3.5 Heterogeneous reduction with $FeCl_2$ sorbed on Al_2O_3-surface

The heterogeneous experiments were conducted based on the knowledge gained from the homogeneous reduction experiments and also on the information gathered in the sorption experiments. The experimental setup illustrated in *Figure 5* was used.
In all cases, pH was buffered at 8 with 20 mM MOPS and 342.2 µM NaCl was added as background electrolyte to create conditions that are as comparable to the homogeneous reduction data as possible. *Amirbahman et al., 2013* stated, that the reduction of Hg(II) by Fe(II) was slowed down by the addition of Al_2O_3, which led to an inevitable elevation of Hg and/or iron to drive the reaction to a degree that grants meaningful and explicit isotope data, as discussed in the introduction of this thesis. Another option would have been to increase the reaction time. The reduction was described to exhibit second order reaction rate depending on Fe(II) and Hg concentrations, so increasing either one of those would accelerate the reaction rate (Amirbahman et al., 2013). The reactor solution with the Al_2O_3 particles in suspension were prepared in the anoxic glove box the day before the experiments were conducted, including all the chemicals except for Hg, to expand the period of Fe(II) sorbing to the Al_2O_3 particles. The pH was adjusted to 8.0 and was also measured in the next morning to confirm that there are no changes. Overnight, the suspension was constantly stirred.
In the heterogeneous experiment the reactor was sampled twice at each time step. The first one unfiltered and a second one using a 0.2 µm cellulose acetate syringe filter before transferring it to the sample tubes. In both sample tubes BrCl conc. was added to reach a final concentration of 2 % of the sampled volume to stabilize the Hg in the sample immediately.
After experiment stop, the unfiltered samples were acidified to reach c(BrCl conc.) = 10 % to desorb all the Hg from the Alumina. Then they were centrifuged at 2000 rcf for 0.5 minutes. The supernatant was subsequently diluted with 1 % BrCl or water to reach c(BrCl) = 1 % in the samples for the concentration analysis.
The purpose of taking two samples – one filtered directly and an unfiltered one - is to be able to differentiate between the fraction of Hg in solution and the fraction sorbed to the Al_2O_3-particles in terms of concentration as well as in terms of the isotopic signature. The samples filtered during the experiment were supposed to show the signature of only the Hg in solution and the unfiltered and then desorbed samples should inherit the signature of both the Hg in solution and the Hg sorbed to the Alumina. Calculating the difference in pool size could show how much of the Hg sorbed to the Alumina and the isotope ratios of the respective pool allows to assess if the sorption process itself fractionates the Hg isotopes.

In *Table 4*, the initial concentrations for the heterogeneous reduction experiments discussed in this work are listed. In the appendix in *Table A2*, also the experiments not considered for this study are included.

Table 4: List of initial concentrations of chemicals used in the respective heterogeneous experiments. For all the experiments, pH was adjusted to 8.0 and 20 mM MOPS was used as buffer.

Experiment	Hg (µmol/l)	$FeCl_2$ (µmol/l)	NaCl (µmol/l)	Al_2O_3 (m^2/l)	Date
Het F	5.0	69.3	342.2	4500	2021-04-08
Het G	5.0	69.3	342.2	4500	2021-04-08

2.4 Analysis

2.4.1 Hg concentration analysis

To determine the Hg concentration of the samples taken during all experiments, a DMA-80L Direct Hg Analyzer manufactured by Milestone Inc. was used. This instrument uses a cold-vapor system to introduce the Hg followed by amalgamation and atomic fluorescence and absorption spectrometry (CV-AFS/AAS).
Before the measurement, the pump of the instrument was always freshly calibrated, and a new calibration file was created by measuring volumes of 1 ml, 2 ml and 3 ml of solutions with known concentrations between 0 and 5 µg/l, leading to a calibration curve from 0 to 15 ng of Hg input. These solutions were either mixed on the day of measuring or a maximum of a few days beforehand. They were always produced in a 1 % BrCl matrix. The cold vapor system utilizes reduction of all Hg in the samples by mixing them with a $SnCl_2$-solution (2 % (w/v) $SnCl_2$ in 2 % (v/v) HCl) and removes the produced Hg(0) by continuously purging with Argon (Ar) gas. The samples were always pre-diluted with 1 % BrCl-solution to match the calibration range and pre-reduced shortly before insertion into the instrument with 20 µl of 30 % (v/v) hydroxylamine-hydrochloride (NH_2OH-HCl) following EPA method 1631 (EPA, 2002). For samples with higher BrCl-concentration, higher NH_2OH-HCl volumes were added to counterbalance the oxidizing effect of the BrCl. The calibration solutions were pre-reduced in the same manner. After at least every tenth sample, a standard sample of the calibration solution and a blank solution were measured, to validate the ongoing measurement and exclude possible carry over.

2.4.2 Hg isotope analysis

The samples gathered during the experiments were analyzed with a Nu Plasma II multi-collector inductively- coupled plasma mass spectrometer (MC-ICP-MS) manufactured by Nu Instruments. Before measuring, the samples were concentration matched by diluting with 1 % BrCl solution to c(Hg) = 10 µg/L, in rare cases also to c(Hg) = 5 µg/L or c(Hg) = 2.5 µg/L. To reduce Hg(II) in the samples to Hg(0), a HGX-200 Cold Vapor System (Teledyne CETAC) mixing the sample with a $SnCl_2$-solution (2.5 % (w/v) $SnCl_2$ in 1 M HCl) was used. Through a constant Ar gas flow, the Hg-bearing vapor was carried to the plasma torch.
On each day of measuring, the instrument was tuned to obtain the most stable and highest signal possible, with the priority focusing firstly on the stability and secondarily on the signal

height. Tuning parameters involved in obtaining optimal signal included an automatic pre-amplifier gain calibration routine, adjustment of shape and coincidence of the signal peaks and manually adjusting the torch position, gas flows and the voltages on the focusing lenses. To tackle the instrumental mass fractionation (mass bias), two correction methods were used, based on the works of *Wiederhold et al., 2010*:

1. Standard sample bracketing: between every sample a standard sample with known isotopic signature (NIST 3133) was analyzed, outlining the 0-value on the y-Axis in the fractionation plot. Every sample was mathematically set in relation to the standard measured immediately before and after. The Hg concentration was always adapted to the concentration of the analyte.
2. Element doping: Through an Aridus II desolvating nebulizer system manufactured by Teledyne Cetac, Omaha, USAA a Tl standard (NIST-997) aerosol of known isotopic composition was generated and introduced to the MC-ICP-MS along with every sample measured. By comparing the known and measured values of the Tl standard, the mass bias of the instrument had been observed and corrected during the measurement.
3. For further validation of the accuracy and precision of the data gathered in the MC-ICP-MC, at least four samples of a secondary standard ("ETH-Fluka") were measured throughout a session. They were used to define the standard deviation of each day of measurement. The error bars shown in the graphs of the Hg isotope data results show the double of the standard deviation of the Fluka measurements on each day of analysis.

2.4.3 Iron analysis

Dissolved Fe(II) and Fe(III) were determined by colorimetry, using the ferrozine assay (Stookey, 1970; Viollier et al., 2000). For total iron (Fe(tot)) concentrations, aliquots were reduced with 10 % w/v hydroxylammonium hydrochloride ($NH_2OH{\times}HCl$) dissolved in 1 M HCl. Fe(II) and Fe(tot) samples were mixed with a 0.1% w/v solution of ferrozine in 50 % w/v ammonium acetate buffer. Absorbance was measured at 562 nm in microplates with a plate reader (Tecan Infinite 200 Pro).

2.4.4 Inductively coupled plasma – mass spectrometry (ICP-MS)

Inductively coupled plasma mass spectrometry (ICP-MS) was used to determine the effect of the Al_2O_3 on Fe in the reactor solution in the sorption experiments. For this purpose, an Agilent 7700 was utilized, and samples were acidified and stabilized with trace metal grade 1 % HNO_3.

2.4.5 XRD

Some of the synthesized minerals and the Al_2O_3 manufactured by *Condea Chemie* were analyzed with powder X-ray diffraction (XRD). A Rigaku Miniflex 600 was used. The minerals containing Fe(II) were dried in the anaerobic Coy-tent and carefully applied on an air-tight sample holder to avoid any oxidation before the XRD-analysis.

2.5 Calculation of the mass dependent fractionation factor ε:

The *f*-value was calculated using the Hg concentration results of the trap samples and total mass of Hg at each time step.

$$f_t = \frac{m(Hg_{tot})_t - m(Hg_{trap})_t}{m(Hg_{tot})_t} \qquad \textbf{Equation 13}$$

The isotope fractionation of an element in a kinetically driven reaction can be calculated as

Equation 2 for the reactant pool,

Equation 3 for the isotopic signature of a product at the time it has reacted and

Equation 4 for the pool of cumulated reacted atoms.

The data gathered in this study represents the reactant pool (reactor samples) and the cumulative products (trap samples). At the beginning of the reaction, or rather when f = 1, the logarithmic term of the equation for the prediction of the reactant pool becomes zero. What is left is the equation

$$\delta_{reactant} = \delta_0 \qquad \textbf{Equation 14.}$$

By calculating a logarithmical trend line for the data set of the measured samples of the reactants of one experiment, a logarithmic term and a constant term is shown. The constant term shows the δ_0-value.

Calculating the cumulative product at the same point of the reaction (f = 1) is not possible since the denominator in the third term of the equation becomes zero. However, as visible in the Rayleigh fractionation plot *Figure 1*, at point f = 1, $\delta_{inst.products} = \delta_{cum.products}$ can be assumed.

$$\delta_{cum.products} = \delta_0 + \varepsilon ln\, f + \varepsilon \quad \textbf{(Only valid for f=1)} \qquad \textbf{Equation 15}$$

Like for the reactant pool, the logarithmic term becomes zero and what remains is

$$\delta_{cum.products} = \delta_0 + \varepsilon \qquad \textbf{Equation 16.}$$

Again, a logarithmical trend line is calculated for the data set of the cumulative products of the same experiment as the reactor samples. The constant term of the trend line equation equals $\delta_0 + \varepsilon$. Given that the constant term of the reactor trend line equation equals δ_0, the difference between these two values is the wanted value ε, the fractionation factor of the experiment.

Using this method, ε was calculated for HomN and HomR, respectively. A Rayleigh fractionation plot was made with the three calculated trend lines using these ε-values and the data set of the two experiments were fitted.

2.6 Calculation of the reaction rate in the homogeneous experiments

Based on the observations of the homogeneous reaction reduction experiments, the rate constant was calculated and compared to k-values found in literature for this specific reaction. First, the average Hg concentration values of several experiments at each measured time step (30, 60, 120, 180 and 240 minutes after experiment start) were calculated. To establish the

$FeOH^+$ and $Hg(OH)_2$ concentrations (according to the research of *Amirbahman et al., 2013,* these species are the most reactive and therefore most relevant for the reaction kinetics) for each time point, a vMinteq model was created with its actual measured Hg concentration in the reactor and the theoretical Fe(II) concentration at that point. A loss of two mol/l Fe(II) concentration was assumed for one mol/l Hg concentration decrease in the reactor. Using the excel solver function, a sum of squared residuals- fit for the rate constant was calculated for the average reactor data.

Moreover, the average reactor values were linearized according to both the first and second order linearization rules following *Brezonik, 2015*. For each time step, a rate constant k was calculated in reference to the starting concentrations of $Hg(OH)_2$ and - in case of the second order linearization – $FeOH^+$ Based on these rate values, two rate constants were calculated for both the first and second order linearization: (a) A mean value of rate constants calculated for each individual sampling point in respect to the starting concentrations and (b) a graphical solution with the slope of the linear trend line fitted for all the linearized mean values of the investigated homogeneous reduction experiments (first order and second order assumptions, respectively).

3. Results

3.1 XRD mineral analysis results

The synthesized siderite and magnetite minerals and the Al_2O_3 (*Condea Chemie*) were analysed using powder X-ray diffraction. All results are depicted in *Figure 6.* The signal peaks (light blue) of all three materials can be fitted well with the theoretical peaks (red) of the corresponding materials.

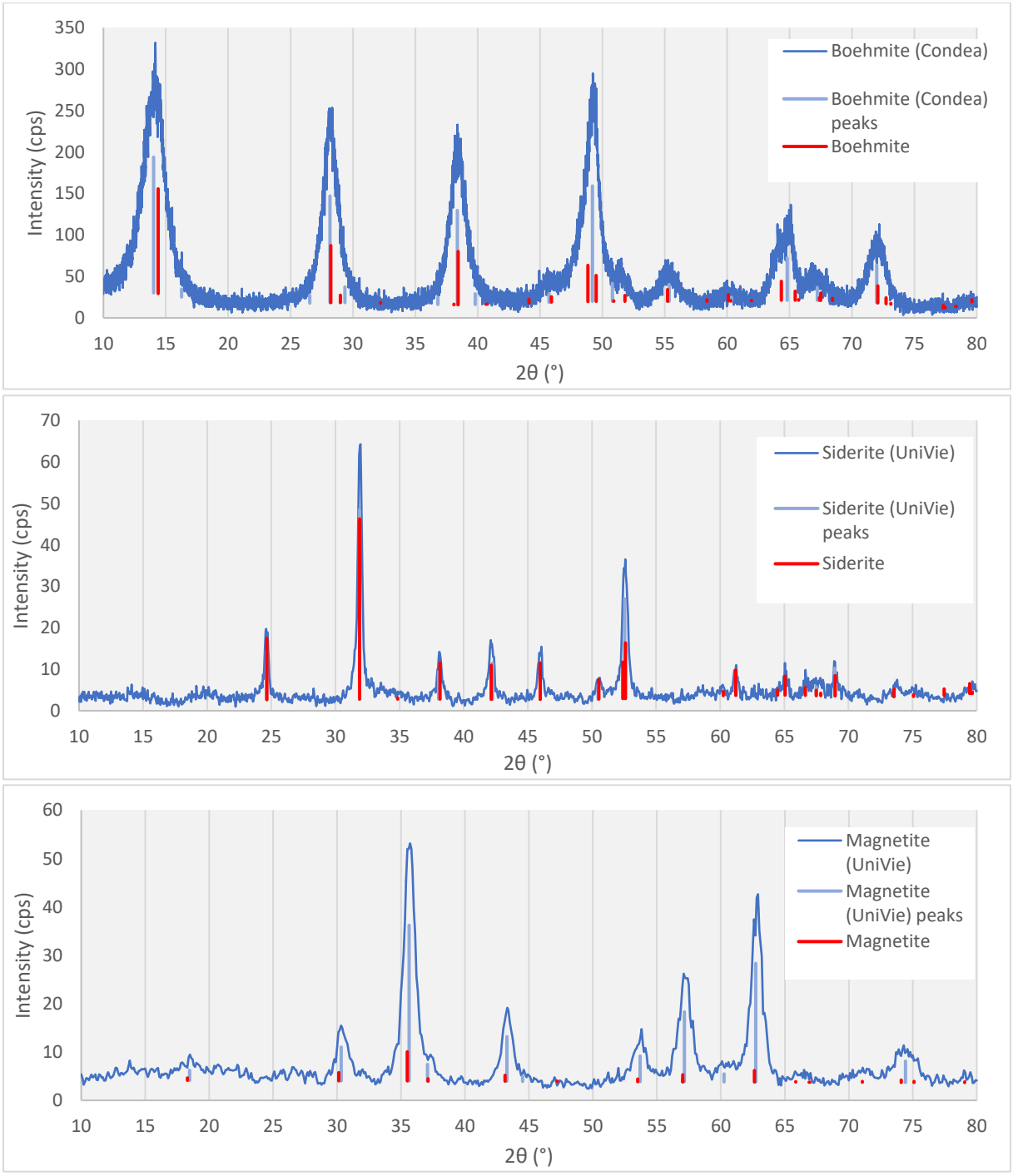

Figure 6: XRD results for the Al_2O_3-, the siderite and the magnetite analysis. The pattern of each mineral powder is compared to the theoretical peaks from COD database ().

3.2 Sorption experiments

3.2.1 Hg concentration analysis

Figure 7 shows the Hg concentration measurement results of the sorption pre-experiments, and the corresponding data can be found in *table B1.*

The results of the sorption experiments suggest that most of the sorption process takes place in the first few minutes after the addition of Hg to the system. The experiments display how the sorption capacity is increased through the increase of Al_2O_3-surface area. In experiments with 360 m^2/l (SorpG, SorpH) an average of 72 %, with 900 m^2/l (SorpI, SorpJ) an average of 82 % and with 2700 m^2/l (SorpK, SorpL) an average of 93 % of the added Hg is adsorbed after 4 hours, respectively.

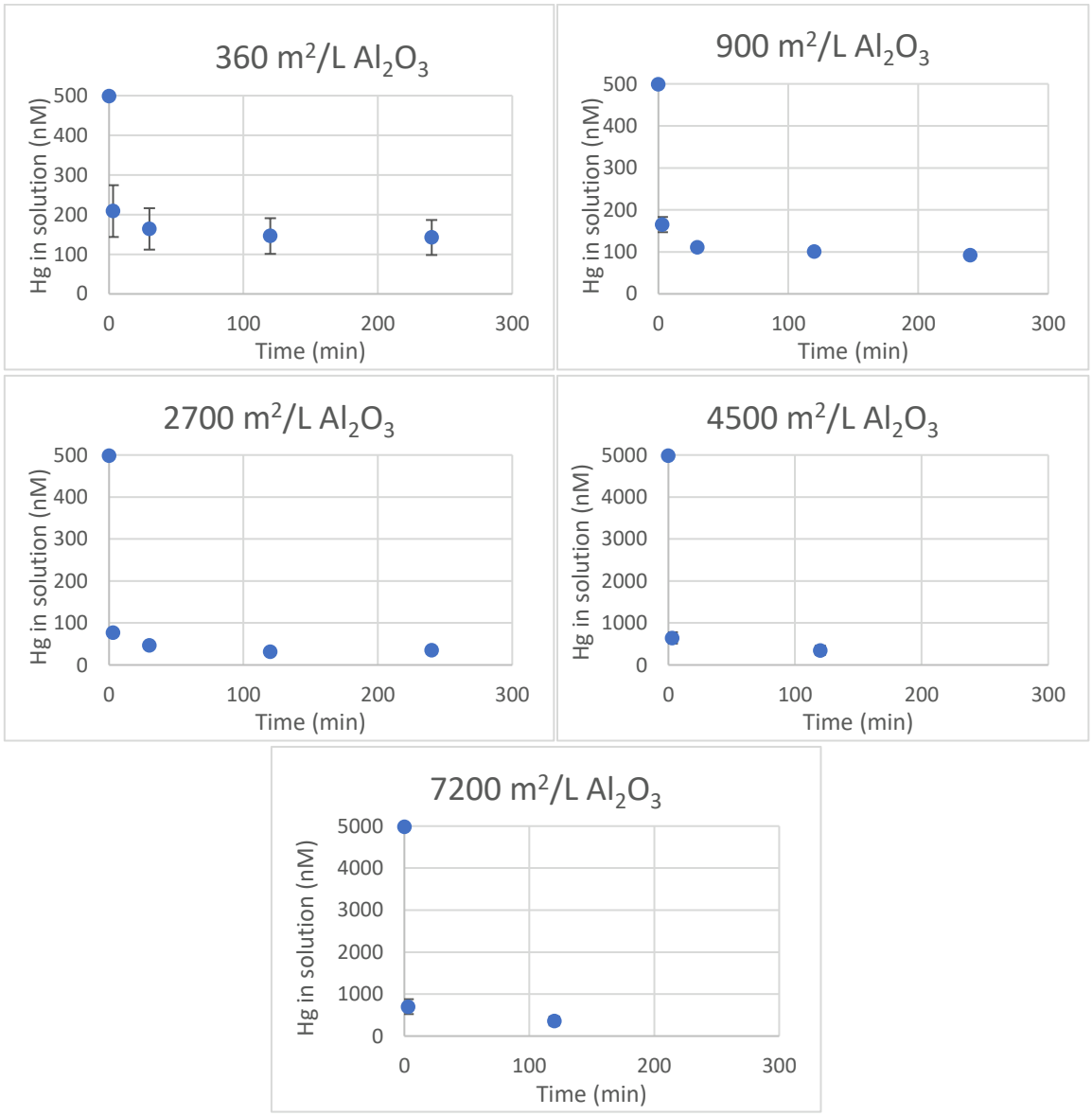

Figure 7: These graphs show the Hg concentration in solution at different time points of the sorption experiments. Each experiment was done with the same settings except for the for the Al_2O_3-surface area. The mean concentration values of the duplicates are depicted here as blue dots, with the standard deviation mostly hidden under the dots (n = 2).

Experiments SorpM- SorpP were executed later and therefore based on the knowledge gained from experiments SorpG- SorpL and previously conducted heterogeneous reduction experiments. The starting Hg concentration was elevated from 500 to 5000 nM in respect to the decreased reaction kinetics evoked by the addition of the Al_2O_3-surface. In experiments M and N, the surface area was elevated to 4500 m^2/l, resulting in 93 % sorption efficiency on average after 2 hours. In SorpO and SorpP (7200 m^2/l Al_2O_3) slightly more Hg was still in solution after two hours.

3.2.2 Plate reader iron analysis

In *Figure 8* the iron concentration results from the plate reader analysis are depicted. The first sample was taken three minutes after $FeCl_2$ (62.5 µM) was added to the system. For some reason, an initial Fe concentration increase can be observed in experiments SorpA and SorpB (75.3 µM). It may be due to insufficient mixing in solution, but the high resemblance of the duplicates speaks against this explanation. Nevertheless, as in the Hg concentration results of the sorption experiments, a clear connection between the higher Al_2O_3-area and the sorption efficiency can be drawn. Again, a major part of the sorption process takes place in the first few minutes after the addition of iron to the system.
Based on the results of experiments SorpA- SorpF, the Al_2O_3-content for SorpQ- SorpT were evaluated. On the basis of *Figure 8,* the calculation and thought process can be explained: In this graph, the iron concentrations of the sorption experiments two hours after initiation are depicted in reference to the associated Al_2O_3-content. The three dots in the lefthand side illustrate experiments SorpA-SorpF (duplicates are represented as one dot). These three experiments suggest a linear connection between the Al_2O_3-surface area and the adsorption efficiency. A first set of experiments was conducted with the premise that this linear trend continues until all the iron is sorbed to the γ-Alumina particles, so the intersection of the linear in *Figure 9* and the x-axis was calculated (about 4500 m^2/l). This surface area was used in experiments SorpQ and SorpR. In case the linear relationship was not valid when approaching total Fe-sorption, a second set of duplicate experiment (SorpS and SorpT) with 7200 m^2/l Al_2O_3-surface area was conducted.
The results show that after 2 hours with 4500 m^2/l, 93 % of the added Fe is adsorbed to the Al_2O_3-particles. Enhancing the surface area to 7200 m^2/l, increases the sorption efficiency by only 0.5 %.

3.2.3 Hg isotope analysis

Sorption experiments SorpM, SorpN, SorpO and SorpP were analyzed for Hg isotopic composition (*Table 11* in appendix). Based on the knowledge gained from the Hg concentration analysis of the sorption experiments, *Figure 10* and *Figure 11* were created to understand MDF and MIF of the sorption process to γ-Alumina. The four analyzed sorption experiments varied in the sorption efficiency three minutes after introducing Hg to the system (timestep 0 fil – the samples taken with a 0.2 µm filter on the syringe, thus only holding Hg of the solution phase). Only these samples from the first timestep were used for the MDF and MIF calculation, since they were least likely to have suffered from Hg isotope exchange between the sorbed fraction and the fraction in solution.

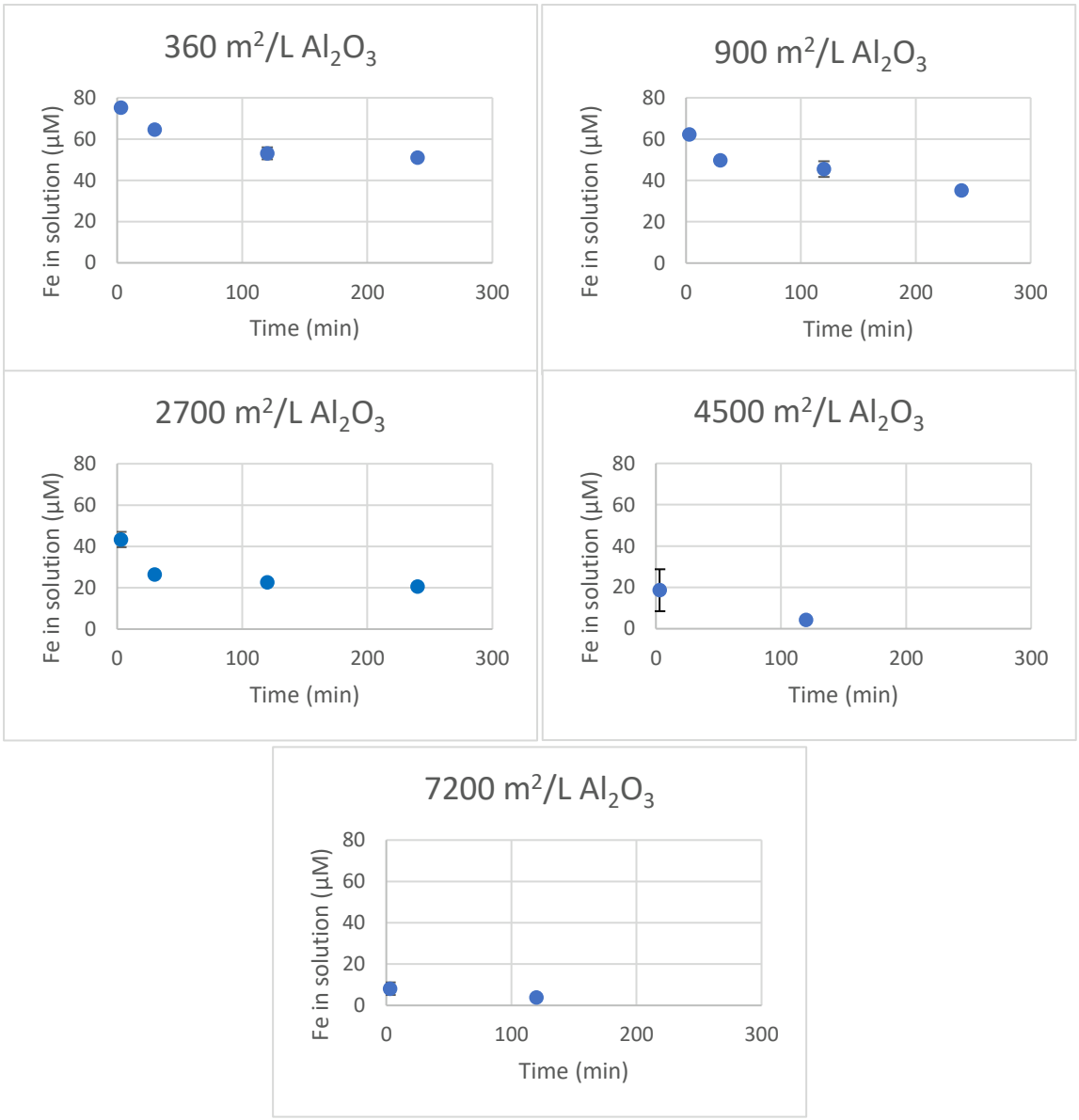

Figure 8: These graphs show the iron concentration in solution at different time points of the sorption experiments. Each experiment was done with the same settings except for the for the Al_2O_3-surface area. The mean concentration values of the duplicates are depicted here as blue dots, with the standard deviation mostly hidden under the dots (n = 2).

Figure 10 pictures the δ^{202}Hg on the y-axis and the fraction remaining (f-value) on the x-axis, as in a Rayleigh fractionation plot. "Fraction remaining" in this case represents the Hg portion still in solution, while the rest has already sorbed to the γ-Alumina particles. This f-value was calculated with the Hg concentration measurement results. Since the sorbed fraction differs in each reaction bottle (either due to different γ-Alumina surface area or because of slight deviations in the duplicates), the four data points vary in their f-value. A fifth data point was added to the data set with δ^{202}Hg = 0 and fraction remaining f = 1, to represent the isotopic composition of the used NIST-3133 Hg standard prior to the sorption process. A logarithmical fit with the curve shape y = -0.189ln(x) - 0.0111 and R^2 = 0.932 and a linear fit with a slope of -0.4246 and R^2 = 0.8614 were then added. The graph indicates that the sorption process favors light isotopes, since the solution pool gets heavier with decreasing fraction remaining value.

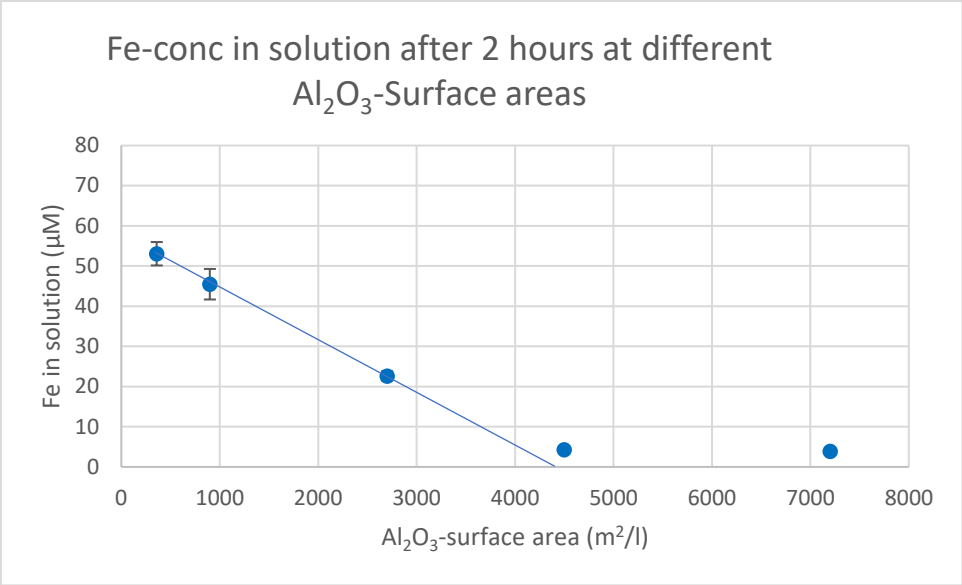

Figure 9: This plot summarizes the iron concentration analysis of the sorption experiments two hours after adding the $FeCl_2$-solution to the system. The iron solution (y-Axis) is not set in relation to the sorption time, but to the γ-Alumina surface area (x-axis).

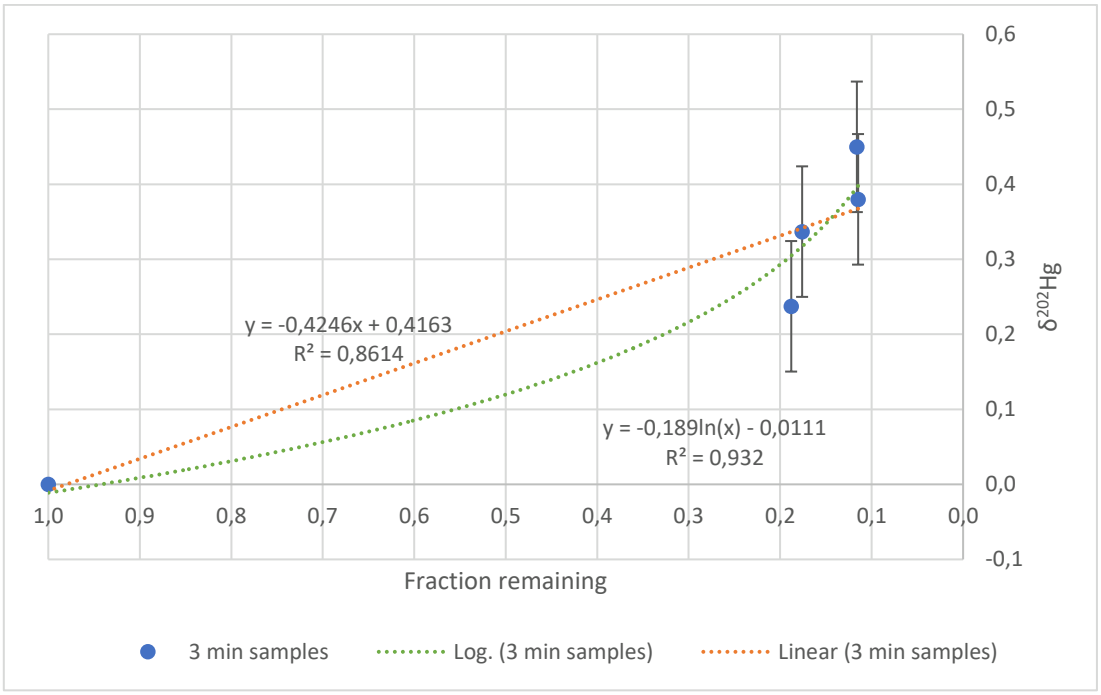

Figure 10: MDF Rayleigh Fractionation plot based on the sorption experiments SorpM, SorpN, SorpO, and SorpP using only the earliest taken filtered samples (three minutes after addition of Hg to the system). "Fraction remaining"- f-value is depicted on the x-axis and shows the relative Hg fraction that is still in solution and not sorbed to the γ-Alumina surface. The y-axis shows the δ^{202}Hg-signature of the samples.

In *Figure 11* the same principle as described above was applied to the Δ^{199}Hg of the same four samples, to study the influence of the sorption process on MIF of the Hg isotopes. The logarithmical trend line describing these data set offers a flatter curve shape y = -0.035ln(x) – 0.0003 and R^2 = 0.8063 and the linear trend line shows a slope of -0.0795 and R^2 = 0.7788.

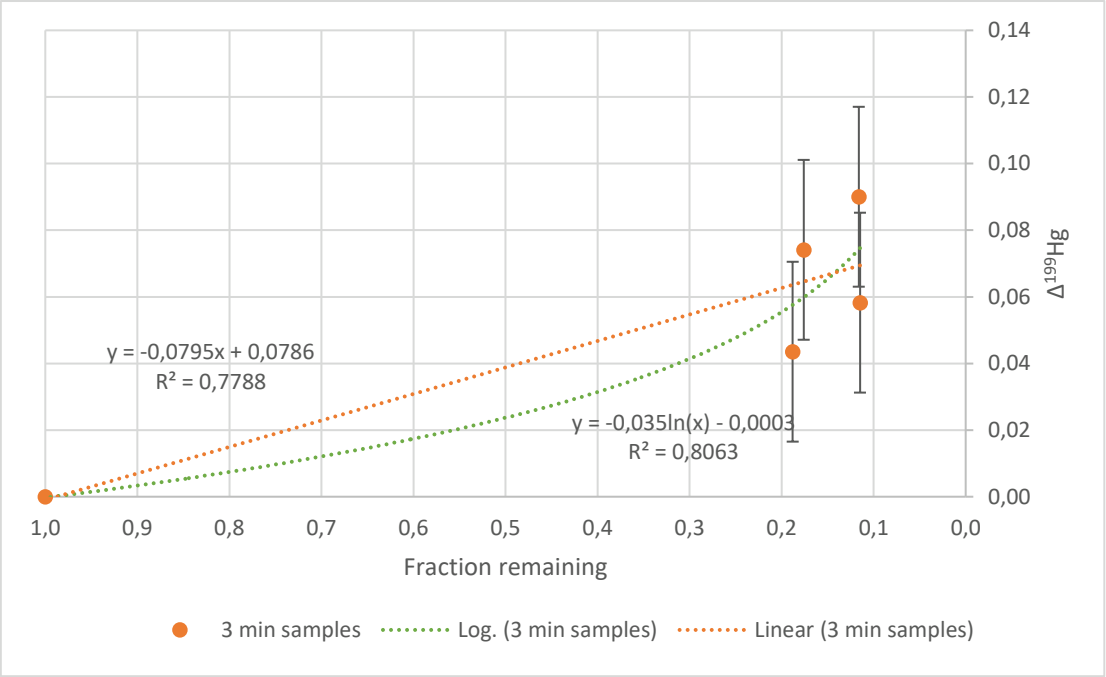

Figure 11: MIF Rayleigh Fractionation plot based on the sorption experiments SorpM, SorpN, SorpO, and SorpP using only the earliest taken filtered samples (three minutes after addition of Hg to the system). "Fraction remaining"- f-value is depicted on the x-axis and shows the relative Hg fraction that is still in solution and not sorbed to the γ-Alumina surface. The y-axis shows the Δ^{199}Hg-signature of the samples.

3.3 Homogeneous reduction experiments

3.3.1 Fe- and Hg-speciation modelling

Hg-speciation comparison with different NaCl concentrations

The three models in *Figure 12* all show the change in Hg speciation with changing pH-value ranging from 1 to 14. In all three plots the same input concentrations were established ([Hg] = 0.5 µM and [Fe(II)] = 12.5 µM) except for the NaCl-concentration, which varied from 34.2 µM (a) to 342 µM (b) and 3240 µM (c). NaCl concentration of 324 µM was commonly used in the experiment, so *Figure 12* gives a comparison between the speciation resulting from this concentration, a tenth of it and multiplied by ten. Note that in reality a decent amount of Cl^- is also coming from the addition of Fe(II)Cl_2-stock solution, which is not considered in the modelled plots. The exact amount of Cl^- put into the system that way cannot be calculated, but it is at least double the amount of Fe(II).

Studying plot 12b in detail from left to right (with increasing pH), a first dramatic change of the Hg-speciation can be seen at pH 4. The predominant species $HgCl_2$ drops and HgClOH increases. At about pH 5 $Hg(OH)_2$ starts being present and increases drastically resulting in being the only relevant species at about pH 9. HgClOH reaches a maximum at pH 5.9 and $HgCl_2$ becomes irrelevant at pH 7.

The three graphs show that a lower NaCl-concentration shifts the first dramatic change of the Hg-speciation to the left compared to panels 12b and 12c, resulting in a drop of $HgCl_2$ at about pH 3 (in plot 12b, this drop can be observed at about pH 4 and in plot 12c at about pH 6). In all three cases, the general image of the speciation looks quite similar, but shifted to the right

with increasing NaCl-concentration. With increasing NaCl-concentrations, the $HgCl^{-1}$ species becomes more prominent at low pH-values.
At pH 8, which was prevalently used in the experiments of this thesis, a dramatic difference in $Hg(OH)_2$ concentration between the three plots can be noticed. Especially by increasing the NaCl-content, the steep slope of the $Hg(OH)_2$ species surrounds the vertical pH 8 line, leading to dramatic changes of the Hg-species that was reported to be the relevant Hg-species determining the kinetics of the reduction of Hg(II) by Fe(II).

Fe-speciation

Figure 13 shows a pH sweep of the predominant Fe-species along the pH range from 1 to 14 following an input of [Fe(II)] = 12.5 µM, [Hg] = 0.5 µM and [NaCl] = 342 µM. Between pH 1 and pH 7 the only predominant Fe(II)-species in solution is Fe(II). The reactive species $FeOH^+$ then becomes present, faces a maximum at about pH 10.5 with a concentration slightly above 9 nM, drops again and vanishes at about pH 12. At about pH 10 $Fe(OH)_3^+$ becomes present and at about pH 12 it becomes the only mentionable species.
At pH 8, the $FeOH^+$-concentration is quite low with only 0.36 µM, compared to the total Fe(II) concentration of 12.5 µM. Since this pH-value is at a slope and not a plateau of this reactive species, pH changes result in drastic $FeOH^+$-concentration changes.
Figure 14 mimics the concentration losses of Hg, total Fe, Fe(II) and $FeOH^+$ during the course of an experiment assuming the reaction reaches 100 % completion (meaning all the Hg(II) in solution has been reduced to Hg(0) and vaporized). For each reduced mol of Hg, 2 mol of Fe(II) are oxidized, leading to a drop from 12.5 µM starting concentration total Fe(II) to 11.5 µM when reducing 0.5 µmol Hg ([NaCl] = 324 µM, pH = 8). So, 1 µmol Fe(II) is needed to reduce all the Hg.
The $FeOH^+$-species, which is assumed to be most reactive and therefore crucial for the reaction kinetics only reaches a concentration of 0.36 µM at the beginning of the reaction. However, at the end of the reaction, when 0 µM Hg are in solution, $FeOH^+$ still shows a concentration of 0.33 µM, due to constant equilibration between the Fe(II)-species as the reaction progresses. This results in a $FeOH^+$ concentration loss of 7 % while the Hg concentration decreases by 100 %.

3.3.2 Hg Concentration Analysis

The data resulting from the DMA-80L analysis was used to check the mass balance of the conducted experiments. In an ideal system, the overall Hg mass in the reactor, the traps and the sample volumes should be the same as the Hg mass spiked in at the beginning of the experiment.
The data is presented in x-y-diagrams with the Hg mass on the y-axis in nmol and the time of sampling after experiment start on the x-axis in min. In both the reactors and the traps, the content of Hg in the sample volumes was added.
Furthermore, the data was used to calculate the *f*-value for each sample.

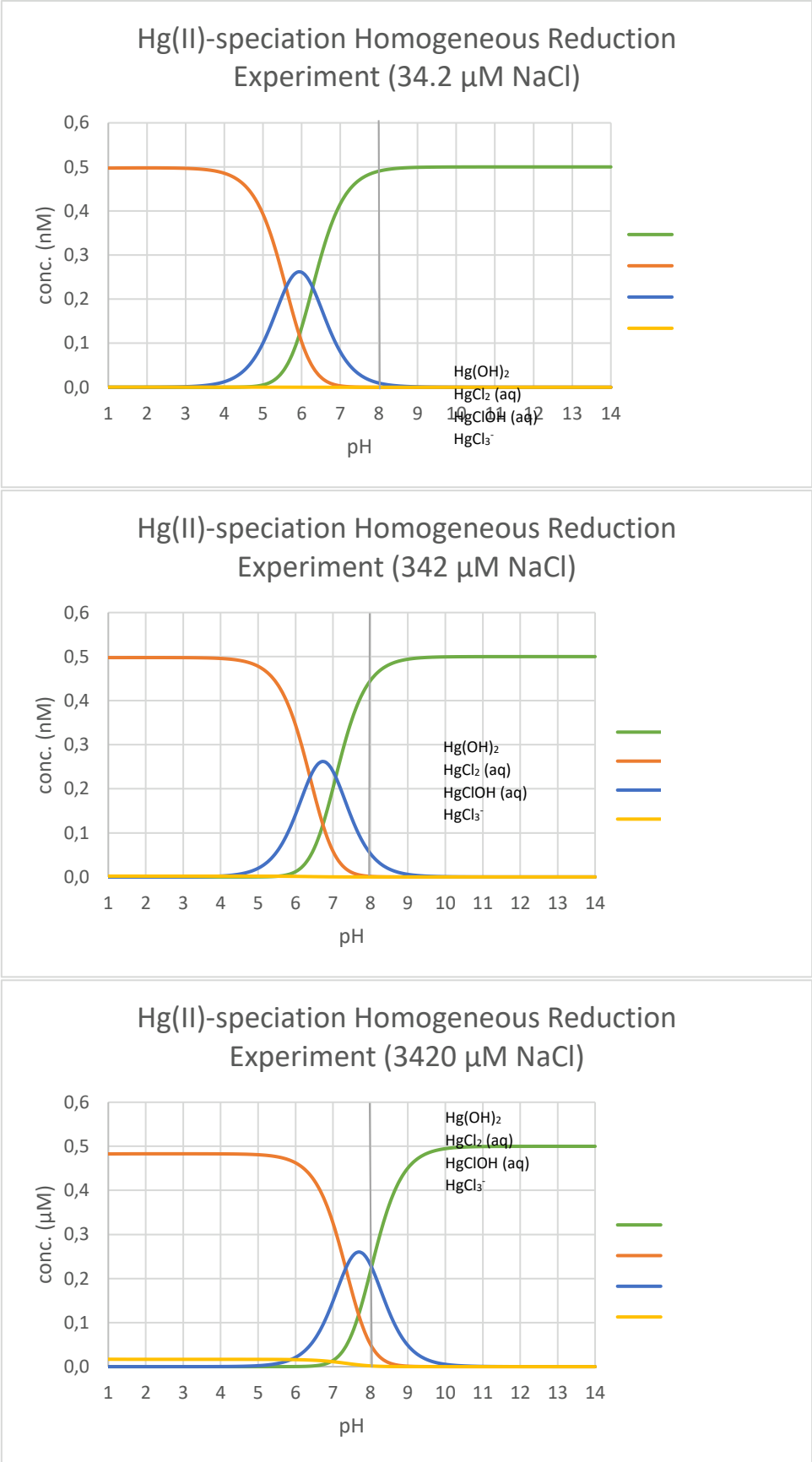

Figure 12: Visual MinteQ model with starting concentrations of the homogeneous reduction experiments presented in the results section. NaCl was changed (34.2 µM, 342 µM and 3420 µM) to display its effect on the Hg-speciation. pH-value is depicted on the x-axis and the concentration of the according species on the y-axis.

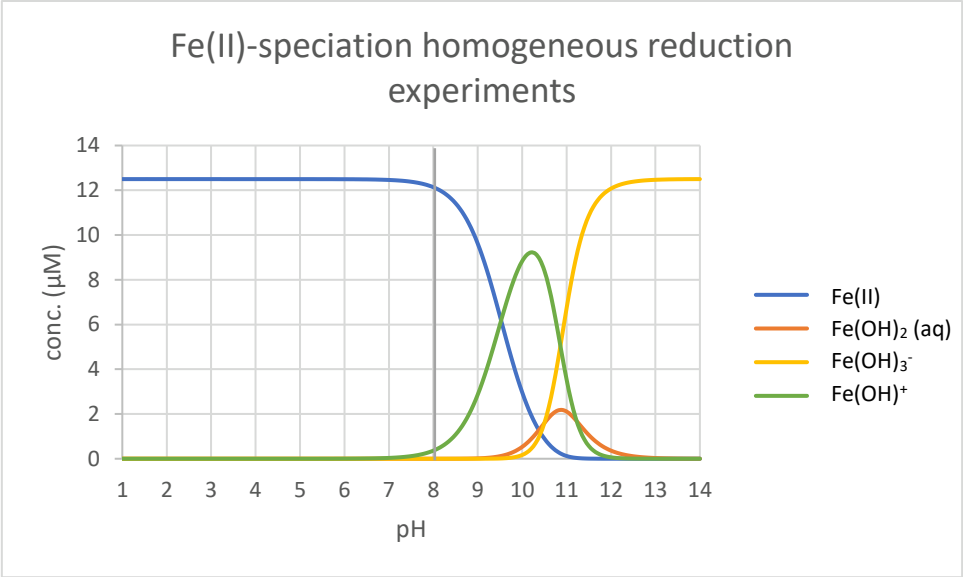

Figure 13: Visual MinteQ model with starting concentrations of the homogeneous reduction experiments presented in the results section. pH-value is depicted on the x-axis and the concentration of the according species on the y-axis. This plot shows the Fe-speciation with these settings. The grey vertical line represents the pH-value the experiments were conducted at (pH = 8).

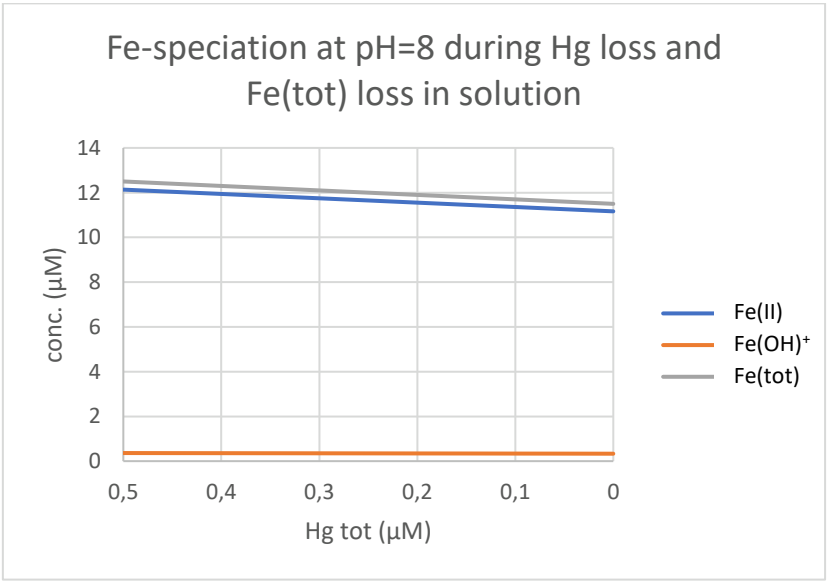

Figure 14: Visual MinteQ model mimicking the Hg loss from starting concentration ([Hg] = 0.5 µM, lefthand side of the plot) to a complete reduction of all the Hg ([Hg] = 0 µM, right-hand side of the plot). The plot was created by running Visual MinteQ at in 6 iterations from [Hg] = 0.5 µM with step size 0.1 µM and corresponding total Fe(II) loss (Hg concentration loss times two, since two Fe(II) are oxidised when one Hg(II) is reduced to Hg(0)).

In the homogeneous reduction experiments, the trap liquids (10 ml) were exchanged at each sampling step. The analyzed data gathered that way represents a mixture of the instantaneous and the cumulative products. To be more specific, it shows the isotopic signature of the

cumulative products between the previous and the next sampling step. The cumulative products were calculated and displayed in the isotope data plots.

Figure 15 shows the results of the Hg concentration analysis of the homogeneous experiments HomN and HomR not as concentration values, but as mols in reactor, traps and combined at each time step, to visualize the Hg loss in the reactor, the increase in the traps and the recovery efficiency of the system irrespective of the reactor and trap volume (*Table* in appendix). These experiments were the only ones from the homogeneous experimental runs, that were considered robust enough to proceed with meaningful isotope measurements (in terms of both recovery and progression of the reduction by the end of the experiments).

Both these experiments show a Hg-decrease in the reactor bottles (blue dots) and an accumulation of Hg in the trap vessels (orange dots), as expected. At time 0, HomN and HomR both show slight deviations from the theoretical 50 nmol spiked into the system (HomN: 45.57 nmol, HomR: 46.64 nmol). In HomN the last sampling point was taken after 240 min. At this point in time, the Hg content in the reactor dropped to 8.83 nmol in the reactor and the traps had captured 29.42 nmol, indicating a mass balance loss of 19.9 % over the time span of the reaction. HomR depicts a similar cumulative trap Hg content (29.43 nmol), but less significant loss in the reactor (16.19 nmol), resulting in a more consistent mass balance with a deficit of 2.61 %, which is within analytical uncertainty of the DMA-80L.

Determination of the Hg Reduction Rate Constant

An average data plot with the Hg concentration data measured of the reactor samples of the homogeneous reduction experiments HomN, HomQ, HomR and HomS was created to get a deeper understanding of the reaction kinetics (*Figure 16*). Experiments HomQ and HomS could not be used for isotope data since Hg losses along the way from the reactors to the traps could be observed in the Hg concentration analysis causing incomplete recoveries. However, the results of the Hg concentration analysis of the reactor samples were still robust and therefore useful for investigations on the reaction kinetics. Based on this data set, a plot representing the average Hg concentration loss in the reactor, the concentration increase in the traps of each experiment, a modelled rate constant (*Figure 16*) and first and second order linearization fits (*Figure 17*) were calculated. *Amirbahman et al., 2013* postulated second order reaction kinetics depending on the concentrations of the most reactive species $FeOH^+$ and $Hg(OH)_2$ after studying the reduction of Hg(II) by Fe(II) in solution. The purpose of the investigation concerning reaction kinetics in this study is to compare the results with previous works and eventually form assumptions in this regard.

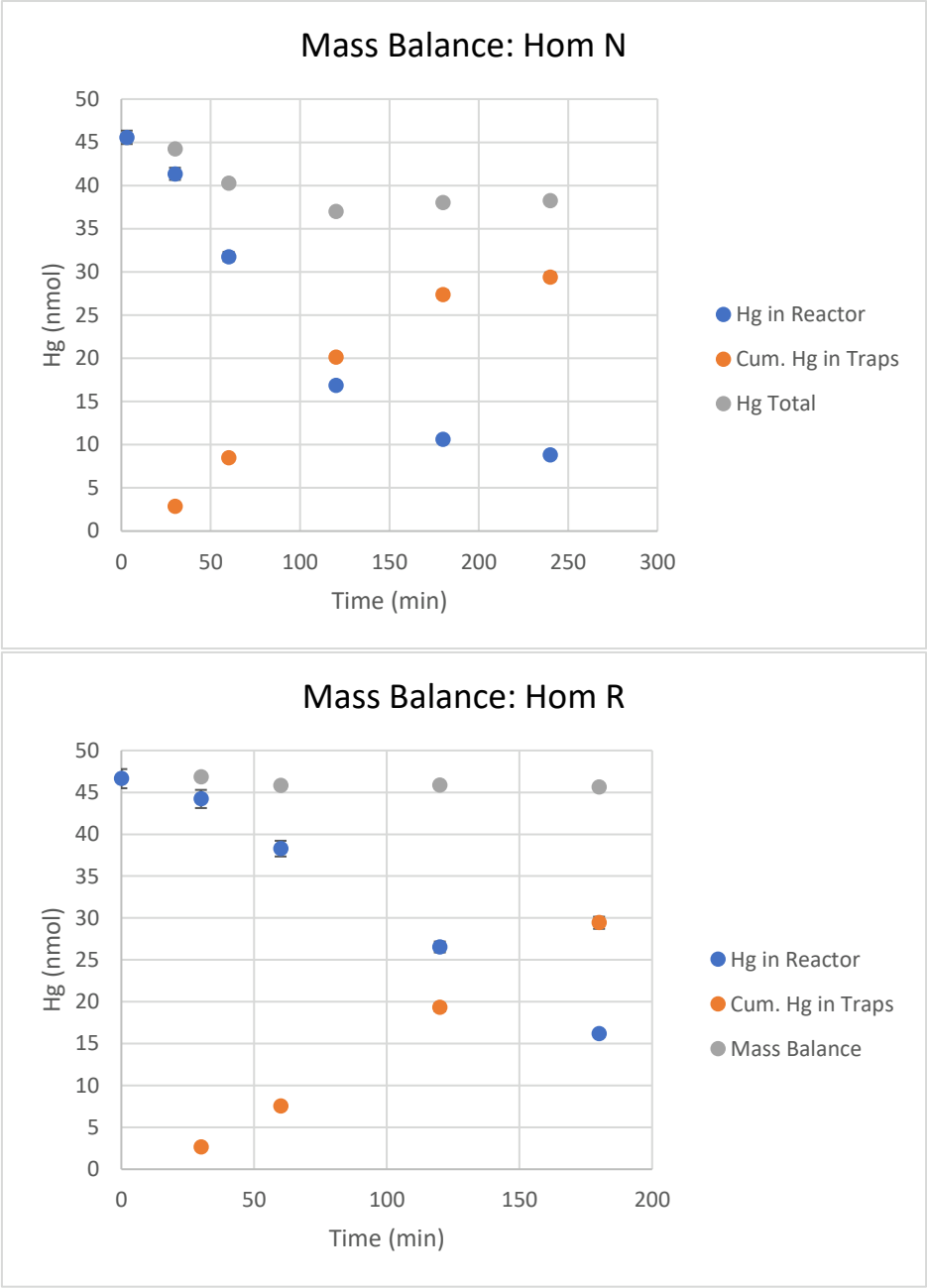

Figure 15: These plots show the mass balance of the homogeneous reduction experiments HomN and HomR. It depicts the total amount of Hg (y-axis) at different times of the experiment period (x-axis). The two different fractions are the trap values (orange dots) and the reactor values (blue dots). The data also includes the fraction in the sample volumes. The grey dots display the combined masses of the trap and the reactor fractions.

Based on the total measured Hg concentration in the reactor, the reactive species $[Hg(OH)_2]$ and $FeOH^+$ concentration were modelled in vMinteQ, similar to *Figure 14.* The Hg concentration of each time step and a corresponding $Fe(II)_{tot}$ drop of 2 mol $[Fe(II)_{tot}]$ for the loss of each mol Hg(II) were assumed to model $Hg(OH)_2$ and $FeOH^+$ concentrations. Based on these two values, a reaction rate was calculated to be $k = -2.04*10^4\ M^{-1}\ min^{-1}$ using the solver-function of excel minimizing the summed squared residuals of the average reactor values. The trap values were not taken into account for the calculation of the rate constant. In *Figure 16* the calculated rate constant is shown both for the Hg concentration loss in the reactor and

the elevation in the traps since all the Hg(II) reduced during the process is captured in the traps ideally. Comparing them with the theoretical increase of Hg in the traps, the measured values show a deficit during the course of the experiment, which strongly correlates with the mass loss of each experiment.

This data set was then linearized following (a) the first order and (b) the second order linearization rules (*Brezonik, 2015*). As established above, two methods were applied for the calculation of the rate constant. For the first order linearization, a rate constant of $k = 6.37 * 10^{-3}$ min^{-1} (standard deviation $\sigma = 3.64 * 10^{-4}$) was calculated with the mean value of the difference of the Hg starting concentration and the values of each sampling point. $k = 6.26 * 10^{-3}$ min^{-1} with a variance of $R^2 = 0.99$ was estimated with the graphical solution (trend line through the linearized mean concentration values). The second order linearization resulted in rate constants $k = 7.11 * 10^4$ M^{-1} min^{-1} (standard deviation $\sigma = 4.81 * 10^3$) and the graphical solution resulting in $k = 7.28 * 10^4$ M^{-1} min^{-1} (variance R = 0.99), respectively. The linearization results are depicted in *Figure 17.*

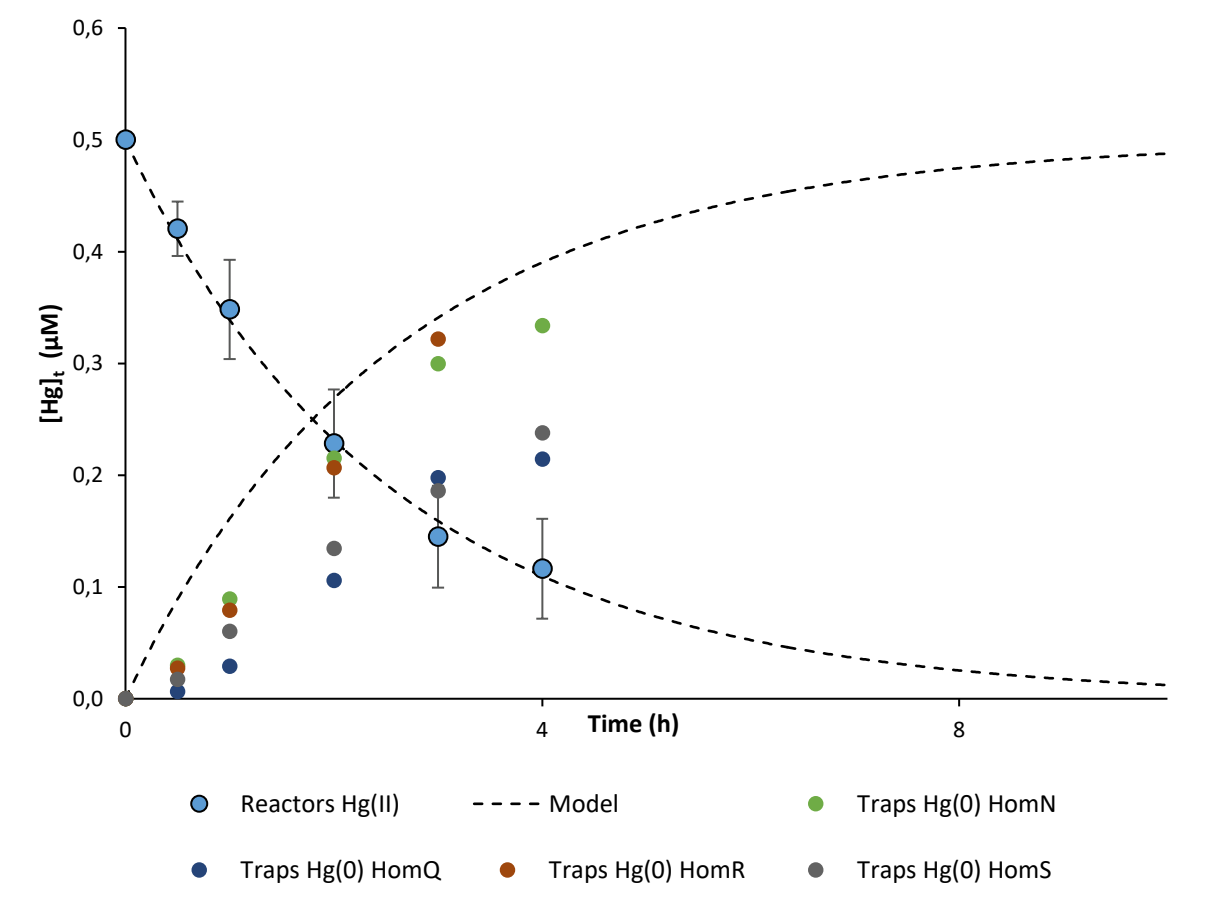

Figure 16: Homogeneous reaction: Hg concentration loss in reactor (average): This plot shows an average concentration loss in the reactor bottle during the homogeneous Hg reduction experiments HomN, HomQ, HomR and HomS. The dot at time 0 is not an average of the measured values at experiment start, but the known value spiked in. n = 4, except for the last dot n = 3. An exponential trend line was fitted to the data set. All the experiments were conducted with the same starting concentrations, pH = 8, [Hg] = 498.5 nM, [Fe] = 12.5 µM, [NaCl] = 342.2 µM.

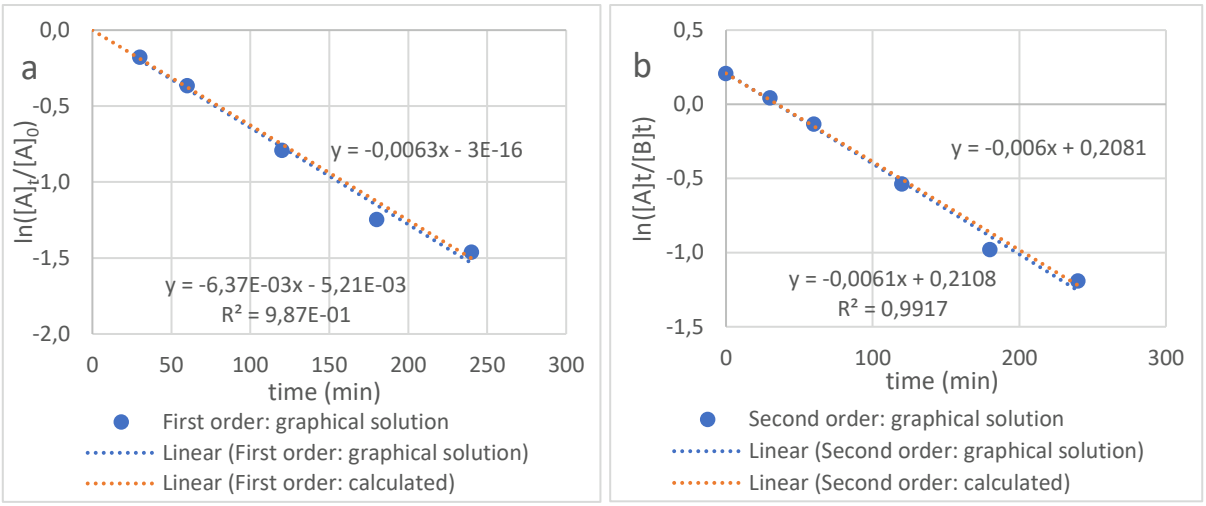

Figure 17: Comparison between the First order (a) and second order (b) approach to the homogeneous reduction kinetics between Fe(II) and Hg(II) in solution. The calculations are based on the experiments HomN, HomQ, HomR and HomS.

3.3.3 Hg Isotope Data

Mass Dependent Fractionation

The isotope data (*Table* in appendix) is displayed in graphs showing the portion of unreacted Hg on the x-axis and the δ^{202}Hg-value of the samples taken during the experiments on the y-axis, like in the Rayleigh fractionation plot described in *Figure 1.*

For each experiment, a linear trend line and a logarithmical trend line was created, to show their R^2- values, respectively. A higher R^2-value of the logarithmical fit suggests kinetically driven experiment conditions, whereas a better linear fit points towards equilibrium conditions.

In addition to the data gathered by sampling reactor and traps during the experiment, mass balance data is shown in the plots. The values of the mass balance at each point along the x-axis were calculated by adding the associated δ^{202}Hg-values of the reactor and traps multiplied by its pool size (*f*-value):

$$\boldsymbol{\delta^{202}Hg_{tot}(f) = \delta^{202}Hg_{reactor}(f) \times f + \delta^{202}Hg_{trap}(f) \times (1 - f)} \qquad \textbf{Equation 17}$$

Ideally, the mass balance stays close to zero at each point since the reference material NIST-3133 was used for the Hg addition in each experiment. Variations in the mass balance suggest mass loss in one of the pools like sorption in the reactor and therefore Hg loss in solution (error in reactor pool), trap solution inefficiency or leakage in the gas line system (error in trap pool). Errors in the mass balance could also result from issues during analysis of Hg isotopes in either the trap or reactor sample. This is however less likely because of the rigorous quality control during the analytical procedure.

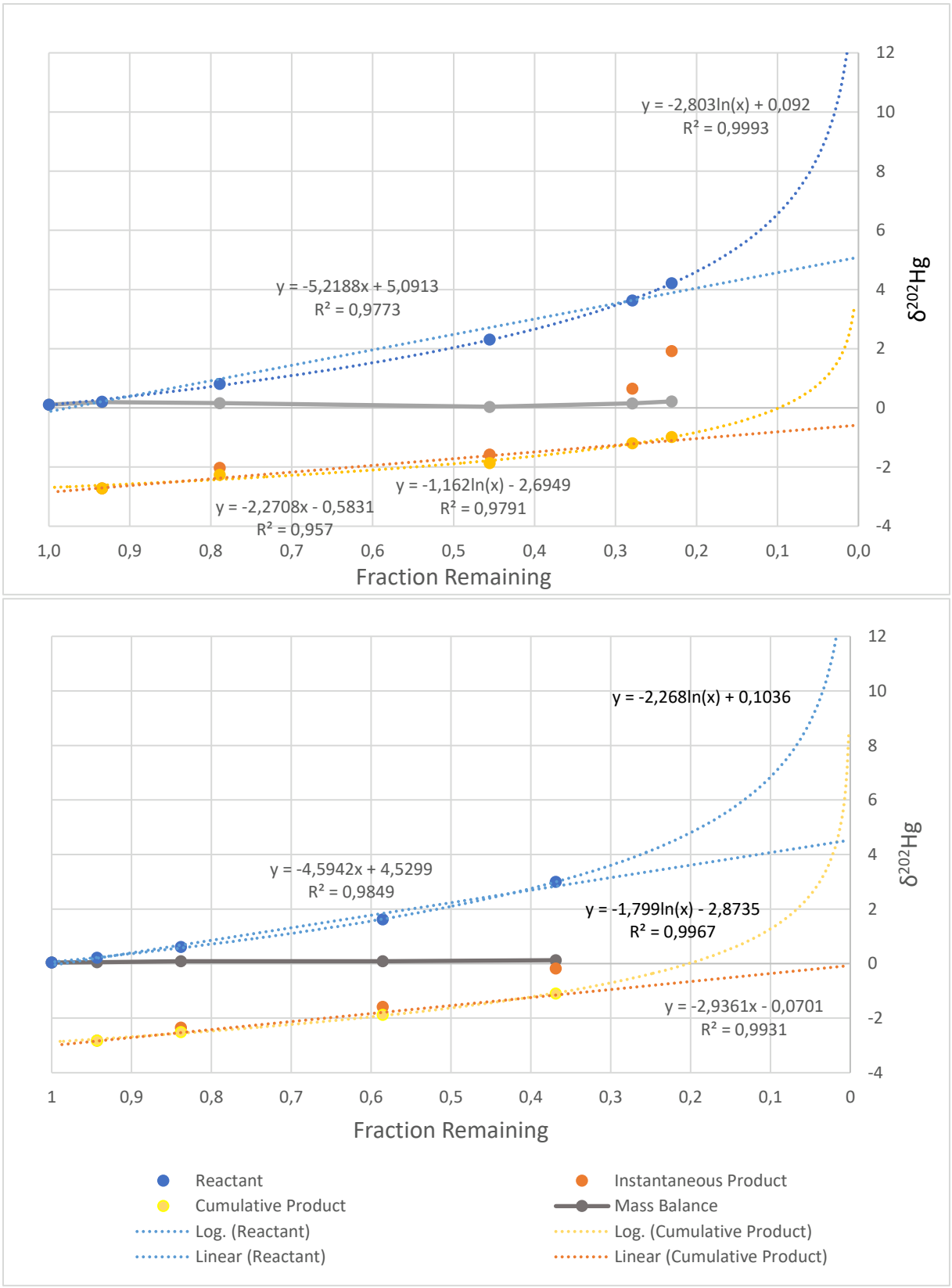

Figure 18: The graphs show the Hg isotope data of the homogeneous experiment HomN and HomR as Rayleigh fractionation plots: On the x-axis, the "fraction remaining"-value f is shown. The y-axis represents the δ^{202}Hg-data measured on the MC-ICP-MS. The mass balance was calculated from the cumulative product values and the reactant values of each measured time step taking the fraction sizes into account. For both data sets, a logarithmical trendline and a linear trendline were fitted.

Figure 18 illustrates the isotope measurement data of the experiments HomN and HomR as Rayleigh fractionation diagrams. In both cases, a similar trend can be observed, exhibiting a loss of preferable lighter isotopes in the reactant pool, resulting in a δ^{202}Hg difference of 4.11 ‰ from the first sampling point at time point 0 and the last one after 240 min for HomN and a δ^{202}Hg difference of 2.96 ‰ over a time span of 180 min for HomR. Consequently, the instantaneous products data is shifted down the y-axis (lower epsilon-values – lighter isotopes) with δ^{202}Hg-differences ranging from 2.30 to 3.89 ‰ in the HomN samples and from 2.94 and 3.20 ‰ in the HomR samples compared to their reactant counterparts. The isotope mass balance slightly drifts apart from the initial isotopic composition in experiment HomN (δ^{202}Hg difference = 0.10 ‰) as well as in HomR (δ^{202}Hg difference = 0.09 ‰) until the end of the observed reaction, in contrast to the Hg concentration mass balance discussed before. Taking into account that the analytical error ranges between 2SD = 0.06 - 0.08 ‰ in both the reactor and the trap samples, the isotopic mass balance of these to experiments can be considered almost perfect, since all the values are within the propagated error.
For both experiments a linear and a logarithmical fit are depicted, to evaluate if equilibrium or kinetically driven reaction conditions were constructed with the experimental set-up. In basically all the data sets of the experiments, the logarithmical fit features a higher R^2-value. In *Figure 19,* the data is presented in another Rayleigh fractionation plot, were all the lines are calculated as described in *Equation 2 – Equation 4.* For HomN, a fractionation factor of ε^{202}Hg = -2.79 ‰ was calculated and for HomR ε^{202}Hg = -2.93 ‰. In both cases, the reactor data set stays closer to its calculated trend line than the product values.

Mass independent fractionation factor E^{199}:

The mass independent fractionation was evaluated using the measured Δ^{199}-data (*Figure 20*). Similar to the mass dependent fractionation, it was plotted as an x-y-diagram, with the f-value on the x-axis and Δ^{199}Hg on the y-axis. Logarithmic trend lines were fitted and the same mathematics as for the calculation of ε were applied. To compare the kinetically driven and the equilibrium condition character of the reaction, logarithmical and linear trend lined were fitted to the Δ^{199}Hg-data as well. Again, the logarithmical fits show higher R^2-values than the linear fits, especially in the reactants data sets.
MIF in the homogeneous reaction shows positive E^{199}-value. The slope of the reactant pool drops during the course of the experiment and the products are shifted up the y-axis, unlike the MDF trend. The Δ^{199}Hg differences are more subtle than observed in the δ^{202}Hg data.
The mass balance stays close to 0 throughout both experiments (deviation up the 0.02 in HomN and 0.02 in HomR). The E-values calculated for the MIF are E^{199} = 0.286 ‰ in HomN and E^{199} = 0.296 ‰ in HomR.

Evaluation of the predominant effect causing Mass Independent Fractionation:

To evaluate the predominant effect causing MIF, a linear York regression following the protocol of *Cantrell, 2008* was calculated in Excel for the data cloud of the Δ^{199}Hg- and the Δ^{201}Hg-values of the experiments HomN and HomR. The slope was compared to the characteristic slopes of MIE (0.9 – 1.3) and NVE (1.6) in *Figure 21.* The York regression calculated this way offers a slope of 1.70 ± 0.12 (Wiederhold, 2015; Zheng & Hintelmann, 2009).

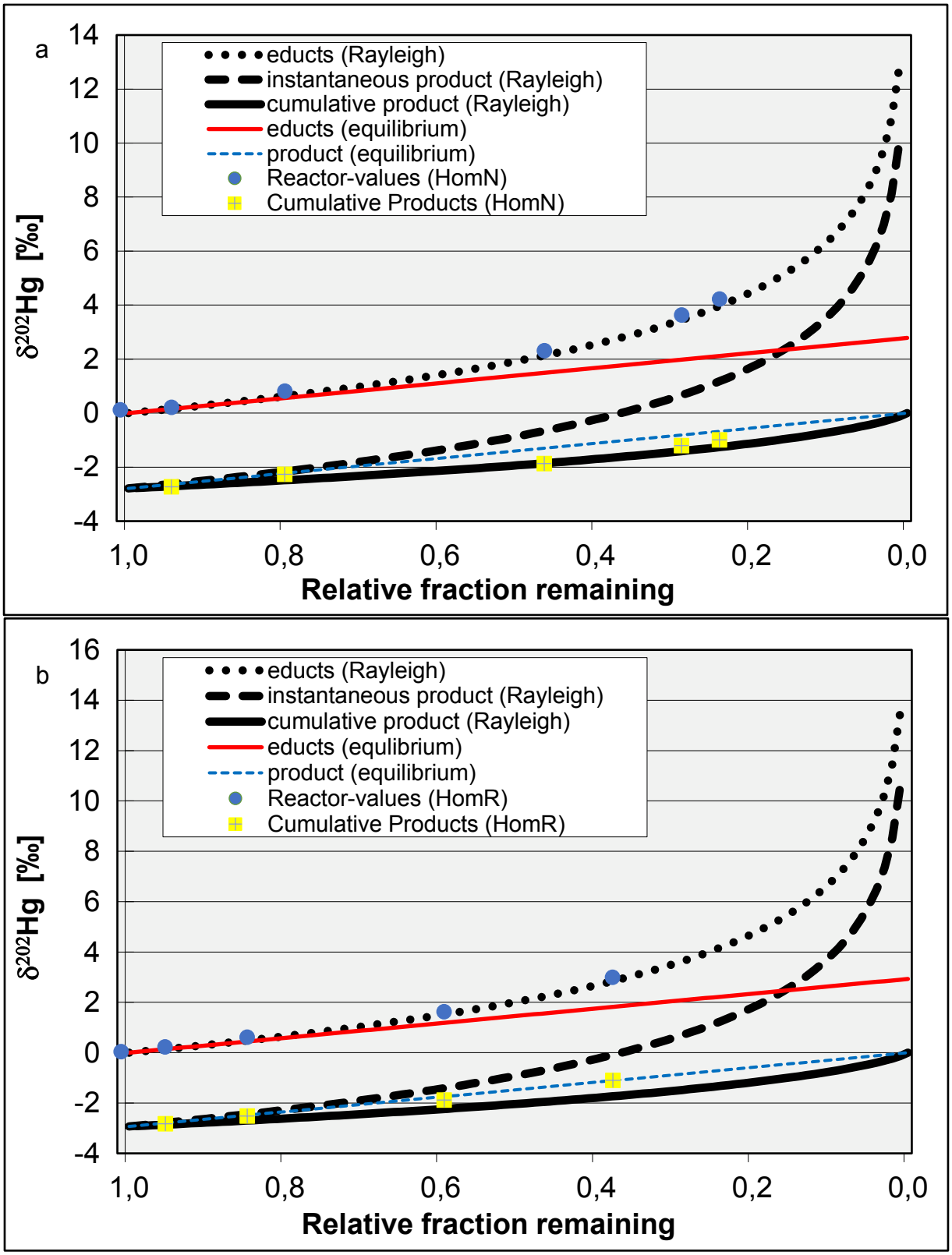

Figure 19: These Rayleigh Fractionation Plots were created to fit the calculated ε-values with the data sets (blue dots: reactant values, yellow squares: trap values) HomN and HomR. The three shown logarithmical trend lines (black dotted line: reactant pool, black dashed line: instantaneous products, black line: cumulative products pool) were all calculated with the *Equation 2-4* and ε being the value calculated as explained above. Equilibrium fits (red line: educt pool, blue dashed line: product pool) were also added with the same ε-value to visualize the kinetically driven and/or equilibrium character of the observed reaction.

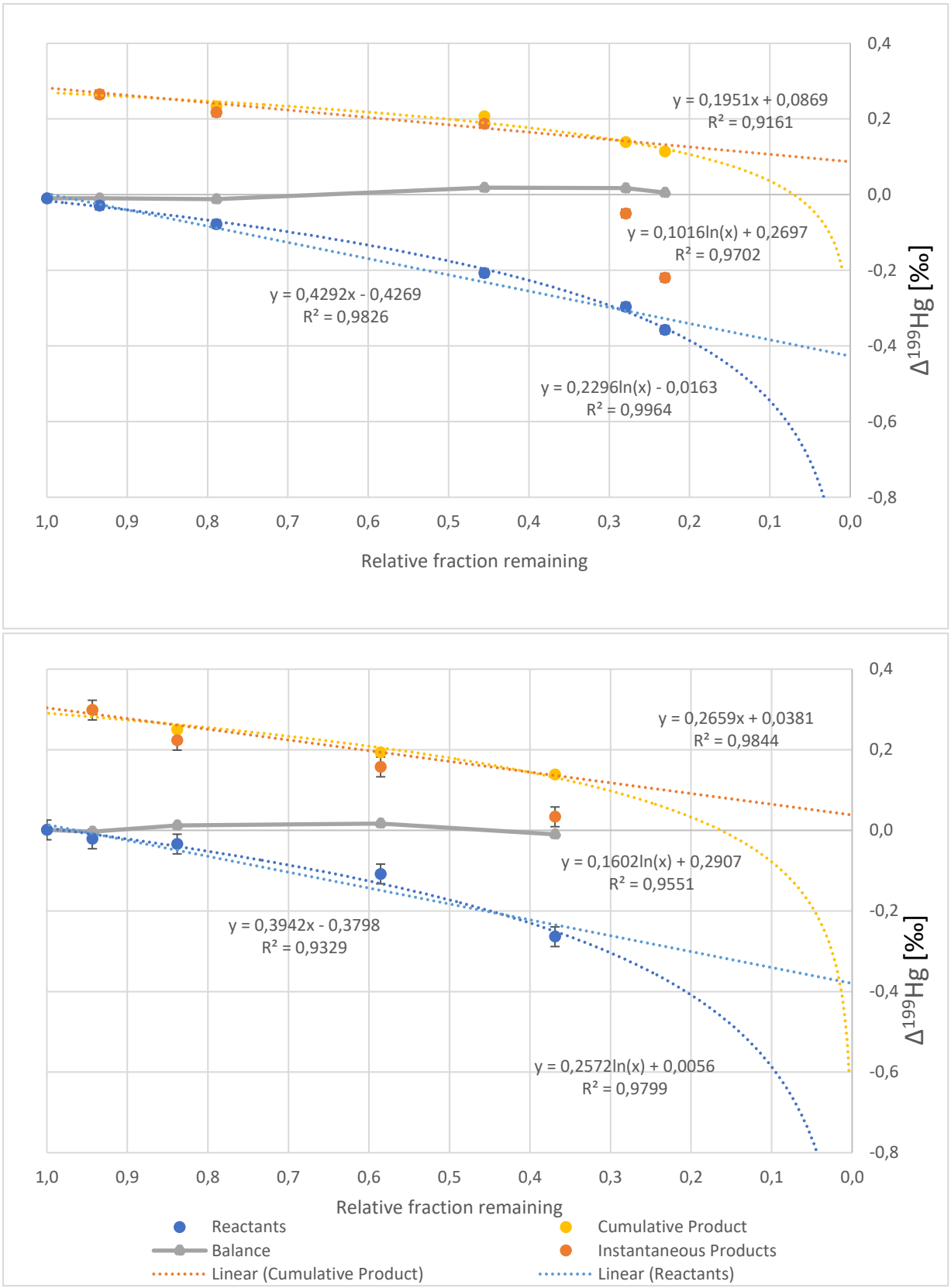

Figure 20: MIF of the experiments HomN and HomR is displayed with the "Fraction remaining"-factor f on the x-axis and Δ^{199}Hg on the y-axis. Logarithmical and linear trend lines were created for the reactant data (blue dots) and the cumulative product data (yellow dots). The measured trap values are represented as orange dots. The mass balance is shown as grey dots at each point sampling.

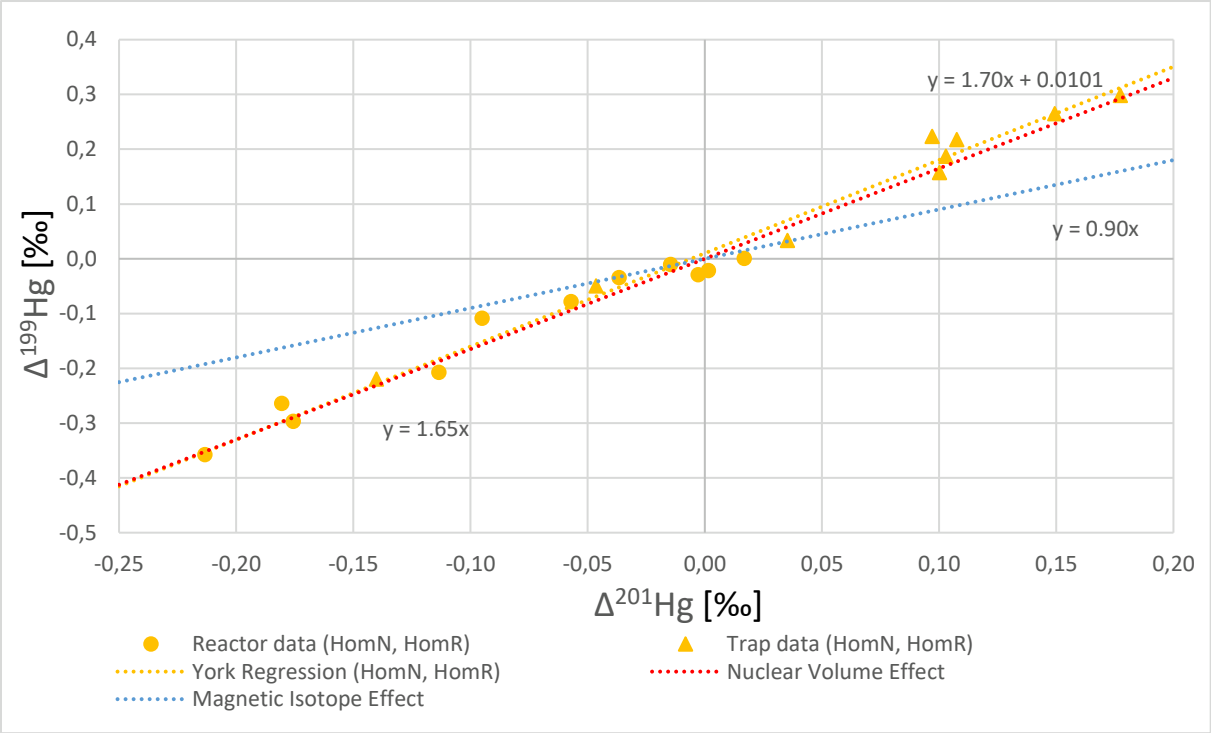

Figure 21: Comparison of the calculated slope York regression line of the homogeneous reduction reaction data gathered in the experiments HomN and HomR in an x-y-plot with Δ^{199}Hg on the y-axis and Δ^{201}Hg on the x-axis. Dotted blue line = MIE slope (0.90), dotted red line = NVE slope (1.65), dotted yellow line = Calculated York regression (slope = 1.70 ± 0.12).

3.4 Heterogeneous Reduction

3.4.1 Hg Concentration Analysis

The results of the Hg concentration measurements of the heterogeneous experiments HetF and HetG are found in the appendix in *Table B3.* For each experiment, there are three sets of data: The samples taken from the reactor without filtering - representing the total Hg in solution and sorbed to the Al_2O_3-particles, the reactor-samples taken with traversing them through a filter (suffix “fil” is written in the sample name) and the samples taken from the trap solutions (suffix ‘T’).

Figure 22: Mass Balances of experiments HetF displays the concentration analysis results of the heterogeneous reduction experiments HetF and HetG. On the x-axis, the time point of sampling after experimental start is represented and, on the y-axis, the total measured Hg-mass in both the trap (orange dots) and the reactor (blue dots) vessels, as well as the associated Hg-mass lost through sampling, are shown. The grey dots show the mass balance, which ideally should stay at the same level – the initial spiked in Hg-mass (1000 nmol) – during the whole experiment. However, compared to the homogeneous experiments, the mass balance is quite far off, especially in the first few sampling points (55 % of the theoretical value measured in the first sample). The reactor measurements for both experiments HetF and HetG do not follow an expected trend, since they start with low Hg concentration values, reach a peak after 60-120 minutes and then start decreasing until the last point of sampling. Nevertheless, the measured trap concentrations exhibit an increase of gathered Hg at each point of measuring, leading the mass balance to be quite off at the beginning, but much less

at the end of the experiments (HetF: Hg loss = 12.7 %, HetG: Hg loss = 12.8 %). At the end of the experiment HetF, 362 nmol Hg were captured in the trap and in HetG, 351 nmol.

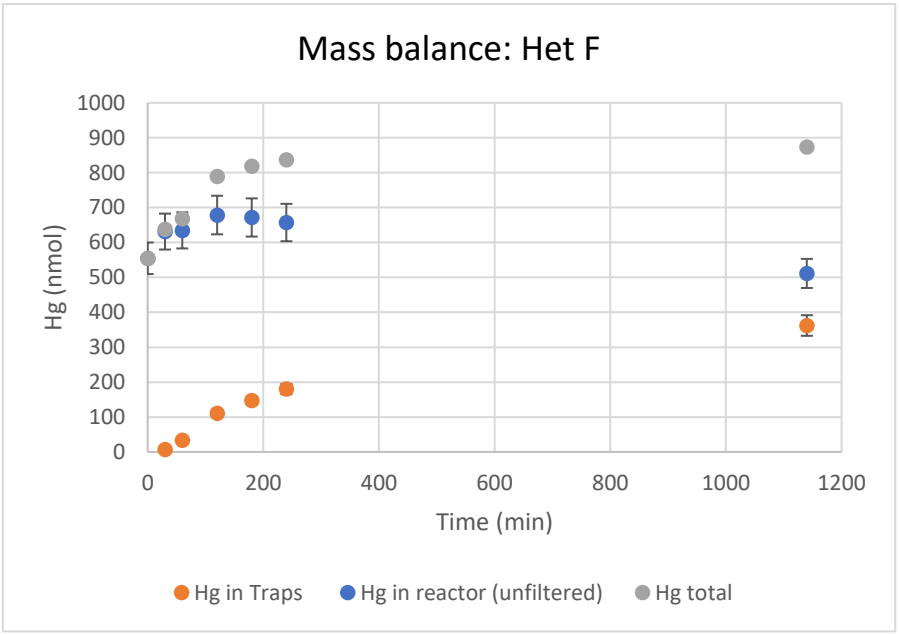

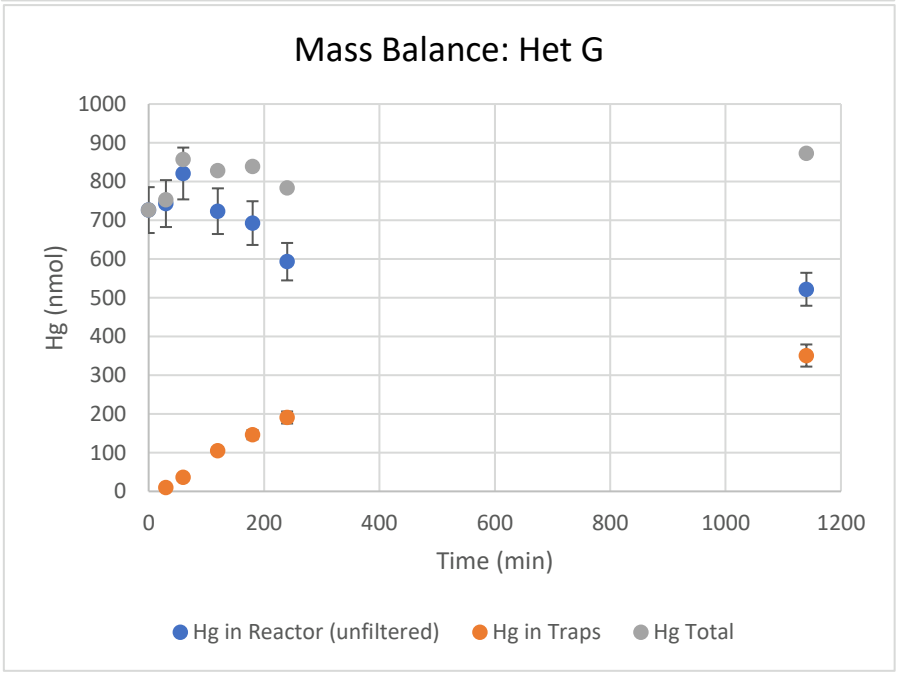

Figure 22: Mass Balances of experiments HetF and HetG. Hg in the reactor (and associated sample volumes) is represented as blue dots, the Hg captured in the traps in orange and the grey dots show the combined Hg mass as each time step.

The experiment was conducted over night, with the last sampling point taken 1140 minutes after initiation of the reaction, to counterbalance the anticipated slower reaction kinetics of the heterogeneous experiments.

In *Figure 23* a detailed look at the Hg distribution in the reactor is presented. In contrast to *Figure 22,* Hg concentration instead of the Hg-mass is illustrated on the y-axis. Note that the fraction sorbed to the Al_2O_3 particles was calculated by subtracting the dissolved fraction from the total Hg concentration; it was not actually measured.

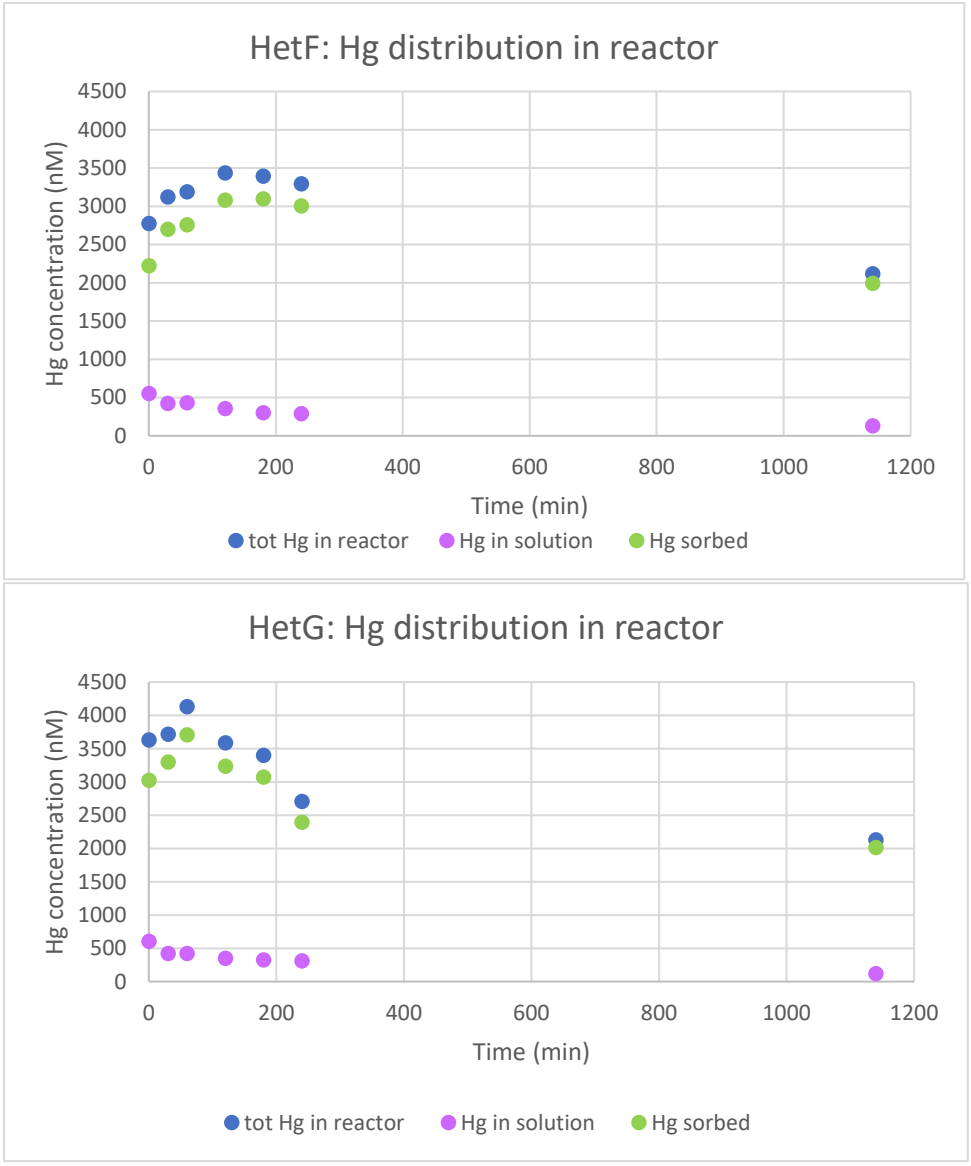

Figure 23: Hg distribution in the reactor during experiments HetF and HetG. The lavender-colored dots represent the HetF… fil and HetG… fil samples, which were filtered during sample gathering. These samples therefore inherited the concentration of the Hg fraction in solution. The blue dots show the results of the total Hg in the reactor and through these two data sets, the green dots were calculated to retrace the Hg fraction sorbed to the Al_2O_3-particles.

3.4.2 Hg Isotope Analysis

In the appendix in *Table A13,* the most important measurement data of the Hg isotope analysis on the MC-ICP-MS is presented. It shows the δ^{202}Hg, Δ^{199}Hg, Δ^{200}Hg, Δ^{201}Hg and Δ^{204}Hg of the reactor samples, the reactor samples filtered as they were collected, and the trap samples of experiments HetF and HetG.

Mass Dependent Fractionation

In the heterogeneous reduction reaction, the vaporized Hg was transferred to a single trap solution (50 ml) over the course of the experiment. At each sampling step, a sample of the trap solution was taken and later analyzed. Therefore, the data gathered this way – in contrast

to the trap data of the homogeneous experiments - represents the cumulative products in the isotope data plots.

Based on the δ^{202}Hg data presented in *Table A13*, Rayleigh fraction plots (*Figure 24*) were created for the experiments HetF and HetG separately, to calculate the fractionation factor ε that represents the MDF of these experiments, respectively. Again, linear and logarithmical fits were created for each data set (traps and reactor values), to explore the characteristics of the reaction kinetics under the created conditions (kinetically driven or equilibrium conditions). As the R^2-values suggest, the logarithmical trend lines fit their corresponding data sets better than the linear trend lines in both experiments. The isotope mass balances tilted to the heavier side of the plot, implying a predominant Hg-mass loss in the lighter fraction. The "fraction remaining"-value was calculated by the trap concentrations at each time point and applied to each sample taken at the same point in time, resulting in the sample with the lowest f-value reaching 0.56 in HetF as well as in HetG. The lavender-colored dots in *Figure 24* represent the measured δ^{202}Hg isotope data of the samples HetF0 fil - HetF6 fil and HetG0 - HetG6. In the first 30 minutes of the experiments, these samples bear a heavier isotopic composition than the bulk composition in the reactor (blue dots). After 60 minutes, the isotopic signature falls below the bulk composition and stays on the lighter side until the last sample.

As in the homogeneous experiments, the overall trend indicates a preference of the lighter isotopes. The trap values start with a lower isotopic signature than the reactor values and both pools get heavier over the course of the reaction.

The same methodical process was used for the calculation of ε as described above, resulting in ε^{202}Hg = -2.32 for HetF and ε^{202}Hg = -2.25 for HetG. Based on these ε-values, Rayleigh fractionation plots with the trend lines for the reactant, the instantaneous products and the cumulative products pools were created (*Figure 25*). The reactants and the trap data of the respective experiments were additionally inserted in the plots to determine the credibility of the calculated ε-values. The data points fit trend lines well on the left side of the plot, or rather, at low progression rate of the reaction. The difference between the reactant and the product lines is also embodied in the actual observed data. Further to the right, the data points tend to show heavier isotope values than the calculated lines predict.

Mass Independent Fractionation

The Δ^{199}Hg-data listed in *Table 13 in the Appendix* gives insight to the MIF-mechanisms of the heterogeneous experiments. Rayleigh fractionation plots of the experiments HetF and HetG are shown in *Figure 26* with logarithmical and linear trend lines for each data set. The filtered reactor samples (lavender-colored) were added to compare them to the bulk isotopic signature of the reactor (blue). The Hg isotope composition in the reactor solution samples tends to exhibit higher Δ^{199}Hg-values than in their bulk-counterparts. The only sample pair boasting the opposite case are the samples HetG6 and HetG6 fil – the last samples taken in experiment HetG.

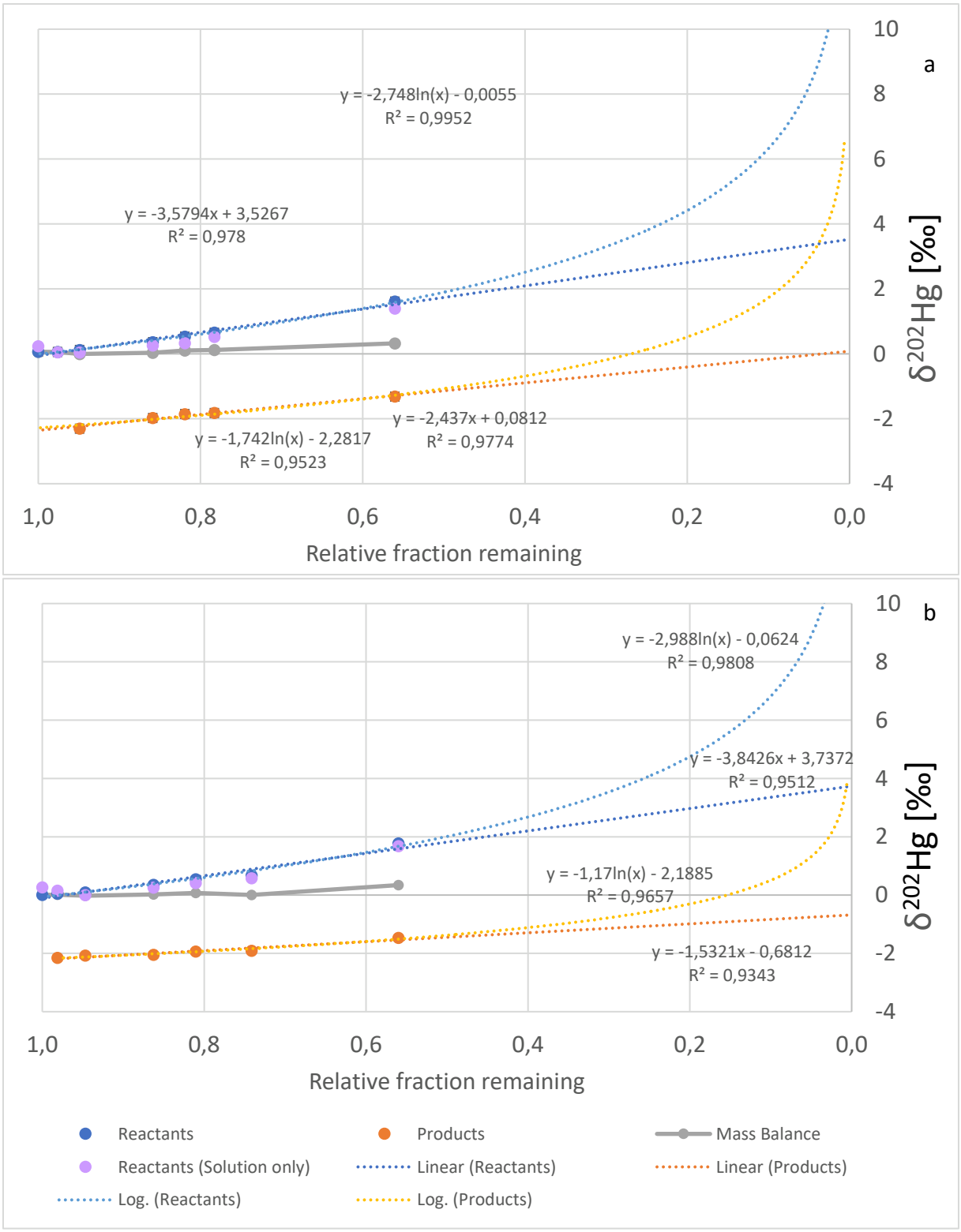

Figure 24: The graphs show the Hg isotope data of the heterogeneous experiment (a) HetF and (b) HetG as Rayleigh fractionation plots: On the x-axis, the "fraction remaining"-value f is shown. The y-axis represents the δ^{202}Hg-data measured on the MC-ICP-MS. The mass balance was calculated from the cumulative product values and the reactant values of each measured time step taking the fraction sizes into account. For both data sets, a logarithmical trendline and a linear trendline were fitted. The measurement only representing the solution fraction in the reactor, without the Hg-fraction sorbed to the Al_2O_3-particles (lavender coloured).

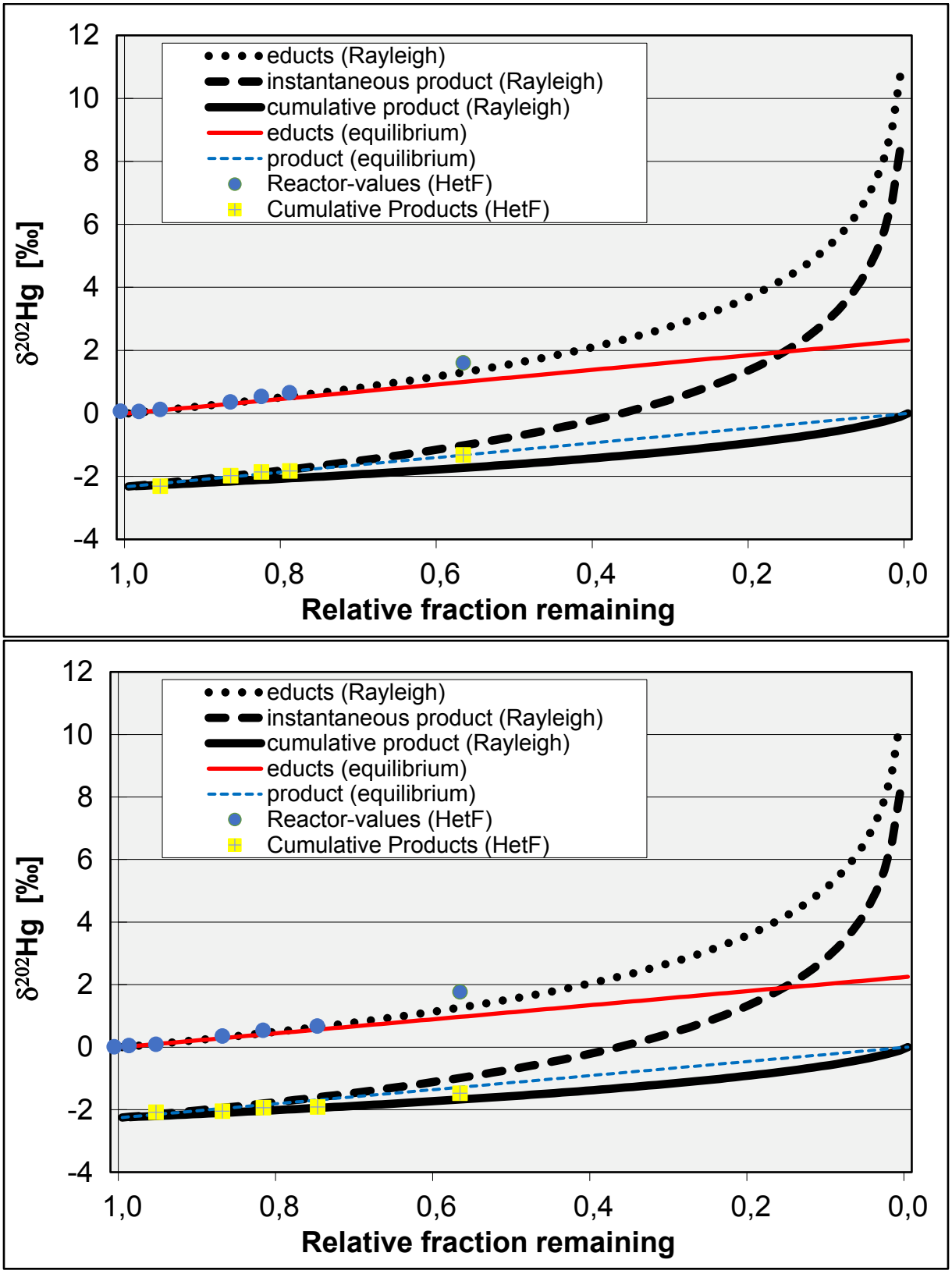

Figure 25: These Rayleigh fractionation plots were created to fit the calculated ε-values with the data sets (blue dots: reactant values, yellow squares: trap values) HetF and HetG. The three shown logarithmical trend lines (black dotted line: reactant pool, black dashed line: instantaneous products, black line: cumulative products pool) were all calculated with the *Equation 2-4* and ε being the value calculated as above. Equilibrium fits (red line: educt pool, blue dashed line: product pool) were also added with the same ε-value to visualize the kinetically driven and/or equilibrium character of the observed reaction.

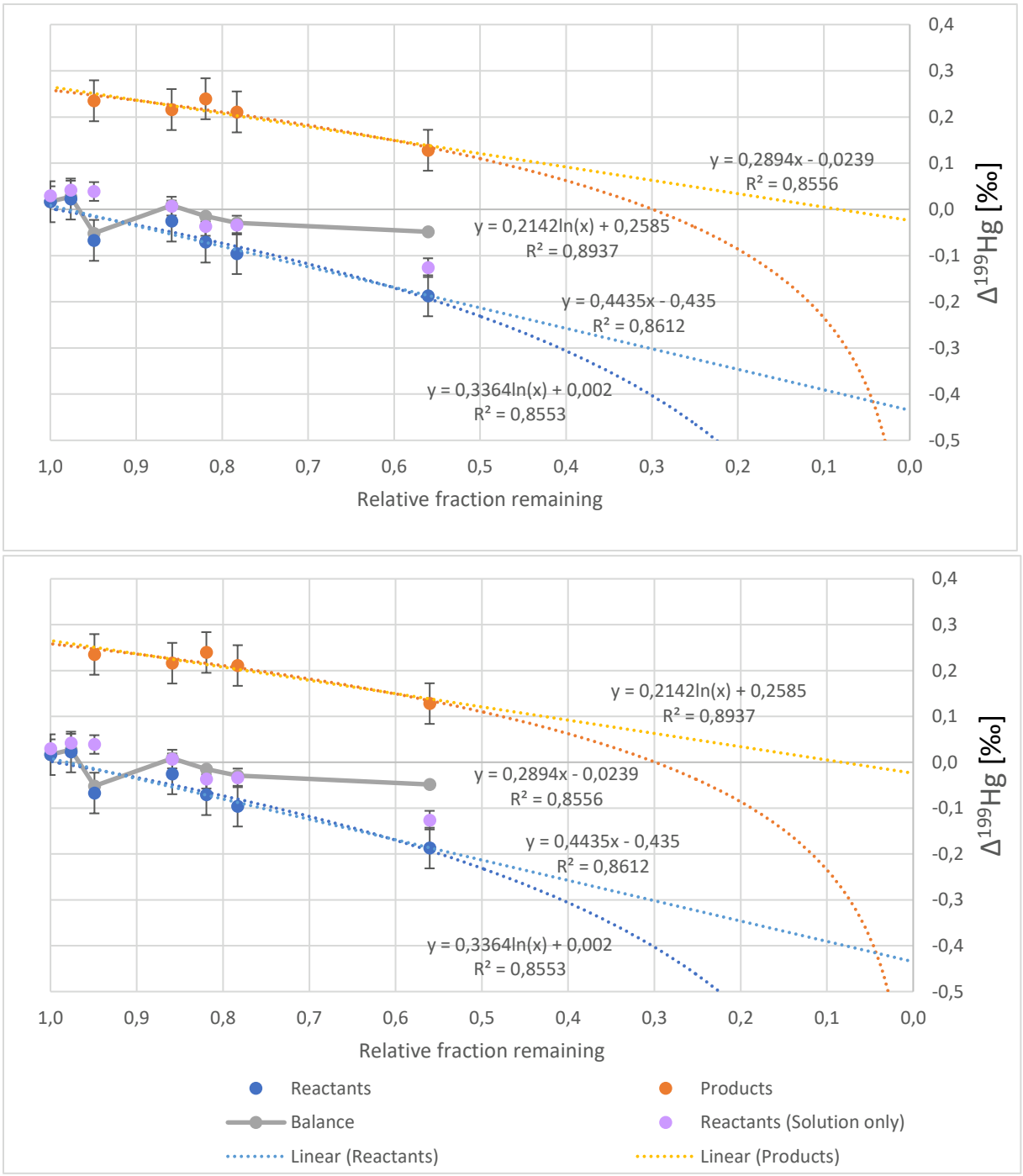

Figure 26: MIF of the experiments HetF and HetG is displayed with the "fraction remaining"-factor f on the x-axis and Δ^{199}Hg on the y-axis. Logarithmical and linear trend lines were created for the reactant data (blue dots) and the cumulative product data (orange dots). The mass balance is shown as grey dots at each point sampling. The Hg fraction only in solution without the fraction sorbed to the Al_2O_3 in the reactors is also represented (lavender colored).

In general, the Δ^{199}Hg-data of the heterogeneous experiments reveals higher discrepancies from the predominant trend regarding MIF, which is also expressed by the R^2-values of the logarithmical as well as the linear trend lines. In both experiments, the isotope mass balance start deviating from the desired value in the first 60 minutes, reaches about 0 after 120 minutes and then starts to drop below 0 again - in the direction of the reactor samples (as in

the MDF). The products values are shifted upwards from the corresponding reactor values and the trend visualized by both data sets is down the y-axis, as the reaction progresses. The MIF enrichment factor $E^{199}Hg$ was calculated for both experiments individually the same way as the MDF-factor ε was determined. For experiment HetF $E^{199}Hg$ = 0.27 ‰ and for HetG $E^{199}Hg$ = 0.25 ‰.

Determination of the Predominant Factor Causing MIF

As for the data of the homogeneous reduction experiments, the predominant effect causing MIF in the heterogeneous experiments was evaluated using a linear York regression following the protocol of *Cantrell, 2008.* The data cloud of the $\Delta^{199}Hg$- and the $\Delta^{201}Hg$-values of the experiments HetF and HetG is displayed in *Figure 27*. The MIE- and NVE-slopes (0.9 – 1.3 and 1.65) were put in contrast to the York regression linear estimated for the data cloud (1.56 ± 0.11) (Wiederhold, 2015; Zheng & Hintelmann, 2009).

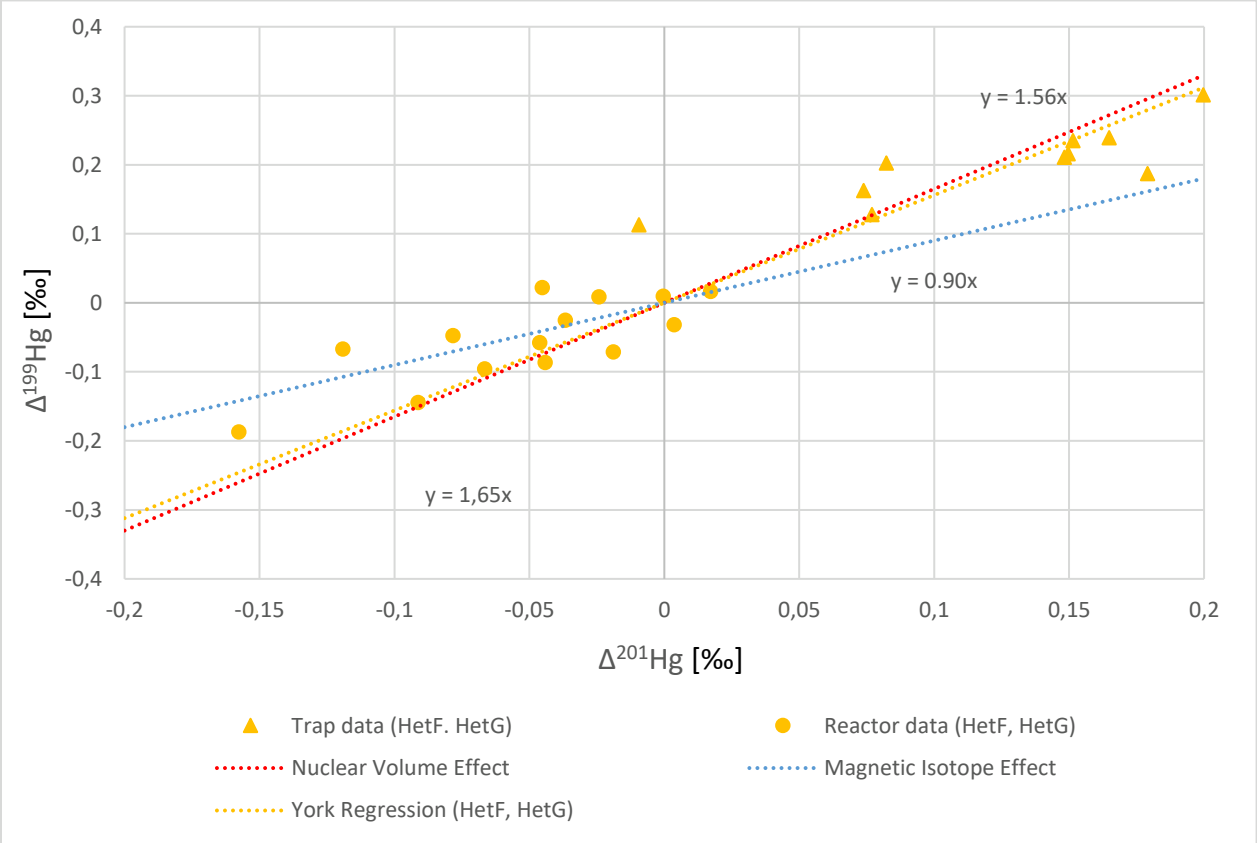

Figure 27: Comparison of the calculated slope York regression line of the heterogeneous reduction reaction data gathered in the experiments HetF and HetG in an x-y-plot with $\Delta^{199}Hg$ on the y-axis and $\Delta^{201}Hg$ on the x-axis. Dotted blue line = MIE slope (0.90), dotted red line = NVE slope (1.65), dotted yellow line = Calculated York regression (slope = 1.56 ± 0.11).

4. Discussion

4.1 Reaction kinetics: Reduction of Hg(II) to Hg(0) by Fe(II) in solution and Fe(II) sorbed to Al_2O_3

The homogeneous reaction settings offer a deeper look into the reaction kinetics of the reduction reaction between Hg(II) and Fe(II). There are two major mechanisms defining the speed of the transfer from the reaction bottles to the trap vessels: (I) The partial reactions that lead to the reduction of Hg(II) to Hg(0) and (II) the following volatilization of the reduced Hg(0) (Amirbahman et al., 2013).

Amirbahman et al., 2013 suggested second order reaction kinetics for said reaction, depending on the concentration of the Fe(II)-species $FeOH^+$ and the Hg-species $Hg(OH)_2$. The first and second order linearization calculations of the homogeneous experiments show no major difference in terms of variance, as shown in *Figure 17*. This may be due to the excess of total Fe(II) compared to Hg. The model constructed for the homogeneous reduction (*Figure 14*), shows a $FeOH^+$ concentration loss of 7 % over the course of the reduction, if 100 % Hg(II) is reduced, with the used starting concentrations. Therefore, even though the $FeOH^+$ concentration and $Hg(OH)_2$ concentration start at comparable levels, $Hg(OH)_2$ concentration drops to a much higher degree over the course of the experiment, since $FeOH^+$ is constantly reproduced from the total Fe(II)-pool. This leads to observed pseudo first order reaction kinetics, due to the relatively small concentration change of $FeOH^+$ over the whole experiment. *Amirbahman et al., 2013* postulated a second order rate constant k = 7.19 10^3 M^{-1} min^{-1}, which is slightly slower than observed in the experiments performed for this study for the reduction reaction of $Hg(OH)_2$ and $FeOH^+$ (Excel-solver solution: k = 2.04 10^4 M^{-1} min^{-1}). Several factors are assumed to be responsible this difference:

- *Amirbahman et al., 2013* measured the reduced Hg through the accumulation of Hg in the trap and not its loss in the reactor liquid, as it was in this study. Potential loss of Hg on the way from the reactor to the trap would therefore lead to lower observed Hg reduction rates than actually occurring. Moreover, purging and transportation processes to the gold traps used in the studies of *Amirbahman et al., 2013* requires time depending on gas flow rate and reactor volume, leading to lower observed reaction rates. *Kritee et al., 2007,* for example, only took the measured reactor values into account for the calculation of the fraction reacted value, since they were assumed to be more robust.
- As described above, the $FeCl_2$-solution used for this studies was purified from Fe(III) before usage. During the purification process, significant Fe(III)- precipitation could be observed. In *Amirbahman et al., 2013,* Fe(II)SO_4-salt was used to create the Fe(II)-solution without the purification step. This could have led to higher assumed Fe(II) concentration than present.

The trap values were not taken into account for the determination of the rate constant, since the reactor data was considered more robust, as it was not affected by mass loss during the transfer of Hg from the reactor to the traps. As seen in *Figure 16*, the trap data of HomQ and HomS – the experiments with severe mass loss – drop significantly below the determined

Hg(0) production curve. Using these values to calculate the rate constant of the reduction process would therefore lead to a lower k-value than observed in the reactors.
The second order linearization of the concentration loss in the reactor worked fine mathematically and led to two approaches to calculate the rate constant resulting in quite similar values: mathematical solution: $k = 7.11*10^4 \pm 0.48\ 10^4\ M^{-1}\ min^{-1}$, graphical solution resulting: $k = 7.28\ 10^4\ M^{-1}\ min^{-1}$, $R^2 = 0.99$. However, the second order linearization method is to be questioned, since one of the reactive species ($FeOH^+$) is constantly reproduced from a much greater Fe(II)-pool during the ongoing reaction.

The reaction rate was observed to decrease with increasing Al_2O_3-surface area in the reactor, which is consistent with the work of *Amirbahman et al., 2013,* as it depends highly on Hg(II) in solution. The sorption process of Hg(II) to the Al_2O_3-surface takes place much faster than the reduction reaction of $FeOH^+$ and $Hg(OH)_2$, as stated by *Amirbahman et al., 2013.* This is further backed up by the results of the sorption experiments depicted in *Figure 7* as well as the comparison of the filtered and unfiltered samples of the heterogeneous reduction experiments shown in *Figure 23*, leading to much lower Hg concentrations in solution and therefore slower reaction kinetics. This is crucial for the rate determining step in the surface catalyzed reduction pathway, as not only observed by *Amirbahman et al., 2013,* but also in studies with different heavy metals, like Cr(IV) (Buerge & Hug, 1999).
It is important to notice, that the initial main purpose of this study was the observation of the isotopic effects on Hg during the reduction reaction, not its kinetics. The study design and experimental setup were therefore primarily optimized for Hg isotope analysis.

4.2 Isotopic Effects of the Hg sorption process

Isotope fractionation effects were investigated along the process of the pre-experimentation for the heterogeneous reduction experiments. Therefore, statements made about the sorption process in this thesis are exclusively done qualitatively and not quantitatively. The calculations developed to determine fractionation factors and withstand scientific discourses can only be applied to data involving the educt and the product fractions. The effect of the sorption mechanism on the fractionation of Hg isotopes were studied on one hand by the sorption experiments, and the comparison between the two sample sets taken from the reactor suspension during the heterogeneous reduction experiments. Both these methods were planned and executed to get an overview of the fractionation process induced by the sorption mechanism, but never to state precise assertions.

4.2.1 Mass Dependent Fractionation

The results of the sorption experiments depicted in *Figure 10* and *Figure 11* show a slight tendency of the solution pool to become heavier with more Hg sorbed to the particles. Therefore, the counter pool – the fraction sorbed to the Al_2O_3-particles – is arguably becoming lighter during the same mechanism. Since the data shown in these graphs is gathered from samples taken three minutes after adding the Hg to the Al_2O_3-suspension, an initial kinetic effect to the isotope fractionation is possibly inherited in this data, which is also supported by the higher R^2-values of the logarithmical trend lines compared to the linear trend lines in the

δ^{202}Hg data set. It has been previously suggested, that initial kinetic isotope effects during the sorption process of Hg(II) to mineral surfaces (e.g. goethite) potentially takes even much greater time spans of up to several days to one month (Jiskra et al., 2014). The results are also supported by the data of the heterogeneous reduction experiments shown in *Figure 24.* By comparing the samples filtered while sampling (representing the fraction in solution, lavender-colored dots) and the bulk samples of the reactor (blue dots), heavier isotope composition in solution can be observed in the first few minutes after experimental start, which also empowers the statement, that the adsorption process favors lighter Hg isotopes to some extent. This is consistent with *Wiederhold et al., 2010* and *Jiskra et al., 2012* claiming that similar processes – isotope fractionation between dissolved Hg(II) and thiol-bound Hg(II) and Hg(II) sorption to iron oxides – have also shown to decrease δ^{202}Hg-values, as depicted in *Figure 3*. The fractionation extent also exhibits a similar range in these two studies with δ^{202}Hg-decrease ranging from 0.53 ‰ and 0.62 ‰ and observed fractionation factors between ε^{202}Hg = -0.30 ‰ to -0.44 ‰ (Jiskra et al., 2012; Wiederhold et al., 2010).
However, after one hour of reaction time, the heterogeneous reduction experiments show the opposite trend: The samples representing only the reactor solution become isotopically lighter than the bulk reactor samples, indicating that the sorbed Hg fraction becomes heavier than the fraction in solution.

4.2.2 Mass Independent Fractionation

The MIF results depicted in *Figure 11* show a similar trend for the Δ^{199}Hg alteration as seen in the MDF for δ^{202}Hg. The solution values enhance with increasing sorption rate and therefore the sorbed fraction is estimated to exhibit negative Δ^{199}Hg-values. The opposite trend can be observed in the heterogeneous experiment results shown in *Figure 26.* The Δ^{199}Hg sample data representing the solution fraction (lavender-colored) boasts higher values than the counterpart data set representing the bulk composition in the reactor (blue dots). However, this variation is very discreet, being in the range or slightly out of the range of the measuring errors. The Δ^{199}Hg shift observed in the sorption experiment data ranges from 0.04 ‰ to 0.09 ‰.
The experiments conducted for this thesis suggest that the adsorption process of Hg(II) to an Al_2O_3-surface results in a similar Hg isotope fractionation as the process of binding Hg to thiols and adsorption to iron oxide particles (Jiskra et al., 2012; Wiederhold et al., 2010). In *Jiskra et al., 2012* an explanation for the sorption fractionation mechanism is provided, as it was discovered that the equilibrium fractionation factor is independent of the pH, chloride and sulfate concentration, the type of surface complex and the equilibration time. It was suggested that the fractionation does not happen during the sorption process to – in this case – the goethite surface, but due to an equilibrium isotope effect of the Hg(II) solution species. Since the cationic species are preferably sorbed, the isotope fractionation is expressed on the mineral surfaces (ε^{202}Hg = -0.30 ‰ to -0.44‰), making it independent from the specific surface Hg(II) is sorbed onto (Jiskra et al., 2012).

4.3 Isotopic effects of Hg(II) reduction by Fe(II) in solution

The homogeneous reduction experiments conducted for this thesis offer a detailed look into the Hg isotope behavior during the reduction reaction with Fe(II) as well as Hg(II) in solution. The fraction reacted by the end of the experiments HomN and HomR has proceeded to a point where statements on the conditions of the reaction can be made (meaning if equilibrium conditions were predominant or the reaction was kinetically driven). The dataset created through these two experiments hints similar conclusions about MDF and MIF mechanisms induced by the observed reaction, resulting in more robust qualitative and quantitative interpretations.

However, with the used experimental setup, two barely distinguishable mechanisms causing Hg isotope fractionation take place: The reduction from Hg(II) to Hg(0) and the following volatilization of the reduced Hg(0). However, the volatilization only influences the fractionation, if reduced Hg(0) is not purged out of the system efficiently and rapidly as soon as it is produced, since isotope fractionation only comes into play when a pool of elements partly undergoes some transformation – not entirely. The volatilization of Hg from solution to the gaseous phase was previously studied and the highest δ^{202}Hg-value observed was 1.48 ± 0.07 ‰ (Zheng et al., 2007).

4.3.1 Mass dependent fractionation

Figure 18 compares the linear and the logarithmical trend line fitted to the HomN and HomR data. In both cases, the logarithmical fits feature lower R^2-values than the linear ones, indicating kinetically driven reaction conditions. Naturally, this becomes more obvious on the right-hand side of the plots. Therefore, the HomN data displays this phenomenon more explicitly than HomR since the reaction was more advanced by the time of the last sampling step. These results point out, that Hg(0) has been purged out of the reactor efficiently after reduction, as isotope exchange between the reduced Hg(0) and the educt Hg(II)-species would lead to observed equilibrium conditions and the linear fit would provide a better fit for the data set than the logarithmical

The MDF shown in the experiments is coherent with previously observed isotope fractionation during similar processes where Hg(II) is reduced to Hg(0), as seen in *Figure 3* (Kritee et al., 2008; Zheng & Hintelmann, 2010a). Lighter isotopes are shown to be preferably reduced in those reactions. The pool left behind therefore becomes heavier as the reaction continues, like in the sorption experiments. However, the effect is far more drastic: The isotope ratios reach values of up to 4.22 ‰ and 3.00 ‰ in the last samples of HomN and HomR, respectively, even with a slightly lower “fraction reacted”-factor. For HomN and HomR ε^{202}Hg = -2.79 ‰ and ε^{202}Hg = -2.93 ‰ were calculated, respectively, as seen in *Figure 19.* The observed MDF is therefore much more pronounced than the fractionation observed in the isolated volatilization process.

The way the f-value was calculated, however, is worth discussing, since both the reactor and the trap concentration values could be put into relation with the total Hg. The trap concentration values were used, as the reactor samples are estimated to be more vulnerable to other processes than the reduction and subsequent vaporization, like sorption to the reactor walls. Also, if not all the Hg(0) is purged out immediately, it possibly falsifies the

isotopic signature in the reactor. The traps can only contain the fraction the has been reduced and purged to the traps.

4.3.2 Mass independent fractionation

In *Figure 20* a comparison between the logarithmical fit and the linear fit of the HomN and HomR Δ^{199}Hg-data is portrayed to clarify the reaction conditions. Again, the logarithmical trend lines suit the data set better, exposing kinetically driven reaction conditions, as the MDF data does. In contrast to the MIF evoked by the sorption process, the Δ^{199}Hg-values of the reactant drop throughout the course of the experiment, meaning that the isotopic signature change triggered by the reduction by Fe(II) proceeds in the opposite direction. This direction was predicted in previous studies (Wiederhold et al., 2010). It is also more significant than the MIF caused by the sorption process: HomN reveals a measured Δ^{199}Hg-values up to -0.36 ‰ and HomR -0.26 ‰, both in the last samples taken. A linear trend line representing the homogeneous reduction of Hg(II) by Fe(II) in solution in a δ^{202}Hg / Δ^{199}Hg plot, as seen in *Figure 3* shows a slope of ~ -0.1. The York regression calculated for the Δ^{199}Hg / Δ^{201}Hg-data cloud of the experiments HomN and HomR has a slope equal to 1.70 ± 0.12, indicating that NVE (theoretical slope of ~1.65,) was the predominant effect causing MIF (Ghosh et al., 2013; Yang & Liu, 2015). The MDF and MIF results of the homogeneous reduction facilitate a possible distinction between different processes previously investigated and the reaction observed in this study not only quantitatively - which is hard to distinguish in natural settings – but also qualitatively. For example, microbial reduction of Hg(II) to Hg(0) evoked MDF favoring the lighter isotopes, but no MIF exceeding measurement errors could be determined (Kritee et al., 2009). Photochemical reduction has also been reported to prefer the lighter isotope fraction, but in the Δ^{204}Hg MIF a signature is inherited. MIF can be observed in the positive and the negative direction and MIE can also be accountable for MIF (Motta et al., 2020).

4.4 Isotope effects of Hg(II) reduction by Fe(II) sorbed to an unreactive Al_2O_3-surface

Of all the experiments conducted the heterogeneous reduction experiments were the most vulnerable to disruptive factors. A lot of experience from previous work (homogeneous experiments, sorption experiments, trial experiments listed in the Appendix) had to go into them to gain data representing the Hg isotope fractionation mechanisms triggered by the reduction reaction with Fe(II) bound to an unreactive Al_2O_3 surface. The Fe-content in the reactor solution was measured at the beginning and at the end of the experiments with the Plate Reader, to control if any Hg could have been reduced by Fe(II) in solution instead of Fe(II) bound to the Al_2O_3 surface. Since the reaction of Hg(II) with dissolved Fe(II) is significantly faster than the reaction with adsorbed Fe(II), its contribution to the change in isotopic composition change in the different pools could be considerably high even at low concentrations of Fe(II) in solution.

The concentration measurement results of HetF and HetG emphasize the difficulty of the heterogeneous reaction settings: Even with ten times higher initial Hg concentrations than in the homogeneous experiments, the kinetics are slowed down to a degree that makes it hard to drive the reaction to a point where a decision about the reaction conditions (equilibrium or

kinetically driven) can be made unambiguously. As seen in *Figure 22* the Hg concentration results show a very unexpected trend. The first few measurements should be higher and constantly dropping afterwards but not increase initially. This phenomenon was observed in both experiments, making measurement errors as an explanation unlikely. The trap results, however, seem to be more reliable. The Hg mass captured in them increased constantly over the course of both experiments. Possible explanations for this phenomenon are for example (a) an inhomogeneous distribution of Hg in the reactor or the particles Hg is sorbed onto at the beginning of the experiment leading to an incomplete sampling, (b) insufficient remobilization from the Al_2O_3 particles before the concentration measurement.

4.4.1 Mass dependent fractionation

The isotope results of the heterogeneous experiments (*Figure 24*) do not resemble the oddities of the concentration measurements of the reactor samples, which could hint sampling issues. If Hg was not suspended homogenously or some of it was stuck to the reactor walls, similar faults could be seen in the concentration values of the reactor. The isotope measurements as well as the concentration measurements of the traps, however, could be unaffected. The reactor values show a similar trend as in HomN and HomR. However, the MDF is slightly less significant (HetF: $\varepsilon^{202}Hg$ = -2.32 ‰, HetG: $\varepsilon^{202}Hg$ = -2.25 ‰).

The comparison of the isotopic signature of the solution fraction and the total reactor composition shows an odd trend, as already mentioned in *sec 4.2.* At first, the solution fraction becomes heavier than the overall reactor content. After one hour of experimental time, however, this trend changes to the opposite direction and the solution constantly boasts a lighter isotopic signature than the bulk. This observation could give insight into the reaction mechanism and a hypothesis can be formulated based on two previously stated findings: (a) The kinetics observed for the two relevant mechanisms are very different - the sorption of Hg to the Al_2O_3 particles occurs within a few minutes and the reduction reaction takes place over the time span of many hours. (b) The quantitative difference in MDF between these two mechanisms.

At first, the adsorption of Hg to the Al_2O_3 particles is more relevant, as the reduction has progressed to a much lower degree and the sorbed fraction becomes lighter, leaving the solution fraction heavier, as seen in the samples. However, after 30-60 minutes, the adsorption process reaches almost a plateau while the reduction reaction is still ongoing and kinetically driven and due to its much higher impact on the Hg isotope fractionation - favoring lighter isotopes more than the sorption process by about a factor 10 - the solution fraction becomes lighter than the adsorbed fraction and therefore lighter than the bulk. This indicates that reduction preferably takes place on the sorbed fraction rather than the fraction in solution. Due to Hg cation exchange between Hg(II) in solution and Hg(II) sorbed to the Al_2O_3, the isotopic composition of the solution fraction gravitates towards the composition of the adsorbed fraction. This hypothesis suggests, that Hg sorbed to Al_2O_3 is more likely to be reduced by the Fe(II) adsorbed to the Al_2O_3 particles than Hg ions in solution. To some degree, this hypothesis contradicts the findings of the kinetics of the homogeneous and the heterogeneous reaction kinetics as well as the findings of *Amirbahman et al., 2013* regarding this matter. It was shown that the presence of Al_2O_3 particles slows down the reaction kinetics,

so faster reaction kinetics on the surface sites than in the solution fraction seems counterintuitive. However, the Fe(II) is bound to the particles and not in solution. This could change the reaction mechanism to a higher likelihood of sorbed Hg(II) being reduced than Hg(II) in solution.
The R^2-values of the linear and logarithmical trend lines for the heterogeneous experiments are so close to each other that a clear statement about the reaction conditions cannot be made, although the logarithmical lines fit slightly better in both HetF and HetG. This is caused by the fact, that the reaction did not progress to a point where linear and logarithmical trends display large differences. In both experiments, only 44 % of the Hg(II) was reduced. The isotopic mass balance drifts towards the reactant composition over the course of the reaction. This makes sense since the concentration analysis reveals a mass loss of 12.7 % and 12.8 % which can likely be attributed to Hg missing in the fraction of the produced Hg(0).

4.4.2 Mass independent fractionation

The MIF factors calculated with the Δ^{199}Hg-values depicted of the heterogeneous reduction experiments in *Figure 25* reveal E^{199}Hg = 0.27 ‰ and E^{199}Hg = 0.25 ‰ for HetF and HetG, respectively. Again, this mirrors the results of the homogeneous experiments: The trend is similar, but the fractionation is not as drastic as observed in the solution reaction. However, the data set is much less clean and both the logarithmical and the linear trend line show lower R^2-values than in the homogeneous reduction reaction. The effect causing MIF seems to be the NVE, as the York Regression calculated for the HetF and HetG data has a slope of 1.56 ± 0.11 in the Δ^{199}Hg / Δ^{201}Hg-plot.
Comparing the homogeneous and the heterogeneous reduction experiments, quite similar trends can be observed. In terms of MIF there is no major difference observable. Both show a positive E^{199}Hg that also quantitatively does not deviate from one another. The Δ^{199}Hg / Δ^{201}Hg regression line indicates that NVE is responsible for the observed MIF in both cases. The MDF of the observed reactions also qualitatively follow the same trend, however, the homogeneous reaction favors lighter isotopes more drastically. When it comes to process tracing, this difference is quite subtle and being able to differentiate between these processes based on stable isotope analysis is hard to imagine, though. The deviation of the heterogeneous MDF-factor from the homogeneous one stands in contrast to the expected impact of the slower reaction kinetics, as they should lead to higher extend of isotope fractionation (Basu et al., 2020). The sorption process was shown to fractionate Hg isotopes in the same direction but to a much lower degree than the reduction process, which could be expected as the sorption process takes place much faster than the reduction reaction.

4.5 Extent of MDF and MIF

The results show quite distinct isotope fractionation behavior compared to previous investigations either in terms of MDF, MIF or both. Those deviations are not only observable quantitatively, but also from the general direction, the fractionation trend is leading to. For example, microbial reduction and photoreduction in the presence of DOM showed no MIF, even though the MDF also favored lighter isotopes, but to a minor extend (Kritee et al., 2009; Zheng & Hintelmann, 2009). Photoreduction of intercellular Hg and cysteine bound Hg was

Table 5: Comparison between the isotope fractionation results of this study and different fractionation factors determined in previous studies ([1]Zheng & Hintelmann, 2010b, [2]Kritee et al., 2007, 2008, [3]Bergquist & Blum, 2007; Zheng & Hintelmann, 2009, [4]Kritee et al., 2018, [5]Zheng & Hintelmann, 2010a, [6]Wang et al., 2021).

	Experiment	Mass Dependent Fractionation Factor	Mass Independent Fractionation Factor	$\Delta^{199}Hg/\Delta^{201}Hg$
Data collected In this study	Reduction with Fe(II) in solution	$\varepsilon^{202}Hg$ = -2.93 ‰; -2.79 ‰	$E^{199}Hg$ = 0.29 ‰; 0.30 ‰	1.70 ± 0.12
	Reduction with Fe(II) sorbed to Al_2O_3	$\varepsilon^{202}Hg$ = -2.25 ‰; -2.32 ‰	$E^{199}Hg$ = 0.25 ‰; 0.27 ‰	1.56 ± 0.11
	Sorption to Al_2O_3	$\delta^{202}Hg$ = -0.24 – -0.45 ‰	$\Delta^{199}Hg$ = 0.04 – 0.09 ‰	
Data collected in previous studies	Dissolved Organic Matter[1]	$\varepsilon^{202}Hg$ = -1.52 ± 0.06 ‰	$E^{199}Hg$ = 0.19 ‰	1.60 ± 0.12
	Microbial reduction[2]	$\varepsilon^{202}Hg$ = -0.60 - -1.80 ‰	no MIF	No MIF
	Photoreduction in presence of DOM[3]	$\varepsilon^{202}Hg$ = -0.60 - -1.09 ‰		1.0-1.31
	Dark reduction with $SnCl_2$[1]	$\varepsilon^{202}Hg$ = -1.56 ‰; -1.77 ‰	$E^{199}Hg$ = 0.17 ‰; 0.26 ‰	1.59; 1.62
	Photoreduction of intercellular Hg(II)[4]	$\varepsilon^{202}Hg$ = -0.7 ‰ - -0.8 ‰	$E^{199}Hg$ = 0.89 ‰ - 1.03 ‰	~1.0
	Photoreduction of cysteine bound Hg(II)[5]	$\varepsilon^{202}Hg$ = -1.32 ± 0.07 ‰	$E^{199}Hg$ = 1.02 ‰	1.46 ± 0.03
	Hg(II) reduction by siderite (equilibrium conditions)[6]	$\varepsilon^{202}Hg$ = -2.43 ± 0.38 ‰	$E^{199}Hg$ = 0.28 ± 0.06 ‰	1.06 (uncertain)
	Hg(II) reduction by green rust (equilibrium conditions)[6]	$\varepsilon^{202}Hg$ = -2.28 ± 0.40 ‰	$E^{199}Hg$ = 0.28 ± 0.06 ‰	1.06 (uncertain)
	Hg(II) – Hg(0) equilibration[6]	$\varepsilon^{202}Hg$ = -2.63 ± 0.37 ‰ (no Chloride) $\varepsilon^{202}Hg$ = -2.77 ± 0.70 ‰ (10mM Chloride)	$E^{199}Hg$ = 0.28 ± 0.21 ‰	1.44

observed to fractionate Hg isotopes to a similar extend in terms of MDF and MIF (Kritee et al., 2018; Zheng & Hintelmann, 2010a). Despite preferring isotopes in the same direction as observed in the experiments for this study, the extend of MDF exceeded MIF about tenfold. MDF as well as MIF observed with Fe(II)-bearing minerals like siderite and green rust has been reported to be very similar to the results seen for the reduction with Fe(II) in solution and bound to Al2O3 (Wang et al., 2021). In Table 5, a comparison between the Hg fractionation values found in previous studies and the observed data of this study is given.

4.6 Weaknesses and possible Improvements for the experimental set-up

Although a lot of thought went into the experimental setup, it still has some weaknesses that must be addressed to help similar future projects to improve the data quality.

- In almost every experiment, a slow Hg transfer from the reactor bottles to the trap vessels can be observed. This is reflected in the mass balance plots of the reduction experiments (*Figure 15* and *Figure 22*). Most of the time, the mass balance is quite off at the beginning of the experiments and by the end it "recovers" to some degree. The process of volatilizing the reduced Hg(0) into the gaseous phase and subsequently transferring it to the trap seems to take a few minutes to be completed. Therefore, a fraction of the Hg is present as dissolved Hg(0) in the reactors or in the gaseous phase between the reactor and the associated trap if they are measured almost at the same time. This phenomenon is more relevant during the first sampling steps, when a lot of Hg is reduced in short periods of time. It is therefore recommended to use high gas flow for efficient purging of the produced Hg(0).
- Increasing the gas flow for an improved Hg(0) removal from the reactors bears the risk of less efficient retention of Hg in the oxidizing traps. Potential breakthrough could be tested by adding a second trap.
- Sampling the reactor bottle requires short opening of the valve in the cap of the reactor bottle. During that time, Hg(0) can escape. This effect was even amplified in the heterogeneous reduction experiments since the nitrogen gas flow could not be paused for the sampling steps. If it was stopped, backpressure caused permanent cloaking of the inlet gas tube, which resulted in total failure of the experiment.
- Hg(0) could potentially also evaporate while transferring the liquid out of the reactor and into the sample tube before mixing with the BrCl conc. This would also be enhanced by the filtration step needed in the heterogeneous experiments.

5. Conclusion

The aim of this study was to investigate the Hg isotope fractionation during the reduction of Hg(II) to Hg(0) by dissolved and surface bound Fe(II). To conclude and summarize the presented data, the three research questions presented in the introduction will be answered.

Question 1

In which way are Hg isotopes fractionated during the reduction reaction with Fe(II) in solution, in terms of MDF as well as MIF?

The homogeneous reduction of Hg with Fe(II) dissolved in water (pH = 8, [NaCl] = 342µM, dark anoxic conditions) was found to show MDF of the Hg isotopes with $\varepsilon^{202}Hg$ = -2.79 ‰ and $\varepsilon^{202}Hg$ = -2.93 ‰ favoring lighter isotopes and positive MIF with $E^{199}Hg$ = 0.29 ‰ and $E^{199}Hg$ = 0.30 ‰ for two sets of experiments, respectively. For both experiments, the isotope analysis results point out kinetically driven conditions. The mechanism responsible for MIF is most likely NVE, since the data set of the two experiments account for a slope of 1.70 ± 0.12 in the $\Delta^{199}Hg$ / $\Delta^{201}Hg$-plot for the calculated least square York-regression line.

Question 2

How is the isotope fractionation affected, if the reduction of Hg is induced by Fe(II) sorbed to an unreactive boehmite surface instead of dissolved in water?

For the two heterogeneous reduction experiments, where Fe(II) was firstly sorbed to unreactive Al_2O_3 particles in suspension and subsequently Hg added to the solution, MDF with $\varepsilon^{202}Hg$ = -2.32 and $\varepsilon^{202}Hg$ = -2.25 and MIF with $E^{199}Hg$ = 0.27 and $E^{199}Hg$ = 0.25 were calculated. This is against the hypothesis that slower reaction kinetics lead to larger a extent of isotope fractionation. NVE is assumed to be the responsible mechanism for the MIF, as the slope of the linear regression line in the $\Delta^{199}Hg/\Delta^{201}Hg$-plot was calculated to be 1.56 ± 0.11, being close to the theoretical NVE slope, as in the homogeneous reduction experiments. Based on the results of the experiments conducted for this thesis, a quantitative distinction between the homogeneous reduction reaction of Fe(II) and Hg(II), and the heterogeneous reaction with the same components but Fe(II) is sorbed to an unreactive Al_2O_3 surface, is possible. However, since natural systems do not offer isolated reaction conditions as experiments designed for the laboratory do, and several chemical reactions occur in parallel, the applicability on natural samples of the knowledge gained from these experiments depends on future progresses in the heavy metal isotope study field.

Question 3

How do the observed isotope fractionations of the homogeneous and heterogeneous experiments compare to isotope behavior of previously investigated reactions including Hg?

The results of the study demonstrate significant differences in isotope fractionation behavior compared to previous research, both in terms of MDF and MIF. These differences are not only

quantitatively observable but also in the overall direction of the fractionation trend. For instance, in experiments involving microbial Hg(II) reduction, although there was a preference for lighter isotopes in terms of MDF, there was no significant MIF observed. Similarly, photoreduction of Hg(II) in the presence of DOM resulted in isotopic fractionation, but the extent of and direction of MIF were different. This indicates a distinct behavior in isotopic fractionation during Hg(II) by Fe(II) compared to prior investigations.

Pre-experiments, conducted to gain a better understanding of the sorption process of Hg(II) and Fe(II) to the Al_2O_3-particles for the heterogeneous reduction experiments, where also analyzed on the MC-ICP-MS and gave insight into the isotope fractionation mechanisms of the Hg sorption process. Due to a lack of data quality, a quantitative $\varepsilon^{202}Hg$ or $E^{199}Hg$ could not be calculated as it was for the reduction experiments, but qualitative trends are clearly visible. MDF leaves the solution pool slightly heavier than the bulk isotopic composition, implying that the lighter Hg isotopes have a higher tendency to be sorbed to Al_2O_3-particles. When 81-88 % of the Hg is sorbed, Hg deviation between 0.24 ‰ and 0.45 ‰ could be observed, which is about ten times less fractionation than measured in the reduction reaction samples. The first samples of the heterogeneous experiments, when the reduction process has not progressed to a far extent, follows this trend. MIF was observed in the $\Delta^{199}Hg$ results below 0.1 ‰, making statements about that somewhat questionable. This slight difference, however, trends in the opposite directions than in the reduction experiments and theoretically predicted. The solution shows marginally higher $\Delta^{199}Hg$-values than initially, leaving the sorbed fraction with a lower $\Delta^{199}Hg$ signature.

With the results of the investigations of this thesis, the pathway for studies about the effect of the Hg reduction by Fe(II)-bearing minerals on Hg isotopes is laid to get further insights into the mechanisms of these reactions. With such minerals, the Fe(II)-source would be closer to natural conditions. This could also be amplified by changing other settings in the experimental set up. Isotope exchange could be allowed during the reaction, which likely happens in natural groundwaters during Hg(II) reduction pathways.

References

Amirbahman, A., Kent, D., Curtis, G., & Marvin-Dipasquale, M. (2013). Kinetics of Homogeneous and Surface-Catalyzed Mercury(II) Reduction by Iron(II). Environmental Science & Technology, 47. https://doi.org/10.1021/es401459p

Basu, A., Wanner, C., Johnson, T. M., Lundstrom, C. C., Sanford, R. A., Sonnenthal, E. L., Boyanov, M. I., & Kemner, K. M. (2020). Microbial U Isotope Fractionation Depends on the U(VI) Reduction Rate. Environmental Science & Technology, 54(4), 2295–2303. https://doi.org/10.1021/acs.est.9b05935

Bergquist, B. A., & Blum, J. D. (2007). Mass-Dependent and -Independent Fractionation of Hg Isotopes by Photoreduction in Aquatic Systems. Science, 318(5849), 417–420. https://doi.org/10.1126/science.1148050

Bloom, N. S., Preus, E., Katon, J., & Hiltner, M. (2003). Selective extractions to assess the biogeochemically relevant fractionation of inorganic mercury in sediments and soils. Analytica Chimica Acta, 479(2), 233–248. https://doi.org/10.1016/S0003-2670(02)01550-7

Blum, J. (2011). Applications of Stable Mercury Isotopes to Biogeochemistry. In Handbook of Environmental Isotope Geochemistry (pp. 229–245). https://doi.org/10.1007/978-3-642-10637-8_12

Blum, J., Sherman, L., & Johnson, M. (2014). Mercury Isotopes in Earth and Environmental Sciences. Annual Review of Earth and Planetary Sciences, 42, 249–269. https://doi.org/10.1146/annurev-earth-050212-124107

Boening, D. (2000). Ecological effects, transport, and fate of mercury: A general review. Chemosphere, 40, 1335–1351. https://doi.org/10.1016/S0045-6535(99)00283-0

Bone, S., Bargar, J., & Sposito, G. (2014). Mackinawite (FeS) Reduces Mercury(II) under Sulfidic Conditions. Environmental Science & Technology, 48. https://doi.org/10.1021/es501514r

Brezonik, P. L. (2015). Water Chemistry. In Kirk-Othmer Encyclopedia of Chemical Technology (pp. 1–19). John Wiley & Sons, Ltd. https://doi.org/10.1002/0471238961.koe00001

Buerge, I. J., & Hug, S. J. (1999). Influence of Mineral Surfaces on Chromium(VI) Reduction by Iron(II). Environmental Science & Technology, 33(23), 4285–4291. https://doi.org/10.1021/es981297s

Cantrell, C. (2008). Technical Note: Review of methods for linear least-squares fitting of data and application to atmospheric chemistry problems. Atmospheric Chemistry and Physics Discussions, 8. https://doi.org/10.5194/acpd-8-6409-2008

Charlet, L., Bosbach, D., & Peretyashko, T. (2002). Natural attenuation of TCE, As, Hg linked to the heterogeneous oxidation of Fe(II): An AFM study. Chemical Geology, 190(1), 303–319. https://doi.org/10.1016/S0009-2541(02)00122-5

Coulibaly, M., Mazrui, N. M., Jonsson, S., & Mason, R. P. (2021). Abiotic Reduction of Mercury(II) in the Presence of Sulfidic Mineral Suspensions. Frontiers in Environmental Chemistry, 2. https://www.frontiersin.org/articles/10.3389/fenvc.2021.660058

Dideriksen, K., Frandsen, C., Bovet, N., Wallace, A. F., Sel, O., Arbour, T., Navrotsky, A., De Yoreo, J. J., & Banfield, J. F. (2015). Formation and transformation of a short range

ordered iron carbonate precursor. Geochimica et Cosmochimica Acta, 164, 94–109. https://doi.org/10.1016/j.gca.2015.05.005

EPA. (2002). EPA, 2002. Method 1631, Revision E: Mercury in Water by Oxydation, Purge and Trap, and Cold Vapor Atomic Fluorescence Spectrometry. https://www.epa.gov/sites/default/files/2015-08/documents/method_1631e_2002.pdf

Etique, M., Bouchet, S., Byrne, J. M., ThomasArrigo, L. K., Kaegi, R., & Kretzschmar, R. (2021). Mercury Reduction by Nanoparticulate Vivianite. Environmental Science & Technology, 55(5), 3399-3407-3399–3407. https://doi.org/10.1021/acs.est.0c05203

Fry, B. (2006). Stable Isotope Ecology. https://doi.org/10.1007/0-387-33745-8

Futsaeter, G., & Wilson, S. (2013). The UNEP Global Mercury Assessment: Sources, Emissions and Transport. E3S Web of Conferences, 1, 36001–36001. https://doi.org/10.1051/e3sconf/20130136001

Ghosh, S., Schauble, E. A., Lacrampe Couloume, G., Blum, J. D., & Bergquist, B. A. (2013). Estimation of nuclear volume dependent fractionation of mercury isotopes in equilibrium liquid–vapor evaporation experiments. Chemical Geology, 336, 5–12. https://doi.org/10.1016/j.chemgeo.2012.01.008

Ha, J., Zhao, X., Yu, R., Barkay, T., & Yee, N. (2017). Hg(II) reduction by siderite (FeCO3). Applied Geochemistry, 78, 211–218. https://doi.org/10.1016/j.apgeochem.2016.12.017

Hintelmann, H. (2010). Organomercurials. Their formation and pathways in the environment. Metal Ions in Life Sciences, 7, 365–401. https://doi.org/10.1039/BK9781847551771-00365

Hoefs, J. (2015). Stable isotope geochemistry, seventh edition. Stable Isotope Geochemistry, 1–389. https://doi.org/10.1007/9783319197166

Janssen, S. E., Lepak, R. F., Tate, M. T., Ogorek, J. M., DeWild, J. F., Babiarz, C. L., Hurley, J. P., & Krabbenhoft, D. P. (2019). Rapid pre-concentration of mercury in solids and water for isotopic analysis. Analytica Chimica Acta, 1054, 95–103. https://doi.org/10.1016/j.aca.2018.12.026

Jiskra, M., Saile, D., Wiederhold, J. G., Bourdon, B., Björn, E., & Kretzschmar, R. (2014). Kinetics of Hg(II) Exchange between Organic Ligands, Goethite, and Natural Organic Matter Studied with an Enriched Stable Isotope Approach. Environmental Science & Technology, 48(22), 13207–13217. https://doi.org/10.1021/es503483m

Jiskra, M., Wiederhold, J. G., Bourdon, B., & Kretzschmar, R. (2012). Solution Speciation Controls Mercury Isotope Fractionation of Hg(II) Sorption to Goethite. Environmental Science & Technology, 46(12), 6654–6662. https://doi.org/10.1021/es3008112

Joe-Wong, C., Weaver, K., Brown, S., & Maher, K. (2021). Chromium isotope fractionation during reduction of Chromium(VI) by Iron(II/III)-bearing clay minerals. Geochimica et Cosmochimica Acta, 292, 235–253. https://doi.org/10.1016/j.gca.2020.09.034

Kavner, A., Bonet, F., Shahar, A., Simon, J., & Young, E. (2005). The isotopic effects of electron transfer: An explanation for Fe isotope fractionation in nature. Geochimica et Cosmochimica Acta, 69(12), 2971–2979. https://doi.org/10.1016/j.gca.2005.01.014

Kitchen, J., Johnson, T., Bullen, T., Zhu, J., & Raddatz, A. (2012). Chromium isotope fractionation factors for reduction of Cr(VI) by aqueous Fe(II) and organic molecules.

Geochimica et Cosmochimica Acta, 89, 190-201-190–201. https://doi.org/10.1016/j.gca.2012.04.049

Kocman, D., Horvat, M., Pirrone, N., & Cinnirella, S. (2013). Contribution of contaminated sites to the global mercury budget. Environmental Research, 125, 160–170. https://doi.org/10.1016/j.envres.2012.12.011

Kritee, K., Barkay, T., & Blum, J. D. (2009). Mass dependent stable isotope fractionation of mercury during mer mediated microbial degradation of monomethylmercury. Geochimica et Cosmochimica Acta, 73(5), 1285–1296. https://doi.org/10.1016/j.gca.2008.11.038

Kritee, K., Blum, J. D., & Barkay, T. (2008). Mercury Stable Isotope Fractionation during Reduction of Hg(II) by Different Microbial Pathways. Environmental Science & Technology, 42(24), 9171–9177. https://doi.org/10.1021/es801591k

Kritee, K., Blum, J. D., Johnson, M. W., Bergquist, B. A., & Barkay, T. (2007). Mercury Stable Isotope Fractionation during Reduction of Hg(II) to Hg(0) by Mercury Resistant Microorganisms. Environmental Science & Technology, 41(6), 1889–1895. https://doi.org/10.1021/es062019t

Kritee, K., Motta, L. C., Blum, J. D., Tsui, M. T.-K., & Reinfelder, J. R. (2018). Photomicrobial Visible Light-Induced Magnetic Mass Independent Fractionation of Mercury in a Marine Microalga. ACS Earth and Space Chemistry, 2(5), 432–440. https://doi.org/10.1021/acsearthspacechem.7b00056

Lindberg, S. E., & Stratton, W. J. (1998). Atmospheric Mercury Speciation: Concentrations and Behavior of Reactive Gaseous Mercury in Ambient Air. Environmental Science & Technology, 32(1), 49–57. https://doi.org/10.1021/es970546u

Liu, G., Cai, Y., & O'Driscoll, N. J. (2012). Environmental chemistry and toxicology of mercury.

Liu, S., & Wiatrowski, H. A. (2018). Reduction of Hg(II) to Hg(0) by Biogenic Magnetite from two Magnetotactic Bacteria. Geomicrobiology Journal, 35(3), 198–208. https://doi.org/10.1080/01490451.2017.1362076

Minamata Convention on Mercury. (n.d.). Article 1.

Mishra, B., O'Loughlin, E. J., Boyanov, M. I., & Kemner, K. M. (2011). Binding of HgII to High-Affinity Sites on Bacteria Inhibits Reduction to Hg0 by Mixed FeII/III Phases. Environmental Science & Technology, 45(22), 9597–9603. https://doi.org/10.1021/es201820c

Morin, G., Noël, V., Menguy, N., Brest, J., Baptiste, B., Tharaud, M., Ona-Nguema, G., Ikogou, M., Viollier, E., & Juillot, F. (2017). Nickel accelerates pyrite nucleation at ambient temperature. Geochemical Perspectives Letters, 6–11. https://doi.org/10.7185/geochemlet.1738

Motta, L. C., Kritee, K., Blum, J. D., Tsz-Ki Tsui, M., & Reinfelder, J. R. (2020). Mercury Isotope Fractionation during the Photochemical Reduction of Hg(II) Coordinated with Organic Ligands. The Journal of Physical Chemistry A, 124(14), 2842–2853. https://doi.org/10.1021/acs.jpca.9b06308

Nordin, J., Persson, P., Laiti, E., & Sjöberg, S. (1997). Adsorption of o-Phthalate at the Water−Boehmite (γ-AlOOH) Interface: Evidence for Two Coordination Modes. Langmuir, 13. https://doi.org/10.1021/la970066g

O'Loughlin, E. J., Boyanov, M. I., Kemner, K. M., & Thalhammer, K. O. (2020). Reduction of Hg(II) by Fe(II)-Bearing Smectite Clay Minerals. Minerals, 10(12), Article 12. https://doi.org/10.3390/min10121079

O'Loughlin, E. J., Kelly, S. D., Kemner, K. M., Csencsits, R., & Cook, R. E. (2003). Reduction of AgI, AuIII, CuII, and HgII by FeII/FeIII hydroxysulfate green rust. Chemosphere, 53(5), 437–446. https://doi.org/10.1016/S0045-6535(03)00545-9

Outridge, P. M., Mason, R. P., Wang, F., Guerrero, S., & Heimbürger-Boavida, L. E. (2018). Updated Global and Oceanic Mercury Budgets for the United Nations Global Mercury Assessment 2018. Environmental Science & Technology. https://doi.org/10.1021/acs.est.8b01246

Pasakarnis, T., Boyanov, M., Kemner, K., Mishra, B., O'Loughlin, E., Parkin, G., & Scherer, M. (2013). Influence of Chloride and Fe(II) Content on the Reduction of Hg(II) by Magnetite. Environmental Science & Technology, 47. https://doi.org/10.1021/es304761u

Pearson, R. G. (1963). Hard and Soft Acids and Bases. Journal of the American Chemical Society, 85(22), 3533–3539. https://doi.org/10.1021/ja00905a001

Remy, P.-Ph., Etique, M., Hazotte, A. A., Sergent, A.-S., Estrade, N., Cloquet, C., Hanna, K., & Jorand, F. P. A. (2015). Pseudo-first-order reaction of chemically and biologically formed green rusts with HgII and C15H15N3O2: Effects of pH and stabilizing agents (phosphate, silicate, polyacrylic acid, and bacterial cells). Water Research, 70, 266–278. https://doi.org/10.1016/j.watres.2014.12.007

Roebbert, Y., Rosendahl, C. D., Brown, A., Schippers, A., Bernier-Latmani, R., & Weyer, S. (2021). Uranium Isotope Fractionation during the Anoxic Mobilization of Noncrystalline U(IV) by Ligand Complexation. Environmental Science & Technology, 55(12), 7959–7969. https://doi.org/10.1021/acs.est.0c08623

Sherman, L. S., Blum, J. D., Johnson, K. P., Keeler, G. J., Barres, J. A., & Douglas, T. A. (2010). Mass-independent fractionation of mercury isotopes in Arctic snow driven by sunlight. Nature Geoscience, 3(3), Article 3. https://doi.org/10.1038/ngeo758

Skyllberg, U., Cai, Y., & O'Driscoll, N. J. (2012). Chemical speciation of mercury in soil and sediment. Liu G, 219–258.

Stookey, L. L. (1970). Ferrozine—A new spectrophotometric reagent for iron. Analytical Chemistry, 42(7), 779–781. https://doi.org/10.1021/ac60289a016

Streets, D. G., Horowitz, H. M., Lu, Z., Levin, L., Thackray, C. P., & Sunderland, E. M. (2019). Five hundred years of anthropogenic mercury: Spatial and temporal release profiles*. Environmental Research Letters, 14(8), 084004. https://doi.org/10.1088/1748-9326/ab281f

Teng, F.-Z., Dauphas, N., & Watkins, J. M. (2017). Non-traditional stable isotopes. In Non-Traditional Stable Isotopes (p. 885).

Viollier, E., Inglett, P. W., Hunter, K., Roychoudhury, A. N., & Van Cappellen, P. (2000). The ferrozine method revisited: Fe(II)/Fe(III) determination in natural waters. Applied Geochemistry, 15(6), 785–790. https://doi.org/10.1016/S0883-2927(99)00097-9

Wang, Y., Bartov, G., Wang, T., Reinfelder, J. R., Johnson, T. M., & Yee, N. (2021). Rapid Attainment of Isotopic Equilibrium after Mercury Reduction by Ferrous Iron Minerals

and Isotopic Exchange between Hg(II) and Hg(0). ACS Earth and Space Chemistry, 5(6), 1384–1394. https://doi.org/10.1021/acsearthspacechem.1c00026

Wang, Y., Morin, G., Ona-Nguema, G., Juillot, F., Calas, G., & Brown, G. E. (2011). Distinctive Arsenic(V) Trapping Modes by Magnetite Nanoparticles Induced by Different Sorption Processes. Environmental Science & Technology, 45(17), 7258–7266. https://doi.org/10.1021/es200299f

Wiatrowski, H., Das, S., Kukkadapu, R., Ilton, E., & Yee, N. (2009). Reduction of Hg(II) to Hg(0) by magnetite. Environmental Science & Technology, 43, 5307–5313. https://doi.org/10.1021/es9003608

Wiederhold, J. (2015). Metal Stable Isotope Signatures as Tracers in Environmental Geochemistry. Environmental Science & Technology, 49. https://doi.org/10.1021/es504683e

Wiederhold, J. G., Cramer, C. J., Daniel, K., Infante, I., Bourdon, B., & Kretzschmar, R. (2010). Equilibrium Mercury Isotope Fractionation between Dissolved Hg(II) Species and Thiol-Bound Hg. Environmental Science & Technology, 44(11), 4191–4197. https://doi.org/10.1021/es100205t

Yang, S., & Liu, Y. (2015). Nuclear volume effects in equilibrium stable isotope fractionations of mercury, thallium and lead. Scientific Reports (Nature Publisher Group), 5, 12626. http://dx.doi.org/10.1038/srep12626

Zheng, W., Demers, J. D., Lu, X., Bergquist, B. A., Anbar, A. D., Blum, J. D., & Gu, B. (2019). Mercury Stable Isotope Fractionation during Abiotic Dark Oxidation in the Presence of Thiols and Natural Organic Matter. Environmental Science & Technology, 53(4), 1853–1862. https://doi.org/10.1021/acs.est.8b05047

Zheng, W., Foucher, D., & Hintelmann, H. (2007). Mercury isotope fractionation during volatilization Hg(0) from solution into the gas phase. Journal of Analytical Atomic Spectrometry - J ANAL ATOM SPECTROM, 22. https://doi.org/10.1039/b705677j

Zheng, W., & Hintelmann, H. (2009). Mercury isotope fractionation during photoreduction in natural water is controlled by its Hg/DOC ratio. Geochimica et Cosmochimica Acta, 73(22), 6704–6715. https://doi.org/10.1016/j.gca.2009.08.016

Zheng, W., & Hintelmann, H. (2010a). Isotope Fractionation of Mercury during Its Photochemical Reduction by Low-Molecular-Weight Organic Compounds. The Journal of Physical Chemistry A, 114(12), 4246–4253. https://doi.org/10.1021/jp9111348

Zheng, W., & Hintelmann, H. (2010b). Nuclear Field Shift Effect in Isotope Fractionation of Mercury during Abiotic Reduction in the Absence of Light. The Journal of Physical Chemistry A, 114(12), 4238–4245. https://doi.org/10.1021/jp910353y

Appendix

The appendix contains the supplementary information for this thesis. An additional electronic appendix contains the additional raw data generated throughout the thesis work.

Appendix A: Initial concentrations reduction experiments

The results of the concentration analysis of the experiments listed in *Table A1* and *Table A2* can be found in the electronical appendix in unpolished form. All the experiments conducted during the lab work for this thesis took a huge part in reaching the data discussed in the thesis.

Table A1: List of initial concentrations of chemicals used in the respective homogeneous experiments.

Experiment	Hg (µmol/l)	$FeCl_2$ (µmol/l)	NaCl (µmol/l)	pH	Buffer	Date
Hom A	0.5	0	0	8.0	PIPPS	2020-07-09
Hom B	0.5	3.92	0	8.0	PIPPS	2020-07-09
Hom C	0.5	7.84	0	8.0	PIPPS	2020-07-09
Hom D	0.5	0	34.22	8.0	PIPPS	2020-08-14
Hom E	0.5	39.22	34.22	8.0	PIPPS	2020-08-14
Hom F	0.5	78.43	34.22	8.0	PIPPS	2020-08-14
Hom G	0.5	0	2500	7.5	MOPS	2020-09-10
Hom H	0.5	78.43	2500	7.5	MOPS	2020-09-10
Hom I	0.5	156.86	2500	7.5	MOPS	2020-09-10
Hom J	0.5	0	34.2	8.0	MOPS	2020-10-14
Hom K	0.5	12.5	34.2	8.0	MOPS	2020-10-14
Hom L	0.5	37.5	34.2	8.0	MOPS	2020-10-14
Hom M	0.5	0	342.2	8.0	MOPS	2020-10-28
Hom N	0.5	12.5	342.2	8.0	MOPS	2020-10-28
Hom O	0.5	37.5	342.2	8.0	MOPS	2020-10-28
Hom P	0.5	0	342.2	8.0	MOPS	2020-11-11
Hom Q	0.5	12.5	342.2	8.0	MOPS	2020-11-11
Hom R	0.5	12.5	342.2	8.0	MOPS	2020-11-11
Hom S	0.5	12.5	342.2	8.0	MOPS	2021-01-15
Hom T	0.5	12.5	342.2	8.0	MOPS	2021-01-15
Hom U	0.5	12.5	342.2	8.0	MOPS	2021-01-15
Hom V	0.5	12.5	342.2	8.0	MOPS	2021-02-26
Hom W	0.5	12.5	342.2	8.0	MOPS	2021-02-26
Hom X	0.5	12.5	342.2	8.0	MOPS	2021-02-26

Table A2: List of initial concentrations of chemicals used in the respective heterogeneous experiments. For all the experiments, pH was adjusted to 8.0 and 20 mM MOPS was used as buffer.

Experiment	Hg (µmol/l)	$FeCl_2$ (µmol/l)	NaCl (µmol/l)	Al_2O_3 (m^2/l)	Date
Het A	0.5	12.5	342.2	360	2020-11-11
Het B	0.5	125	342.2	360	2020-11-11
Het C	0.5	62.5	342.2	360	2021-01-26
Het D	0.5	62.5	342.2	360	2021-01-26
Het E	0.5	62.5	342.2	360	2021-01-26
Het F	5.0	69.3	342.2	4500	2021-04-08
Het G	5.0	69.3	342.2	4500	2021-04-08

Appendix B: Hg concentration data

In *table B1 – table B3*, the concentration analysis data for the sorption, the homogeneous and the heterogeneous reduction experiments con be found. This data is already shown in the respective figures of each experiment.

Table B1: Sorption experiment Hg concentration results in each sample of the experiments SorpG-SorpP and the time of sampling after experimental start.

Sample	Conc. Hg (nM)	Time (min)	Sample	Conc. Hg (nM)	Time (min)
SorpG0 unf.	345.38	3	**SorpK1**	46.21	30
SorpG0 fil.	274.24	3	**SorpK2**	23.93	120
SorpG1	216.21	30	**SorpK3**	26.82	240
SorpG2	190.99	120	**SorpK4**	461.19	240
SorpG3	186.45	240	**SorpL0 unf.**	348.82	3
SorpG4	330.92	240	**SorpL0 fil.**	79.57	3
SorpH0 unf.	213.77	3	**SorpL1**	48.26	30
SorpH0 fil.	143.63	3	**SorpL2**	39.03	120
SorpH1	111.77	30	**SorpL3**	43.32	240
SorpH2	101.00	120	**SorpL4**	396.58	240
SorpH3	98.16	240	**SorpM0 unf.**	3813.55	3
SorpH4	309.29	240	**SorpM0 fil**	779.40	3
SorpI0 unf.	319.36	3	**SorpM2**	455.95	120
SorpI0 fil.	183.06	3	**SorpM4**	3412.33	240
SorpI1	114.21	30	**SorpN0 unf.**	4027.12	3
SorpI2	105.19	120	**SorpN0 fil**	509.60	3
SorpI3	99.46	240	**SorpN2**	243.48	120
SorpI4	382.57	240	**SorpN4**	4647.09	240
SorpJ0 unf.	306.70	3	**SorpO0 unf.**	4420.56	3
SorpJ0 fil.	146.87	3	**SorpO0 fil**	878.01	3
SorpJ1	107.08	30	**SorpO2**	465.43	120
SorpJ2	95.72	120	**SorpO4**	3285.31	240
SorpJ3	84.95	240	**SorpP0 unf.**	4066.01	3
SorpJ4	309.54	240	**SorpP0 fil**	523.85	3
SorpK0 unf.	345.88	3	**SorpP2**	255.35	120
SorpK0 fil.	74.13	3	**SorpP4**	4613.09	240

Table B2: Hg concentration results of the homogeneous reduction experiments HomN and HomR. To each sample the according sampling time after experimental start is assigned.

Sample	Hg conc. (nmol)	time (min)	Sample	Hg conc. (nmol)	time (min)
HomN0	455,75	0	**HomR0**	466,37	0
HomN1	412,20	30	**HomR1**	441,23	30
HomN2	311,40	60	**HomR2**	378,25	60
HomN3	149,29	120	**HomR3**	248,61	120
HomN4	77,69	180	**HomR4**	127,58	180
HomN5	54,27	240	**HomR6**	136,58	-
HomNT1	289,77	30	**HomRT1**	263,46	30
HomNT2	560,00	60	**HomRT2**	490,91	60
HomNT3	1164,37	120	**HomRT3**	1178,90	120
HomNT4	726,30	180	**HomRT4**	1009,78	180
HomNT5	202,04	240			

Table B3: Hg concentration results of the heterogeneous reduction experiments HetF and HetG. To each sample the according sampling time after experimental start is assigned.

Sample	Hg conc. (nmol/L)	time (min)	Sample	Hg conc. (nmol/L)	time (min)
HetF0	2774.02	0	**HetG0**	3631.49	0
HetF1	3120.20	30	**HetG1**	3717.88	30
HetF2	3188.24	60	**HetG2**	4131.06	60
HetF3	3435.17	120	**HetG3**	3584.28	120
HetF4	3392.44	180	**HetG4**	3396.78	180
HetF5	3291.64	240	**HetG5**	2704.97	240
HetF6	2116.26	1140	**HetG6**	2130.37	1140
HetF7	1905.40	-	**HetG7**	2191.34	-
HetF0 fil	553.27	0	**HetG0 fil**	606.11	0
HetF1 fil	423.20	30	**HetG1 fil**	422.55	30
HetF2 fil	430.03	60	**HetG2 fil**	422.90	60
HetF3 fil	356.10	120	**HetG3 fil**	349.07	120
HetF4 fil	299.42	180	**HetG4 fil**	326.34	180
HetF5 fil	288.10	240	**HetG5 fil**	310.68	240
HetF6 fil	127.72	1140	**HetG6 fil**	118.15	1140
HetFT1	138.74	30	**HetGT1**	198.02	30
HetFT2	732.94	60	**HetGT2**	788.47	60
HetFT3	2612.19	120	**HetGT3**	2460.24	120
HetFT4	3566.23	180	**HetGT4**	3545.54	180
HetFT5	4484.27	240	**HetGT5**	4781.39	240
HetFT6	9843.21	1140	**HetGT6**	9486.76	1140

Appendix C: Hg isotope data

The isotope measurements done for this thesis exceeded the data discussed. Other values gathered could also be imported in the future (for example Δ^{200}Hg and Δ^{204}Hg). In *Table C1 - Table C3,* all the important isotope data of the experiments conducted in this thesis is given.

Table C1: SorpM-SorpP Hg isotope results. Here, only the most important isotope ratios are depicted: δ^{202}Hg, Δ^{199}Hg, Δ^{200}Hg, Δ^{201}Hg and Δ^{204}Hg. Errors are reported in 2SD.

Sample	δ^{202}Hg	Δ^{199}Hg	Δ^{200}Hg	Δ^{201}Hg	Δ^{204}Hg
SorpMO unf	0.01 ± 0.16	0.00 ± 0.05	0.01 ± 0.04	-0.01 ± 0.08	0.04 ± 0.07
SorpM0 fil	0.34 ± 0.16	0.07 ± 0.05	0.02 ± 0.04	0.03 ± 0.08	0.00 ± 0.07
SorpM2	0.10 ± 0.16	0.07 ± 0.05	0.04 ± 0.04	0.08 ± 0.08	0.00 ± 0.07
SorpM4	0.02 ± 0.16	-0.02 ± 0.05	-0.02 ± 0.04	-0.04 ± 0.08	0.01 ± 0.07
SorpN0 unf	0.01 ± 0.16	-0.03 ± 0.05	0.01 ± 0.04	-0.01 ± 0.08	0.01 ± 0.07
SorpN0 fil	0.24 ± 0.16	0.04 ± 0.05	0.02 ± 0.04	0.03 ± 0.08	0.00 ± 0.07
SorpN2	-0.03 ± 0.16	0.05 ± 0.05	0.00 ± 0.04	0.03 ± 0.08	0.03 ± 0.07
SorpN4	-0.01 ± 0.16	-0.04 ± 0.05	0.00 ± 0.04	-0.03 ± 0.08	0.03 ± 0.07
SorpO0 unf	0.06 ± 0.16	-0.01 ± 0.05	0.01 ± 0.04	0.00 ± 0.08	-0.06 ± 0.07
SorpO0 fil	0.39 ± 0.16	0.03 ± 0.05	-0.01 ± 0.04	0.01 ± 0.08	0.01 ± 0.07
SorpO4	0.09 ± 0.16	0.01 ± 0.05	0.00 ± 0.04	0.04 ± 0.08	-0.01 ± 0.07
SorpO0 fil	0.45 ± 0.16	0.09 ± 0.05	0.06 ± 0.04	0.16 ± 0.08	-0.08 ± 0.07
SorpO2	-0.06 ± 0.16	0.06 ± 0.05	0.01 ± 0.04	0.04 ± 0.08	-0.03 ± 0.07
SorpP0 unf	0.02 ± 0.16	0.02 ± 0.05	0.03 ± 0.04	0.00 ± 0.08	-0.02 ± 0.07
SorpP0 fil	0.38 ± 0.16	0.06 ± 0.05	0.04 ± 0.04	0.04 ± 0.08	-0.06 ± 0.07
SorpP2	0.09 ± 0.16	0.11 ± 0.05	0.02 ± 0.04	0.14 ± 0.08	-0.07 ± 0.07
SorpP4	-0.03 ± 0.16	0.00 ± 0.05	-0.01 ± 0.04	0.00 ± 0.08	0.01 ± 0.07

Table C2: Hg isotope measurement results of the experiments HomN and HomR. Here, only the most important isotope ratios are depicted: δ^{202}Hg, Δ^{199}Hg, Δ^{200}Hg, Δ^{201}Hg and Δ^{204}Hg. Errors are reported in 2SD.

Sample	δ^{202}Hg	Δ^{199}Hg	Δ^{200}Hg	Δ^{201}Hg	Δ^{204}Hg
HomN0a	0.139 ± 0.08	0.012 ± 0.03	0.008 ± 0.01	-0.018 ± 0.04	0.034 ± 0.09
HomN0b	0.095 ± 0.08	-0.027 ± 0.03	-0.008 ± 0.01	-0.010 ± 0.04	0.011 ± 0.09
HomN0a/b	0.115 ± 0.08	-0.016 ± 0.03	-0.027 ± 0.01	-0.016 ± 0.04	0.002 ± 0.09
HomN1	0.212 ± 0.08	-0.029 ± 0.03	0.011 ± 0.01	-0.003 ± 0.04	-0.035 ± 0.09
HomN2	0.814 ± 0.08	-0.078 ± 0.03	-0.006 ± 0.01	-0.057 ± 0.04	-0.070 ± 0.09
HomN3	2.312 ± 0.08	-0.207 ± 0.03	-0.019 ± 0.01	-0.114 ± 0.04	-0.017 ± 0.09
HomN4	3.628 ± 0.08	-0.296 ± 0.03	-0.030 ± 0.01	-0.176 ± 0.04	0.006 ± 0.09
HomN5a	4.044 ± 0.08	-0.365 ± 0.03	-0.048 ± 0.01	-0.218 ± 0.04	-0.012 ± 0.09
HomN5b	4.221 ± 0.08	-0.350 ± 0.03	-0.043 ± 0.01	-0.209 ± 0.04	0.043 ± 0.09
HomNT1	-2.719 ± 0.08	0.265 ± 0.03	0.018 ± 0.01	0.149 ± 0.04	-0.016 ± 0.09
HomNT2	-2.016 ± 0.08	0.218 ± 0.03	0.025 ± 0.01	0.108 ± 0.04	-0.028 ± 0.09
HomNT3	-1.611 ± 0.08	0.187 ± 0.03	0.022 ± 0.01	0.103 ± 0.04	-0.044 ± 0.09
HomNT4	0.652 ± 0.08	-0.050 ± 0.03	-0.010 ± 0.01	-0.047 ± 0.04	0.020 ± 0.09
HomNT5	1.896 ± 0.08	-0.219 ± 0.03	-0.040 ± 0.01	-0.140 ± 0.04	0.018 ± 0.09
HomR0a	0.108 ± 0.06	0.009 ± 0.03	0.012 ± 0.01	0.026 ± 0.02	-0.019 ± 0.10
HomR0b	-0.021 ± 0.06	-0.007 ± 0.03	0.004 ± 0.01	0.008 ± 0.02	0.011 ± 0.10
HomR1	0.219 ± 0.06	-0.021 ± 0.03	0.016 ± 0.01	0.001 ± 0.02	-0.020 ± 0.10
HomR2	0.608 ± 0.06	-0.034 ± 0.03	0.002 ± 0.01	-0.037 ± 0.02	-0.017 ± 0.10
HomR3	1.624 ± 0.06	-0.108 ± 0.03	-0.014 ± 0.01	-0.095 ± 0.02	0.036 ± 0.10
HomR4a	2.971 ± 0.06	-0.260 ± 0.03	-0.025 ± 0.01	-0.194 ± 0.02	0.033 ± 0.10
HomR4b	3.018 ± 0.06	-0.268 ± 0.03	-0.040 ± 0.01	-0.168 ± 0.02	0.016 ± 0.10
HomRT1	-2.821 ± 0.06	0.298 ± 0.03	0.039 ± 0.01	0.177 ± 0.02	-0.015 ± 0.10
HomRT2	-2.350 ± 0.06	0.223 ± 0.03	0.004 ± 0.01	0.097 ± 0.02	-0.046 ± 0.10
HomRT3	-1.576 ± 0.06	0.157 ± 0.03	0.032 ± 0.01	0.100 ± 0.02	-0.049 ± 0.10
HomRT4	-0.185 ± 0.06	0.034 ± 0.03	0.008 ± 0.01	0.035 ± 0.02	-0.032 ± 0.10

Table C3: MC-ICP-MS results of the most important isotope ratios (δ^{202}Hg, Δ^{199}Hg, Δ^{200}Hg, Δ^{201}Hg and Δ^{204}Hg) of the heterogeneous reduction experiments HetF and HetG. Errors are reported as 2SD.

Sample	δ^{202}Hg	Δ^{199}Hg	Δ^{200}Hg	Δ^{201}Hg	Δ^{204}Hg
HetF0	0.065 ± 0.13	0.017 ± 0.06	0.009 ± 0.01	0.017 ± 0.17	-0.040 ± 0.01
HetF1	0.058 ± 0.13	0.022 ± 0.06	-0.014 ± 0.01	-0.045 ± 0.17	0.004 ± 0.01
HetF2	0.120 ± 0.13	-0.067 ± 0.06	-0.032 ± 0.01	-0.119 ± 0.17	0.039 ± 0.01
HetF3	0.361 ± 0.13	-0.025 ± 0.06	-0.009 ± 0.01	-0.037 ± 0.17	-0.002 ± 0.01
HetF4	0.532 ± 0.13	-0.071 ± 0.06	-0.019 ± 0.01	-0.019 ± 0.17	-0.015 ± 0.01
HetF5	0.653 ± 0.13	-0.096 ± 0.06	-0.003 ± 0.01	-0.067 ± 0.17	-0.007 ± 0.01
HetF6	1.610 ± 0.13	-0.187 ± 0.06	-0.039 ± 0.01	-0.158 ± 0.17	-0.004 ± 0.01
HetF7	1.558 ± 0.13	-0.130 ± 0.06	-0.007 ± 0.01	-0.096 ± 0.17	0.027 ± 0.01
HetF0 fil	0.240 ± 0.05	0.030 ± 0.02	-0.006 ± 0.03	0.001 ± 0.00	0.007 ± 0.03
HetF1 fil	0.050 ± 0.05	0.042 ± 0.02	-0.005 ± 0.03	0.059 ± 0.00	-0.048 ± 0.03
HetF2 fil	0.044 ± 0.05	0.039 ± 0.02	-0.008 ± 0.03	0.027 ± 0.00	-0.022 ± 0.03
HetF3 fil	0.261 ± 0.05	0.007 ± 0.02	0.000 ± 0.03	0.052 ± 0.00	-0.037 ± 0.03
HetF4 fil	0.333 ± 0.05	-0.037 ± 0.02	-0.056 ± 0.03	-0.110 ± 0.00	0.076 ± 0.03
HetF5 fil	0.523 ± 0.05	-0.034 ± 0.02	0.003 ± 0.03	-0.005 ± 0.00	0.011 ± 0.03
HetF6 fil	1.399 ± 0.05	-0.126 ± 0.02	-0.014 ± 0.03	-0.097 ± 0.00	0.018 ± 0.03
HetFT2	-2.304 ± 0.13	0.235 ± 0.06	0.016 ± 0.01	0.151 ± 0.17	-0.004 ± 0.01
HetFT3	-1.975 ± 0.13	0.216 ± 0.06	0.033 ± 0.01	0.150 ± 0.17	-0.053 ± 0.01
HetFT4	-1.854 ± 0.13	0.239 ± 0.06	0.036 ± 0.01	0.165 ± 0.17	-0.012 ± 0.01
hetFT5	-1.822 ± 0.13	0.211 ± 0.06	0.018 ± 0.01	0.148 ± 0.17	0.020 ± 0.01
HetFT6	-1.316 ± 0.13	0.128 ± 0.06	-0.016 ± 0.01	0.077 ± 0.17	-0.007 ± 0.01
HetG0	0.007 ± 0.04	0.010 ± 0.02	-0.022 ± 0.04	0.000 ± 0.09	-0.015 ± 0.11
HetG1	0.049 ± 0.04	0.009 ± 0.02	-0.009 ± 0.04	-0.024 ± 0.09	0.013 ± 0.11
HetG2	0.092 ± 0.04	-0.047 ± 0.02	-0.027 ± 0.04	-0.078 ± 0.09	0.028 ± 0.11
HetG3	0.349 ± 0.04	-0.031 ± 0.02	-0.001 ± 0.04	0.004 ± 0.09	0.030 ± 0.11
HetG4	0.539 ± 0.06	-0.057 ± 0.02	-0.008 ± 0.06	-0.046 ± 0.05	-0.008 ± 0.01
HetG5	0.674 ± 0.06	-0.086 ± 0.02	-0.012 ± 0.06	-0.044 ± 0.05	-0.027 ± 0.01
HetG6	1.767 ± 0.06	-0.144 ± 0.02	0.002 ± 0.06	-0.091 ± 0.05	0.002 ± 0.01
HetG7	1.757 ± 0.06	-0.180 ± 0.02	-0.025 ± 0.06	-0.066 ± 0.05	0.003 ± 0.01
HetG0 fil	0.266 ± 0.06	0.044 ± 0.02	0.005 ± 0.06	-0.008 ± 0.05	-0.006 ± 0.01
HetG1 fil	0.153 ± 0.06	0.034 ± 0.02	0.008 ± 0.06	0.009 ± 0.05	-0.031 ± 0.01
HetG2 fil	-0.007 ± 0.06	0.054 ± 0.02	0.007 ± 0.06	0.034 ± 0.05	-0.004 ± 0.01
HetG3 fil	0.253 ± 0.06	0.011 ± 0.02	-0.021 ± 0.06	-0.020 ± 0.05	0.028 ± 0.01
HetG4 fil	0.407 ± 0.06	-0.031 ± 0.02	-0.015 ± 0.06	-0.015 ± 0.05	-0.008 ± 0.01
HetG5 fil	0.573 ± 0.06	-0.053 ± 0.02	-0.027 ± 0.06	-0.056 ± 0.05	-0.018 ± 0.01
HetG6 fil	1.676 ± 0.06	-0.157 ± 0.02	-0.032 ± 0.06	-0.102 ± 0.05	0.001 ± 0.01
HetGT1	-2.151 ± 0.04	0.301 ± 0.02	0.062 ± 0.04	0.200 ± 0.09	-0.041 ± 0.11
HetGT2	-2.080 ± 0.04	0.202 ± 0.02	-0.016 ± 0.04	0.082 ± 0.09	-0.039 ± 0.11
HetGT3	-2.052 ± 0.04	0.163 ± 0.02	-0.010 ± 0.04	0.074 ± 0.09	0.081 ± 0.11
HetGT4	-1.934 ± 0.04	0.187 ± 0.02	0.030 ± 0.04	0.179 ± 0.09	-0.047 ± 0.11
HetGT5	-1.910 ± 0.04	0.237 ± 0.02	0.047 ± 0.04	0.228 ± 0.09	-0.059 ± 0.11
HetGT6	-1.472 ± 0.04	0.113 ± 0.02	-0.024 ± 0.04	-0.009 ± 0.09	0.002 ± 0.11